STRUCTURAL DEPENDENCE OF OXIDATIVE PROPERTIES OF Mn-OXIDE NANOPARTICLES PREPARED BY A FACILE GEL FORMATION METHOD

A THESIS SUBMITTED IN PARTIAL FULFILLMENT OF THE REQUIREMENT FOR THE DEGREE OF MASTER OF PHILOSOPHY (M. PHIL.) IN CHEMISTRY

SUBMITTED BY

A. K. M. ATIQUE ULLAH
STUDENT ID: 0412033213P
SESSION: APRIL 2012

Nano-Chemistry Research Laboratory   **APRIL 2015**

Department of Chemistry

Bangladesh University of Engineering and

Technology (BUET)

Dhaka-1000, Bangladesh

Declaration by the Candidate

I do hereby declare that this thesis work, entitled "Structural Dependence of Oxidative Properties of Mn-oxide Nanoparticles Prepared by a Facile Gel Formation Method" submitted in partial fulfillment for the requirement of M. Phil. Degree in Chemistry to the Department of Chemistry, Bangladesh University of Engineering and Technology (BUET) in April 2015, is genuine work done by me under the supervision of Dr. Md. Shakhawat Hossain Firoz, Associate Professor, Department of Chemistry, Bangladesh University of Engineering and Technology (BUET). The thesis or part of it has not been submitted elsewhere for the award or any degree or diploma.

....

(A. K. M. Atique Ullah)

Signature of the Candidate

Certificate

This is to certify that this thesis work entitled "Structural Dependence of Oxidative Properties of Mn-oxide Nanoparticles Prepared by a Facile Gel Formation Method" submitted by A. K. M. Atique Ullah, Student ID: 0412033213P, to the Department of Chemistry, Bangladesh University of Engineering and Technology (BUET) in partial fulfillment for the requirement of M. Phil. in Chemistry in April 2015 is based on his original research and investigation carried out under my guidance and supervision.

Supervisor:

…………………………………………

Dr. Md. Shakhawat Hossain Firoz
Associate Professor
Department of Chemistry
Bangladesh University of Engineering and
Technology (BUET), Dhaka, Bangladesh

DEDICATED TO

MY BELOVED PARENTS
&
HONORABLE SUPERVISOR

Acknowledgement

 April 2015   A. K. M. Atique Ullah

Bangladesh University of Engineering and Technology, Dhaka
Department of Chemistry

Certification of Thesis

A thesis on

STRUCTURAL DEPENDENCE OF OXIDATIVE PROPERTIES OF Mn-OXIDE NANOPARTICLES PREPARED BY A FACILE GEL FORMATION METHOD

BY

A. K. M. Atique Ullah

has been accepted as satisfactory in partial fulfillment of the requirements for the degree of Master of Philosophy (M. Phil.) in Chemistry and certify that the student has demonstrated a satisfactory knowledge of the field covered by this thesis in an oral examination held on April 8, 2015

Board of Examiners

1. Dr. Md. Shakhawat Hossain Firoz
Associate Professor
Department of Chemistry
BUET, Dhaka
_____
Supervisor & Chairman

2. Dr. Md. Nazrul Islam
Professor & Head
Department of Chemistry
BUET, Dhaka
_____
Member (Ex-officio)

3. Dr. Md.Shafiul Azam
Assistant Professor
Department of Chemistry
BUET, Dhaka
_____
Member

4. Dr. Md. Mofazell Hossain
Professor
Department of Chemistry
University of Dhaka, Dhaka
Member (External)

Abstract

The noble synthesis of Mn-oxides nanoparticles and their structural dependence of oxidative properties is a subject of intensive research for their imminent applications in different fields of science and engineering. In the present study, Mn-oxides nanoparticles with different crystal geometry have been synthesized by a facile gel formation route and their structural and oxidative characterizations have been demonstrated.

During the synthesis process, a gel precursor is formed through the reduction of $KMnO_4$ with glycerol. After the heat treatment of the gel precursor at different temperatures, Mn-oxides nanoparticles having different oxidation states, *viz.*, Mn_3O_4, Mn_5O_8 and Mn_2O_3 were formed. The phase identification, chemical composition, crystal structure, crystallinity and surface morphology were analyzed using powder X-ray Diffraction (XRD), Energy Dispersive X-ray (EDX), Fourier Transform Infra Red (FT-IR) and Field Emission Scanning Electron Microscopy (FESEM) techniques. Mn_3O_4 nanoparticles with tetragonal crystal structure and average crystallite size of 42 nm were formed at 80 °C. Then the two other forms, Mn_5O_8 nanorods with monoclinic crystal structure and Mn_2O_3 nanoparticles with cubic crystal structure were formed after heat treatment the gel precursor at 350 °C and 700 °C respectively. The average crystallite size of Mn_5O_8 and Mn_2O_3 nanoparticles calculated from the XRD data was found to be 35 nm and 28 nm respectively.

The structural dependence of oxidative property of the synthesized Mn-oxides nanoparticles was demonstrated from the decolorization of Methylene Blue (MB) using UV-visible spectroscopic technique. Effect of MB concentration, amount of nanoparticles required, influence of pH of the medium and function of time on MB decolorization were also investigated. The dye degradation experiments show that Mn_3O_4 nanoparticles decolorizes the dye through oxidative and adsorptive activity whereas Mn_5O_8 and Mn_2O_3 nanoparticles decolorize the dye through oxidative activity. Among the three oxides of Mn, Mn_5O_8 nanorods show superior dye decolorizing ability.

i

Contents

List of Figures

List of Tables

CHAPTER 1

INTRODUCTION

1.1 Introduction

Manganese oxides (Mn-oxides) have been attracted considerable interest due to their potential applications in catalysts, ion exchanging materials, electrochemical materials, high-density magnetic storage media, solar energy transformation, molecular adsorption, etc [1-6]. But it is well recognized that the functionality of materials is enhanced when they are reduced to nano-sized dimensions. In addition, the properties of nanomaterials depend on their structures and morphologies also. Therefore, understanding the structural dependence of oxidative property of Mn-oxides nanomaterials is a subject of intensive research for their imminent applications as powerful oxidants.

The oxidative properties of Mn-oxides are well proved. It has been reported that oxides and hydroxides of Mn can oxidize many inorganic compounds including Co(II), Cr(III), As(III), Sb(III) and Se(IV) [7-11] also a variety of natural and xenobiotic organic compounds such as catechol, quinines, substituted phenols, aromatic amines, pesticides and explosives (e.g. TNT) [12-16]. It has also been reported that Mn-oxides nanomaterials can be used as an active catalyst for the oxidation of methane and carbon monoxide [17] and selective reduction of nitrobenzene [18]; moreover, it is an effective material to prevent air pollution and limit the emission of NO_x and volatile organic compounds from waste gases of different origins [19]. Mn-oxides have been considered as potential electrode materials in lithium-ion batteries on the basis of their high theoretical lithium-storage capacities: 615 mAh/g for MnO_2, 679 mAh/g for Mn_2O_3 and 703 mA/g for Mn_3O_4 [20]. Recently, Seo et al. [21] investigated the size and structure dependent magnetic properties of Mn_3O_4 and MnO nanoparticles. They reported that Mn_3O_4 nanoparticles showed more ferromagnetic behavior whereas MnO nanoparticles showed weak ferromagnetic behavior. Therefore, from the above mentioned investigations and other literatures it is evident that metal oxides with nano scale dimensions as well as

mixed valence states are more functioning than the single valence state and bulk materials. This is expected to be true for Mn-oxides nanoparticles as well. Another important motive for the unusual properties of nanomaterials is due to their structures. It is demonstrated that the functionality of nanomaterials is strongly dependent on their crystal structures and morphology. Recently, Zhang et al. [22] reported shape controlled synthesis of Mn_3O_4 nanocrytals and their catalytic degradation of methylene blue (MB). They synthesized Mn_3O_4 crystallites of various sizes and shapes using surfactant as structure-directing agents. They found that the octahedral Mn_3O_4 nanostructures possessed a capacity for very high (above 99.7%) degradation of MB as compared to tetragonal Mn_3O_4. Therefore, it is also indispensable to synthesize Mn-oxides nanoparticles with various crystal structures in order to investigate their relative functionality.

Mn occurs normally in the Mn(II), Mn(III) and Mn(IV) oxidation states in natural environments. All three valences form a large number of oxide minerals, ranging from the simple phases manganosite, MnO; partridgite, Mn_2O_3 and pyrolusite, MnO_2 to complex mixed valence oxides such as hauusmannite, Mn_3O_4 (Mn^{2+}, Mn^{3+}), Mn_5O_8 (Mn^{3+}, Mn^{4+}) etc. The crystal structures of Mn-oxides with oxidation states +2, +3 and +4 are shown in Fig.1.1
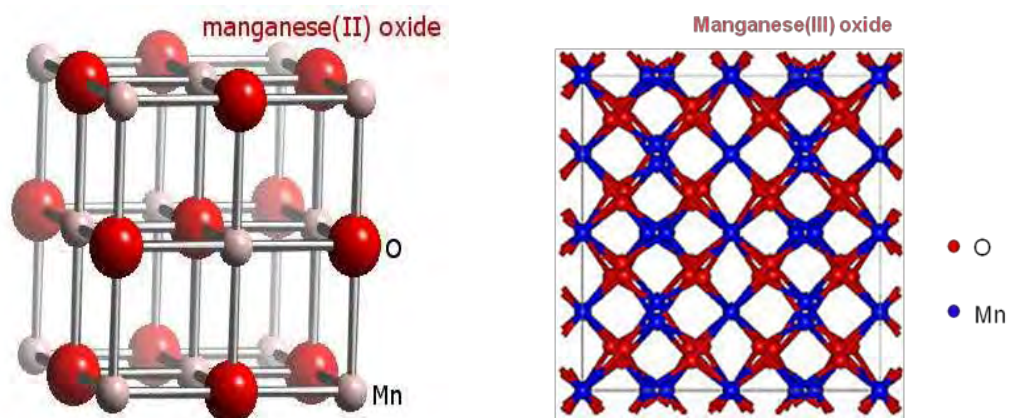
Fig. 1.1 (a): Crystal structures of Mn(II) and Mn(III) oxides
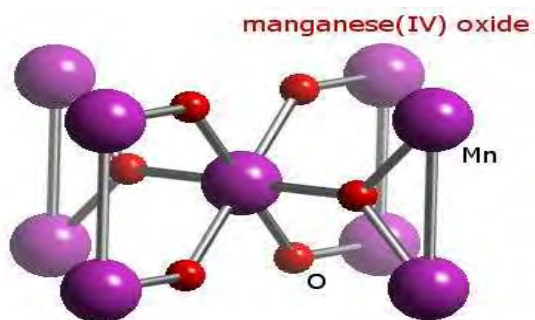
Fig.1.1 (b): Crystal structure of Mn(IV) oxide

Naturally occurring Mn-oxides are hardly found in single phase as they are assorted with other metal oxides which as a whole do not allow us to get particle size to the extent of nanoscale as well as pure state. Therefore, it is still desirable to develop a more accommodating, efficient and simple approach to achieve a single route for synthesizing Mn-oxides with single phase and nanosized dimensions.

Various methods have been reported for the synthesis of Mn-oxides nanoparticles. Among these methods, the most common one is the calcinations of oxides, hydroxides, hydroxyoxides, oxysalts, carbonates, nitrates, or sulphates of Mn in air at about 1000 °C [23-25]. However, theses are economically unviable. Another conventional method for synthesizing of Mn-oxides is the precipitation technique which requires precipitating metal salts with hydroxide ions followed by dehydration. In this method, the formation of solid usually proceeds rapidly which results in particulate with various sizes. Recently, wet chemical preparation of nanoscale Mn-oxides materials was also developed. This technique involves oxidation/reduction – precipitation process via either the oxidation of Mn^{2+} [26-28] or the reduction of MnO_4^- [29], thermal decomposition of manganous precursors in oleyamine [30-31], solvothermal method [32] and so on. Most of these methods to prepare Mn-oxides nanomaterials need NaOH, NH_3 or other basic materials as precipitating agents in the solvent of water or ethanol and easily generate impurities such as MnOOH.

Since nanometer-sized Mn-oxides with mixed valence states are more functioning than the bulk materials as well as single valence state and the structure and morphology are dependent on the proper preparation technique, hence it is necessary to establish a single route for the synthesis of size and structure controlled Mn-oxides nanoparticles that will be cost effective and environmentally more friendly as well. The sol-gel method with low cost raw materials might be a good solution. Furthermore, till the date to the best of our knowledge, there is no published information on systematic study of the relationship between crystal geometry and properties of Mn-oxide nanomaterials. As a consequence, it is desirable to develop a single route for the synthesis of Mn-oxides nanoparticles with single as well as mixed valence states and a systematic study of their structural dependence on the oxidative properties.

1.2 Rationale of the study

The unusual properties of nanomaterials compared with that of bulk materials are not only dependent on their nanosized dimensions but also their crystal geometry and morphology as well. The crystal structure and morphology of nanomaterials are dependent on the techniques of preparation and treatment thereafter. Particles having nano-scale dimensions can be synthesized through various methods and among them hydrothermal [33-35], electrochemical route [36-37], template synthesis [38], and sol-gel processes [39-40] are notable. Among the different methods of nanomaterials preparations, sol-gel method is a highly versatile preparation method that can be used to form a variety of metal oxide nanomaterials.

Recently, a number of reports have been published for the preparation of Mn-oxides nanoparticles through sol-gel method. Ching *et al.* synthesized Mn_3O_4 nanoparticles through the sol-gel reaction between $KMnO_4$ and fumaric acid which requires a post treatment at 450 °C [41]. Mn_3O_4 nanocrystals were prepared by the reaction of $KMnO_4$ and C_2H_5OH by Zhang et al [42]. They reported that for the preparation of single phase of Mn_3O_4 nanoparticles needs higher reaction temperatures. Du *et al* [43]

also synthesized Mn_3O_4 nanoparticles by the reaction of PEG-20000 and $KMnO_4$ in an aqueous solution at 180 °C for 20 hours. Hence, it seems to be apparent that the conventional sol-gel method requires high temperature calcinations that lead to inconsistency in product quality. Furthermore, sol-gel method requires expensive alkoxides. Therefore, the conventional sol-gel method has been found to be expensive, time consuming and polluting. As a consequence it is emergent to establish a low temperature process to synthesize size and shape controlled Mn-oxides precursors without using expensive alkoxides.

Without using alkoxides, metal oxides can be synthesized by precipitating metal salts with hydroxide ions followed by dehydration. In this method, the formation of solid is usually proceeds rapidly which result in particulate with various sizes. It has been reported that the growth can be slowed down if the synthesis is carried out in organic solvent. For example, the ZnO nanoparticles with uniform diameters of 40 nm have been synthesized in the alcohol solution [44]. On the other hand, if inorganic base is applied as the OH source, even in organic solvent, the growth is not so easy to control because of the rapid release of OH [45]. However, if alcohol is used as the material, the gradual release of OH^- leads the precipitation of metal ions and the particle size could be controlled. Therefore, it is crucial to select an alcohol as a source of OH which is an easily available, non-toxic, non-hazardous, no-volatile, biodegradable and recyclable liquid. Moreover, it is also fundamental to select a material for providing Mn that is available and also cost effective.

In the present study, attempt will be taken to synthesize Mn-oxides nanoparticles via a facile gel formation route without using an expensive alkoxides. Then the Mn-oxide nanoparticles precursors will be heated at different temperatures to investigate the phase transformation as well as formation of different new phases with single and mixed valence states.

Mn-oxides nanomaterials are attracting considerable interest because of their potential application in toxic waste remediation. For pollution remediation purposes, land-born

natural Mn ores, Mn-oxides and materials coated or modified win Mn-oxides have been used for removal of Pb^{2+}, Cd^{2+}, Cu^{2+}, 17 α-ethynylestradiol [46-49], as oxidant for degradation of organic pollutants [50-51] and as oxidant and/or adsorbent for removal of As(III) and AS(IV) [52].

In view of strong oxidative properties of Mn-oxides it seems to be interesting to evaluate possible applications of Mn-oxides nanoparticles as effective oxidants for the degradation of organic contaminants in water. The major sources of water contamination are the dyes from the effluent of textile industries. The presence of dyes in water reduces light penetration and hinders photosynthesis in aquatic plants [53]. The dyes and their degradation products in surface water are highly carcinogenic [54]. So it is necessary to treat the dye effluents prior to their discharge into the receiving water. This actually motivated us for the study of oxidative degradation of dyes (e.g., MB) using Mn-oxides nanoparticles with single and mixed valence state to investigate the structural dependence of oxidative property of Mn-oxides nanoparticles.

1.3 Objectives

The main objectives of the present work are to

i)   develop a low cost facile gel formation route for the preparation of Mn-oxides nanomaterials with certain crystal geometry.

ii) structural and morphological characterization of the nanoparticles.

iii) study of the oxidative property through dye degradation.

iv) demonstrate the structural dependence of oxidative property.

References

[1]. A. R. Armstrong, P. G. Bruce, *Nature*, 381 (1996) 499

[2]. Y. F. Shen, R. P. Zerger, R. N. Deguzman, S. L. Suib, L. Mccurdy, D. I. Potter, C. L. Oyoung, *Science*, 260 (1993) 511

[3]. M. C. Bernard, H. L. Goff, B. V. Thi, *J. Electrochem. Soc.*, 140 (1993) 3065

[4]. A. H. De Vries, L. Hozoi, R. Broer, *Phys. Rev. B*, 66 (2002) 035108

[5]. Y. Yamashita, K. Mukai, J. Yoshinobu, M. Lippmaa, T. Kinoshita, M. Kawasaki, *Surf. Sci.*, 514 (2002) 54

[6]. Y. C. Zhang, T. Qiao, X. Y. Hu, *J. Solid State Chem.*, 177 (2004) 4093

[7]. A. Manceau, V. A. Drits, E. Silvester, C. Bartoli, B. Lanson, *Am. Miner.,* 82 (1997) 1150

[8]. J. G. Kim, J. B. Dixon, C. C. Chusuei, Y. Deng, *Soil. Sci. Soc. Am. J.*, 66 (2002) 306

[9]. V. Q. Chiu, J. G. Hering, *Environ. Sci. Technol.*, 34 (2000) 2029

[10]. N. Belzile, Y.-W. Chen, Z. Wang, *Chem. Geol.,* 174 (2001) 379

[11]. M. J. Scott, J. J. Morgan, *Environ. Sci. Technol.,* 30 (1996) 1990

[12]. C. J. Matocha, D. L. Sparks, J. E. Amonette, R. K. Kukkaadapu, *Soil. Sci. Soc. Am. J.*, 65 (2001) 58

[13]. R. A, Petrie, P. R. Grossl, R. C. Sims, *Environ. Sci. Technol.*, 36 (2002) 3744

[14]. H. Li, L. S. Lee, D. G. Schulze, C. Guest, *Environ. Sci. Technol.*, 37 (2003) 6

[15]. H. Zhang, C. H. Huang, *Environ. Sci. Technol.*, 39 (2005) 4474

[16]. K.-H. Kang, D.-M. Lim, H. Shin, *Water Res.*, 40 (2006) 903

[17]. E. R. Stobhe, B. A. D. Boer, J. W. Geus, *Catal. Today,* 47 (1999) 161

[18]. E. J. Grootendorst, Y. Verbeek, V. Ponek, *J. Catal.*, 157 (1995) 706

[19]. M. M. Zwinkels, S. G. Jaras, P. G. Menon, T. A. Griffin, *Catal. Rev. Sci. Eng.*, 35 (1993) 319

[20]. X. Fang, X. Lu, X. Guo, *Electrochem. Commun.,* 12 (2010) 1520

[21]. W. S. Seo, H. H. Jo, K. Lee, B. Kim, S. J. Oh, J. T. Park, *Angew. Chem. Int. Ed.*, 43 (2004) 1115

[22]. P. Zhang, Y. Zhang, B. Cai, C. Hao, J. Wang, C. Liu, Z. Meng, Z. Yin, Q. Chen, *Nano Res.*, DOI 10.1007/s12274-010-1026-0

[23]. C. H. Shomate, *J. Am. Chem. Soc.*, 65 (1943) 786

[24]. J. C. Southard, G. E. Moore, *J. Am. Chem. Soc.*, 64 (1942) 1769

[25]. I. Ursu, R. Alexandrescu, I. N. Michailescu, *J. Phys. B: At. Mol. Phys.*, 19 (1986) 825

[26]. T. Ozkaya, A. Baykal, H. Kavas, Y. Koseoglu, M. S. Toprak, *Physica B*, 403 (2008) 3760

[27]. D. H. Wang, D. Y. Geng, Y. J. Jhang, Z. D. Zhang, *J. Cryst. Growth*, 310 (2008) 4148

[28]. A. Askarinejad, A. Morsali, *Ultrasonics Sonochem.*, 16 (2009) 124

[29]. Z. H. Yang, C. X. Zhou, X. M. Song, W. X. Zhang, N. Zhang, *Chinese J. Inorg. Chem.*, 24 (2008) 1695

[30]. M. S.-Niasari, F. Davar, M. Mazaheri, *Polyhydron*, 27 (2008) 3467

[31]. D. S. Wang, T. Xie, Q. Peng, S. Y. Zhang, J. Chen, Y. D. Li, *Chem. Eur. J.*, 14 (2008) 2507

[32]. C. C. Hu, Y. T. Wu, K. H. Chang, *Chem. Mater.*, 20 (2008) 2890

[33]. G. H. Du, Q. Chen, R. C. Che, et al. *Appl. Phys. Lett.*, l (2001) 3702.

[34]. R. Ma, L. Zhang, T. Sasaki, et al. *Adv. Mater.*, 16 (2004) 918

[35]. F. Y. Cheng, J. Shen, W. Q. Ji, et al. *ACS Appl. Mater. Interfaces*, 1 (2009) 460

[36]. M. Nakayama, H. Tagashira, *Langmuir*, 22 (2006) 3864

[37]. C. C. Hu, C. C. Wang, *J. Electrochem. Soc.*, 150 (2003) 1079

[38]. S. Mann, *Angew Chem. Intl. Ed.*, 39 (2000) 3392

[39]. S. Franger, S. Bach, J. Farcy, et al. *J. Power Sources*, 109 (2002) 262

[40]. C. K. Lin, K. H. Chaung, C. Y. Lin, et al. *Surf. Coat. Technol.* 202 (2007)1272

[41]. S. Ching, J. L. Roark, N. Duan, *Chem. Mater.*, 9 (1997) 750

[42]. W. X. Zhang, Z. H. Yang, Y. Liu, S. P. Tang, X. Z. Han, M. Chen, *J. Cryst. Growth,* 263 (2004) 394

[43]. J. Du, Y. Gao, L. Chai, G. Zou, Y. Li, Y. Qian, *Nanotechnology,* 17 (3006) 4923

[44]. Z. Hu, G. Oskam, R. L. Penn, N. Pesika, P. C. Searson, *J. Phys. Chem. B,* 107 (2003) 3124

[45]. X. Li, L. Zhou, J. Gao, H. Miao, H. Zhang, J. Xu, *Powder Technology*. 190 (2009) 324

[46]. Y. Al-Degs, M. A. Khraisheh, M. F. Tutunji, *Water Res.*, 35 (2001) 3724

[47]. H.-J. Fan, P. R. Anderson, *Sep. Purif. Technol.*, 45 (2005) 61

[48]. J. de Ruddera, T.V. de Wielea, W. Dhoogeb, F. Comhaireb, W. Verstraetea, *Water Res.*, 38 (2004) 184.

[49]. G. M. Hettiarachchi, G. M. Pierzynski, M. D. Ransom, *Environ. Sci. Technol*., 34 (2000) 4614

[50]. J. Ge, J. Qu, *J. Hazard. Mater.*, 100 (2003) 197

[51]. R. Liu, H. Tang, *Water Res.*, 34 (2000) 4029

[52]. E. Deschamps, V.S.T. Ciminelli, W.H. Holl, *Water Res.*, 39 (2005) 5212

[53]. Y. M. Sloker, A. M. Le Marechal, *Dyes Pigments*, 37 (1998) 335

[54]. M. A. Brown, S. C. De Vito, *Crit. Rev. Environ. Sci. Technol.* 23 (1993) 249

CHAPTER 2

BACKGROUND

2.1 Nanomaterials

2.1.1 Fundamental concepts

Nanotechnology is a new technology which has the potential to change the way we live, interact and communicate on a massive scale. It is expected to be the basis of many of the main technological innovations of the 21st century. Never before has there been a technology that has so much potential for the modern world. Research and development in this field is growing rapidly throughout the world. A major output of this activity is the development of new materials in the nanometer scale, including nanoparticles. Nanoparticles or nanocrystals made of metals, semiconductors, or oxides are of particular interest for their mechanical, electrical, magnetic, optical, chemical and other properties. Nanoparticles have been used as quantum dots and as chemical catalysts such as nanomaterial-based catalysts.

Nanoparticles are of great scientific interest as they are effectively a bridge between bulk materials and atomic or molecular structures. A bulk material should have constant physical properties regardless of its size, but at the nano-scale this is often not the case. For example, the bending of bulk copper (wire, ribbon etc.) occurs with movement of copper atoms/clusters at about the 50 nm scale. Copper nanoparticles smaller than 50 nm are considered super hard materials that do not exhibit the same malleability and ductility as bulk copper. A material such as gold, which is chemically inert at normal scales, can serve as a potent chemical catalyst at nanoscales. Much of the fascination with nanotechnology stems from these quantum and surface phenomena that matter exhibits at the nanoscale.

Although a broad definition, nanomaterials are those which have structured components with at least one dimension less than 100 nm. Materials that have one dimension in the nanoscale (and are extended in the other two dimensions) are layers, such as thin films or surface coatings. Some of the features on computer chips come in this category. Materials that are nanoscale in two dimensions (and extended in one

dimension) include nanowires and nanotubes. Materials that are nanoscale in three dimensions are particles, for example precipitates, colloids and quantum dots (tiny particles of semiconductor materials). Nanocrystalline materials, made up of nanometre-sized grains, also fall into this category.

2.1.2 Properties of nanomaterials

The unique properties of various types of intentionally produced nanomaterials give them novel electrical, catalytic, magnetic, mechanical, thermal or imaging features that are highly desirable for applications in commercial, medical, military and environmental sectors. The material properties of nanostructures are different from the bulk due to the high surface area over volume ratio and possible appearance of quantum effects at the nanoscale. As a particle decreases in size, a greater proportion of atoms are found at the surface compared to those inside. For example, a particle of size 30 nm has 5% of its atoms on its surface, at 10 nm 15% of its atoms, and at 3 nm 50% of its atoms. Thus nanoparticles have a much greater surface area per unit mass compared with larger particles. As growth and catalytic chemical reactions occur at surfaces, this means that a given mass of material in nanoparticulate form will be much more reactive than the same mass of material made up of larger particles.

In tandem with surface-area effects, quantum effects can begin to dominate the properties of matter as size is reduced to the nanoscale. These can affect the optical, electrical and magnetic behavior of materials, particularly as the structure or particle size approaches the smaller end of the nanoscale. The large surface area to volume ratio results in a substantial proportion of atoms having different magnetic coupling with neighboring atoms leading to differing magnetic properties. For instance, bulk gold and platinum are non magnetic but at the nano-size they act as magnetic particles. Au nanoparticles become ferromagnetic when they are capped with the appropriate molecules such as thiol. Semiconductors and many metals show large changes in optical properties such as color, as a function of particle size. Colloidal

suspensions of gold nanoparticles have a deep red color which becomes progressively more yellow as the particle size increases.

2.1.3 Classification of nanomaterials

There are many types of intentionally produced nanomaterials and the most current nanomaterials could be organized into four types: carbon based materials, metal based materials, dendrimers and composites. Carbon based materials are composed mostly of carbon, most commonly taking the form of a hollow spheres, ellipsoids or tubes. Spherical and ellipsoidal carbon nanomaterials are referred to as fullerenes, while cylindrical ones are called nanotubes. These particles have many potential applications, including improved films and coatings, stronger and lighter materials, and applications in electronics.

Metal based materials include quantum dots, nanogold, nanosilver and metal oxides, such as titanium dioxide. A quantum dot is a closely packed semiconductor crystal comprised of hundreds or thousands of atoms, and whose size is in the order of a few nanometers to a few hundred nanometers. Changing the size of quantum dots changes their optical properties.

Dendrimers nanomaterials are nanosized polymers built from branched units. The surface of a dendrimer has numerous chain ends, which can be tailored to perform specific chemical functions. This property could also be useful for catalysis. Also, because three-dimensional dendrimers contain interior cavities into which other molecules could be placed, they may be useful for drug delivery.

Composites combine nanoparticles with other nanoparticles or with larger, bulk-type materials. Nanoparticles, such as nanosized clays, are already being added to products ranging from auto parts to packaging materials, to enhance mechanical, thermal, barrier, and flame-retardant properties.

2.1.4 Synthesis of nanoparticles

Fabrication of nanomaterials with strict control over size, shape, and crystalline structure has become very important for the applications of nanotechnology in numerous fields including catalysis, medicine, and electronics. Synthesis methods for nanoparticles are typically grouped into two categories: "top-down" and "bottom-up" approach. The first involves the division of a massive solid into smaller and smaller portions, successively reaching to nanometer size. This approach may involve milling or attrition. The second, "bottom-up", method of nanoparticle fabrication involves the condensation of atoms or molecular entities in a gas phase or in solution to form the material in the nanometer range. The latter approach is far more popular in the synthesis of nanoparticles owing to several advantages associated with it. Fig. 2.1 shows the general overview of the two approaches.
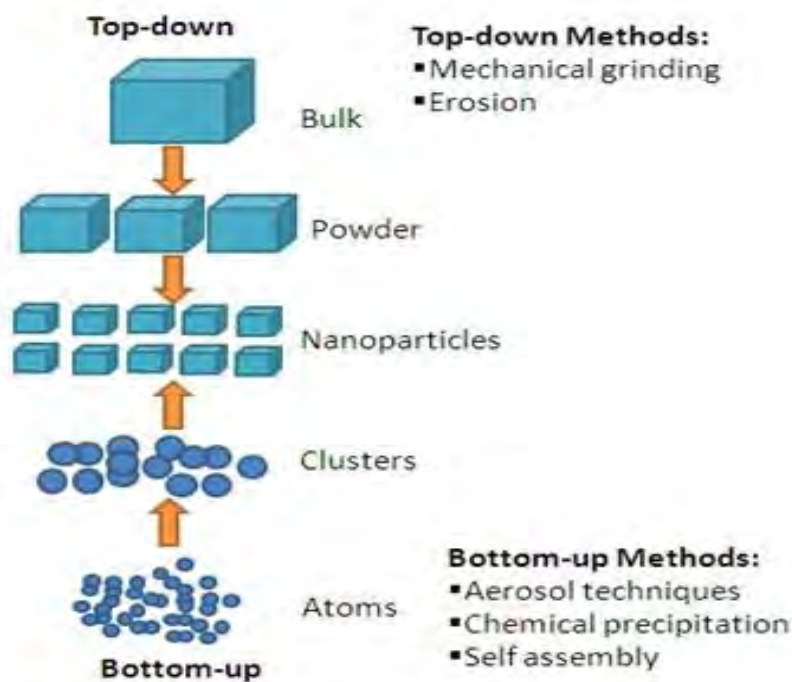
Fig. 2.1: Schematic of bottom-up and top-down approaches

There are many bottom up methods of synthesizing metal oxide nanomaterials, such as hydrothermal [1, 2], combustion synthesis [3], gas-phase methods [4], microwave synthesis [5] and sol-gel processing [6]. Sol-gel processing techniques will be discussed in detail here because the materials reported in this dissertation were synthesised using this method. However, an overview of other techniques usually employed for the synthesis of nanomaterials is also discussed hereunder.

2.1.4.1 Combustion route

Combustion synthesis leads to highly crystalline particles with large surface areas [7, 8]. The process involves a rapid heating of a solution containing redox groups [9]. During combustion, the temperature reaches approximately 650 °C for one or two minutes making the material crystalline.

2.1.4.2 Hydrothermal method

Hydrothermal synthesis is typically carried out in a pressurized vessel called an autoclave with the reaction in aqueous solution [10]. The temperature in the autoclave can be raised above the boiling point of water, reaching the pressure of vapor saturation. Hydrothermal synthesis is widely used   for   the preparation of metal oxide nanoparticles which can easily be obtained through hydrothermal treatment of peptized precipitates of a metal precursor with water [10, 11]. The hydrothermal method can be useful to control grain size, particle morphology, crystalline phase and surface chemistry through regulation of the solution composition, reaction temperature, pressure, solvent properties, additives and aging time [9].

2.1.4.3 Gas phase methods

Gas phase methods are ideal for the production of thin films. Gas phase synthesis can be carried out chemically or physically. Chemical Vapor Deposition (CVD) is a widely used industrial technique that can coat large areas in a short space of time [9].

During the procedure, metal oxide is formed from a chemical reaction or decomposition of a precursor in the gas phase [12, 13].

Physical Vapor Deposition (PVD) is another thin film deposition technique. The process is similar to Chemical Vapor Deposition (CVD) except that the raw materials/precursors, i.e., the material that is going to be deposited starts out in solid form, whereas in CVD, the precursors are introduced to the reaction chamber in the gaseous state. The process proceeds atomistically and mostly involves no chemical reactions. Various methods have been developed for the removal of growth species from the source or target. The thickness of the deposits can vary from angstroms to millimeters. In general, these methods can be divided into two groups: evaporation and sputtering. In evaporation, the growth species are removed from the source by thermal means. In sputtering, atoms or molecules are dislodged from solid target through impact of gaseous ions (plasma) [14].

2.1.4.4 Microwave synthesis

Microwave synthesis is relatively new and an interesting technique for the synthesis of oxide materials [15]. Various nanomaterials have been synthesized in remarkably short time under microwave irradiation [16, 17]. Microwave techniques eliminate the use of high temperature calcination for extended periods of time and allow for fast, reproducible synthesis of crystalline metal oxide nanomaterials. Utilizing microwave energy for the thermal treatment generally leads to a very fine particle in the nanocrystalline regime because of the shorter synthesis time and a highly focused local heating.

2.1.4.5 Sol-gel method

The sol-gel process is a capable wet chemical process to make ceramic and glass materials. This synthesis technique involves the conversion of a system from a colloidal liquid, named sol, into a semi-solid gel phase [18-20]. The sol-gel technology can be used to prepare ceramic or glass materials in a wide variety of

forms: ultra-fine or spherical shaped powders, thin film coatings, ceramic fibres, microporous inorganic membranes, monolithics, or extremely porous aerogels. An overview of the sol-gel process is illustrated in Fig. 2.2.
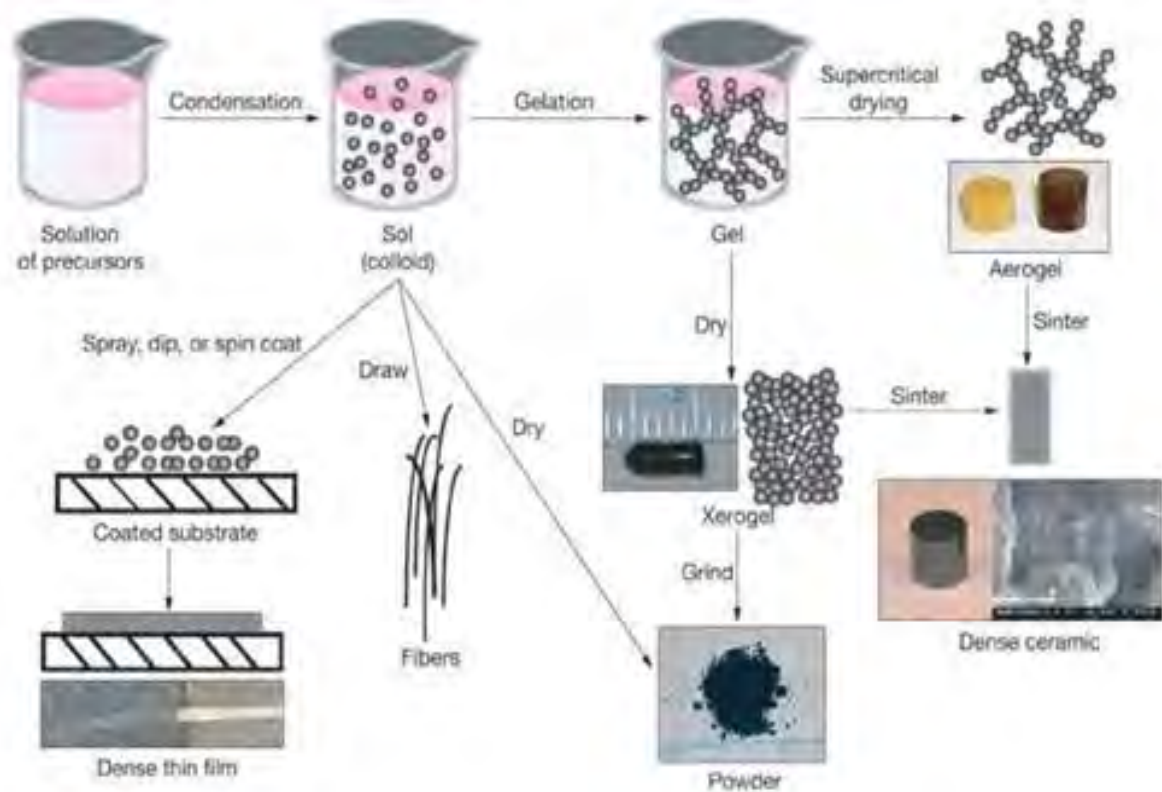
Fig. 2.2: Mechanism of sol-gel process

This technique offers many advantages including the low processing temperature, the ability to control the composition on molecular scale and the porosity to obtain high surface area materials, the homogeneity of the final product up to atomic scale. Moreover, it is possible to synthesize complex composition materials, to form higher purity products through the use of high purity reagents. The sol-gel process allows obtaining high quality films up to micron thickness, difficult to obtain using the physical deposition techniques. Moreover, it is possible to synthesize complex composition materials and to provide coatings over complex geometries [18-20].

The starting materials used in the preparation of the sol are usually inorganic metal salts or metal organic compounds, which by hydrolysis and polycondensation reactions form the sol [18-20]. Further processing of the sol enables one to make ceramic materials in different forms. Thin films can be produced by spin-coating or dip-coating. When the sol is cast into a mould, a wet gel will form. By drying and heat-treatment, the gel is converted into dense ceramic or glass materials. If the liquid in a wet gel is removed under a supercritical condition, a highly porous and extremely low density aerogel material is obtained. As the viscosity of a sol is adjusted into a suitable viscosity range, ceramic fibers can be drawn from the sol. Ultra-fine and uniform ceramic powders are formed by precipitation, spray pyrolysis, or emulsion techniques.

2.1.5 Characterization of nanomaterials

Characterization of nanomaterials with strict control over size, shape, and crystalline structure has become very important for the applications of nanotechnology in numerous fields including catalysis, medicine, and electronics etc. Characterization is done by using a variety of different techniques such as Electron Microscopy (Transmission Electron Microscopy, TEM and Scanning Electron Microscopy, SEM), Atomic Force Microscopy (AFM), Dynamic Light Scattering (DLS), Electron Spectroscopy (Energy dispersive X-ray spectroscopy, EDS and X-ray Photoelectron Spectroscopy, XPS), powder X-ray Diffractometry (XRD), UV-Visible spectroscopy, and Fourier Transform Infrared, FTIR spectroscopy, etc.

Whilst the theory has been known for over a century, the technology for Nanoparticle Tracking Analysis (NTA) allows direct tracking of the Brownian motion and this method therefore allows the sizing of individual nanoparticles in solution.

2.1.6 Nanoparticle morphology

Morphology of nanostructures includes the combined characteristics of nanoobjects including their size, shape and spatial organization (aggregate structure). Morphology of different nanostructures may vary significantly depending on their material composition, crystal structure and manufacturing method. Existing synthesis methods allow the production of nanoparticles with a variety of shapes (spheres, rods, tubes, needles, cubes, octahedrons, etc.) and sizes. For example, variation of such hydrothermal synthesis parameters as temperature, pressure, reagent concentration, treatment time and pH results in different morphologies, compositions and crystallinity of products [21]. The morphological diversity of nanoscale objects built with organic molecules is almost infinite. For example, present-day biotechnologies using self-assembling duplex DNA as building blocks lead to the controllable synthesis of three-dimensional structures sized between 10 nm and 100 nm. One of these techniques was used to create nanoscale "DNA origami": polygon frameworks, gears, bridges, bottles, etc. [22, 23]. Morphology variation is an effective way of controlling functionality of nanomaterials that also affects their biocompatibility, because it is, in fact, a reflection of the product of surface (interface) evolution (transformation) in the process of making a material. Morphological diversity is of paramount importance specifically for nanomaterials, while these materials usually contain a large number of surface atoms that determine their physical and chemical properties. On the other hand, most nanomaterials are thermodynamically unstable, and their nonequilibrium morphologies (different from the shape of monocrystals of a given substance) correspond to local minimums of free energy of the system.

Morphology of α-Fe$_2$O$_3$ nanoparticles generated through hydrothermal treatment of ferrous oxide (III) in different concentrations in the presence of a surfactant (CTAB) is shown in Fig. 2.3.
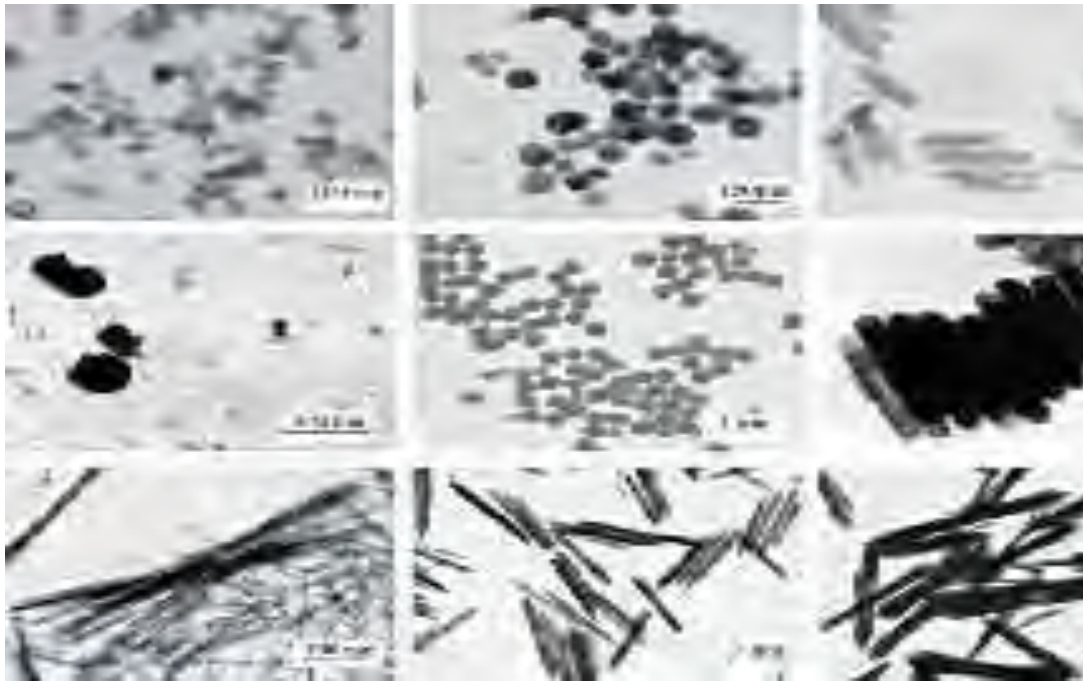
Fig. 2.3: Morphology of α-Fe_2O_3 nanoparticles generated through hydrothermal treatment of ferrous oxide (III) in different concentrations in the presence of a surfactant (CTAB) [21].

2.1.7 Crystal structure of nanomaterials

In mineralogy and crystallography, a crystal structure is a unique arrangement of atoms or molecules in a crystalline liquid or solid. A crystal structure describes a highly ordered structure, occurring due to the intrinsic nature of molecules to form symmetric patterns. A crystal structure can be thought of as an infinitely repeating array of 3D 'boxes', known as unit cells. The unit cell is calculated from the simplest possible representation of molecules, known as the asymmetric unit. The asymmetric unit is translated to the unit cell through symmetry operations, and the resultant crystal lattice is constructed through repetition of the unit cell infinitely in 3-dimensions. Patterns are located upon the points of a lattice, which is an array of points repeating periodically in three dimensions. The lengths of the edges of a unit cell and the angles between them are called the lattice parameters.

2.1.7.1 Unit cell

The crystal structure of a material (the arrangement of atoms within a given type of crystal) can be described in terms of its unit cell. The unit cell is a small box containing one or more atoms arranged in 3-dimensions. The unit cells stacked in three-dimensional space describes the bulk arrangement of atoms of the crystal. The unit cell is represented in terms of its lattice parameters, which are the lengths of the cell edges (a, b and c) and the angles between them (alpha, beta and gamma)

2.1.7.2 Miller indices

The reciprocals of the fractional intercepts which the plane makes with the crystallographic axes are known as Miller indices (h, k, l) and shown in Fig. 2.4.
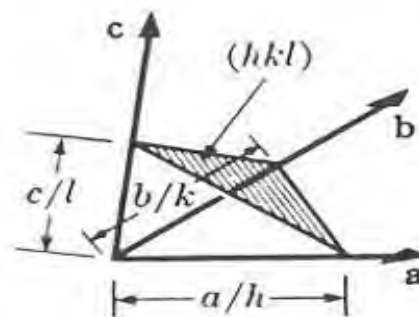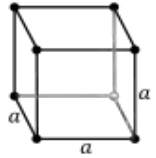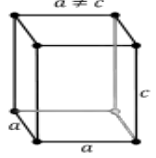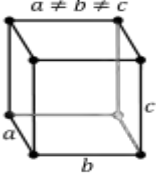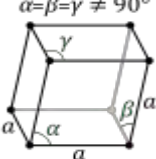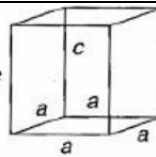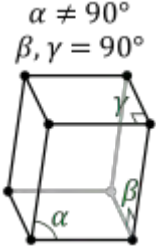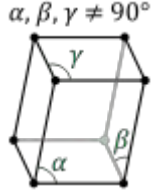
Fig. 2.4: Miller indices

If one or more of the indices is zero, it means that the planes do not intersect that axis (i.e., the intercept is "at infinity").

2.1.7.3 Lattice systems

The lattice systems are a grouping of crystal structures according to the axial system used to describe their lattice. Each lattice system consists of a set of three axes in a particular geometric arrangement. There are seven lattice systems:

Table 2.1: Seven crystal systems

System	Lattice Constants and Angles	Unit Cell Geometry
Cubic	$a = b = c,$ $\alpha = \beta = \gamma = 90°$	
Tetragonal	$a = b \neq c,$ $\alpha = \beta = \gamma = 90°$	
Orthorhombic	$a \neq b \neq c,$ $\alpha = \beta = \gamma = 90°$	
Rhombohedral	$a = b = c,$ $\alpha = \beta = \gamma \neq 90°$	
Hexagonal	$a = b \neq c,$ $\alpha = \beta = 90°, \gamma = 120°$	
Monoclinic	$a \neq b \neq c,$ $\beta = \gamma = 90°, \neq \alpha$	
Triclinic	$a \neq b \neq c,$ $\alpha \neq \beta \neq \gamma \neq 90°$	

2.1.8 Applications of nanoparticles

Since nanomaterials possess unique, beneficial chemical, physical, and mechanical properties, they can be used for a wide variety of applications. These applications include, but are not limited to the following:

2.1.8.1 Medicine

Nanotechnology in medicine (sometimes referred to as *nanomedicine*) involves techniques already being used or currently under development, as well as longer range research into the use of manufactured nano-robots to make repairs at the cellular level. Nanomedicine could revolutionize the way we detect and treat damage to the human body and disease.

i) Earlier detection

We know that the earlier a disease can be detected, the easier it is to remedy. To achieve this, research is focusing on introducing into the body specially designed nanoparticles. These nanoparticles are composed of tiny fluorescent 'quantum dots' that are 'bound' to targeting antibodies. In turn, these antibodies bind to diseased cells. When this happens, the quantum dots fluoresce brightly. This fluorescence can be picked up by new, specially developed, advanced imaging systems, enabling the accurate pinpointing of a disease even at a very early stage.

ii) Faster diagnosis

Nanotechnology is also leading to faster diagnosis. Diagnosis can be a lengthy and stressful business, usually with a test sample having to be sent away for analysis. The results can take several days or even weeks to arrive. Nanotechnology is enabling much faster and more precise diagnosis, as many tests can be built into a single, often palm-sized device that only requires tiny quantities of sample. This device is

sometimes called a 'lab-on-a-chip', and samples can be processed and analyzed so rapidly that the results can be read out almost instantaneously.

iii) Targeted drug delivery

People often complain that the cure for a disease can feel almost as bad as the disease itself, as prescription drugs may have unpleasant side effects. This is because the body needs to be flooded with very high doses of a drug in order to ensure that a sufficient volume reaches the site of the disease. Accurate targeting of the drug can now be achieved, using specially designed drug-carrying nanoparticles. This also means that much smaller quantities of a drug are necessary, reducing toxicity to the body. The drug is then activated only at the disease site (such as a tumour) by light or other means, and the progress of the cure can also be monitored using advanced imaging techniques.

iv) Anti-microbial techniques

Researchers are attempting to use nanotechnology-based techniques to develop new methods for fighting bacterial infections. Nanoparticles can help fight staph infections, burns, and other conditions eradicating or avoiding bacterial infection. It's possible that these nano-techniques could remove bacterial infection in minutes, rather than in weeks as is currently the case with antibiotics.

v) Nanorobots

Many future applications of nanomedicine will be based on the ability to build and develop nanorobots. In the future these nanorobots could actually be programmed to repair specific diseased cells, functioning similarly to antibodies in our natural healing processes.

2.1.8.2 Environment

Nanotechnology is being used in several applications to improve the environment. This includes cleaning up existing pollution, improving manufacturing methods to reduce the generation of new pollution, and making alternative energy sources more cost effective. In trying to help our ailing environment, nanotechnology researchers and developers are pursuing the following avenues:

i) Air pollution

There are two major ways in which nanotechnology is being used to reduce air pollution: catalysts and nano-structured membranes.

Catalysts can be used to enable a chemical reaction (which changes one type of molecule to another) at lower temperatures or make the reaction more effective. Nanotechnology can improve the performance and cost of catalysts used to transform vapors escaping from cars or industrial plants into harmless gasses. That's because catalysts made from nanoparticles have a greater surface area to interact with the reacting chemicals than catalysts made from larger particles. The larger surface area allows more chemicals to interact with the catalyst simultaneously, which makes the catalyst more effective.

Nanostructured membranes, on the other hand, are being developed to separate carbon dioxide from industrial plant exhaust streams. The plan is to create a method that can be implemented in any power plant without expensive retrofitting.

Examples of nanoparticle catalysts and nano-structured membranes in reducing air pollution can be mentioned here. Gold nanoparticles embedded in a porous manganese oxide as a room temperature catalyst was used to breakdown volatile organic compounds in air. Crystals containing nanosized pores was used to trap carbon dioxide. Nanocatalyst containing cobalt and platinum was used to remove nitrogen oxide from smokestacks. Carbon nanotube based membranes, nanostructured

membranes, genetically engineered enzymes can be used for removal of carbon dioxide from industrial smoke stacks.

ii) Water pollution

Nanotechnology is being used to develop solutions to three very different problems in water quality. One challenge is the removal of industrial water pollution, such as a cleaning solvent called TCE, from ground water. Nanoparticles can be used to convert the contaminating chemical through a chemical reaction to make it harmless. Studies have shown that this method can be used successfully to reach contaminates dispersed in underground ponds and at much lower cost than methods which require pumping the water out of the ground for treatment.

Another challenge is the removal of salt or metals from water. A deionization method using electrodes composed of nano-sized fibers shows promise for reducing the cost and energy requirements of turning salt water into drinking water.

The third problem concerns the fact that standard filters do not work on virus cells. A filter only a few nanometers in diameter is currently being developed that should be capable of removing virus cells from water.

Followings are the potential of nanotechnology in removing contaminates from water. Using nanoscavengers, in which a layer of reactive nanoparticles coat a synthetic core which is designed to be easily magnetized. The nanoparticles, for example silver nanoparticles if bacteria is a problem, attach to or kill the pollutants. Then when a magnetic field is applied the nanoscavengers are removed from the water.

Pellets containing nanostructured palladium and gold were used as a catalyst to breakdown chlorinated compounds contaminating groundwater. Since palladium is very expensive the researchers formed the pellets of nanoparticles that allow almost

every atom of palladium to react with the chlorinated compounds, reducing the cost of the treatment.

Graphene oxide can be used to remove radioactive material from water. Flakes of graphene oxide absorb radioactive ions in water. The graphene oxide then forms clumps that can be removed from the water for disposal. Graphene can also be used as a membrane for low cost water desalination. Researchers have determined that graphene with holes the size of a nanometer or less can be used to remove ions from water. They believe this can be used to desalinate sea water at a lower cost than the reverse osmosis techniques currently in use.

Carbon nanotubes are used as the pores in reverse osmosis membranes. This can decrease the power needed to run reverse osmosis desalination plants because water molecules pass through carbon nanotubes more easily than through other types of pores. Other researchers are using carbon nanotubes to develope small, inexpensive water purification devices needed in developing countries.

2.1.8.3 Energy

Nanotechnology is being used in several applications to improve the efficiency of energy generation or develop new methods to generate energy. Here are some interesting ways that are being explored using nanotechnology to produce more efficient and cost-effective energy:

i) Creating steam from sunlight

Sunlight, concentrated on nanoparticles, can produce steam with high energy efficiency. The efficiency of solar steam is due to the light-capturing nanoparticles that convert sunlight into heat. When submerged in water and exposed to sunlight, the particles heat up so quickly they instantly vaporize water and create steam. The "solar steam device" is intended to be used in areas of developing countries without

electricity for applications such as purifying water or disinfecting dental instruments.

ii) Producing high efficiency light bulbs

A nano-engineered polymer matrix is used in a new style of high efficiency light bulbs. The bulbs produce white light, similar to sunlight and can be made in any shape. The new bulbs have the advantage of being shatterproof and twice the efficiency of compact fluorescence light bulbs.

iii) Increasing the electricity generated by windmills

An epoxy containing carbon nanotubes is being used to make windmill blades. Stronger and lower weight blades are made possible by the use of nanotube-filled epoxy. The resulting longer blades increase the amount of electricity generated by each windmill.

iv) Generating electricity from waste heat

Sheets of nanotubes are used to build thermocells that generate electricity when the sides of the cell are at different temperatures. These nanotube sheets could be wrapped around hot pipes, such as the exhaust pipe of a car, to generate electricity from heat that is usually wasted.

v) Storing hydrogen for fuel cell powered cars

Graphene layers are used to increase the binding energy of hydrogen to the graphene surface in a fuel tank, resulting in a higher amount of hydrogen storage and therefore a lighter weight fuel tank. It is also demonstrated that sodiumborohydride nanoparticles can effectively store hydrogen.

vi) Reducing power loss in electric transmission wires

Wires containing carbon nanotubes are developed that would have significantly lower resistance than the wires currently used in the electric transmission grid. These upgraded transmission wires, which could transmit electricity thousands of miles with insignificant power losses, with local electricity storage capacity in the form of batteries in each building that could store power for 24 hours use.

vii) Reducing the cost of solar cells

Nanotech solar cells reduced manufacturing costs as a result of using a low temperature process similar to printing instead of the high temperature vacuum deposition process typically used to produce conventional cells made with crystalline semiconductor material. **It also** reduced installation costs achieved by producing flexible rolls instead of rigid crystalline panels. Cells made from semiconductor thin films will also have this characteristic.

viii) Improving the performance of batteries

With the growth in portable electronic equipment (mobile phones, laptop computers, remote sensors), there is great demand for lightweight, high energy density batteries. Nanocrystalline materials synthesized by sol–gel techniques are candidates for separator plates in batteries because of their foam-like (aerogel) structure, which can hold considerably more energy than conventional ones. Nickel–metal hydride batteries made of nanocrystalline nickel and metal hydrides are envisioned to require less frequent recharging and to last longer because of their large surface area.

ix) Improving the efficiency and reducing the cost of fuel cells

Catalysts are used with fuels such as hydrogen or methanol to produce hydrogen ions. Platinum, which is very expensive, is the catalyst typically used in this process.

Nanotechnology is being used to reduce the cost of catalysts used in fuel cells. Now nanoparticles of platinum are used to reduce the amount of platinum needed, or nanoparticles of other materials are used to replace platinum entirely and thereby lower costs.

2.1.8.4 Consumer products

Nano has already found its way into lots of products we use every day, from clothing to tennis racquets. In fact, if we strolled around our home we'd probably find dozens of products manufactured using some kind of nanotechnology.

i) Sunscreens and cosmetics

The traditional chemical UV protection approach suffers from its poor long-term stability. A sunscreen based on mineral nanoparticles such as titanium dioxide offer several advantages. Titanium oxide nanoparticles have a comparable UV protection property. Nanosized titanium dioxide and zinc oxide are currently used in some sunscreens, as they absorb and reflect ultraviolet (UV) rays and yet are transparent to visible light and so are more appealing to the consumer. Nanosized iron oxide is present in some lipsticks as a pigment. The use of nanoparticles in cosmetics has raised a number of concerns about consumer safety.

ii) Foods

Nanotechnology can be applied in the production, processing, safety and packaging of food. A nanocomposite coating process could improve food packaging by placing anti-microbial agents directly on the surface of the coated film. Nanocomposites could increase or decrease gas permeability of different fillers as is needed for different products. They can also improve the mechanical and heat resistance properties and lower the oxygen transmission rate.

iii) Textiles and sports apparel

A new breed of clothing is emerging out of nanotechnology which are water repellant, UV-protective, anti-bacterial, anti-static and wrinkle resistance. Running shoes, tennis racquets, golf balls and a range other sporting goods have also been enhanced by nanotechnology. Such high performance materials require very little maintenance making. There has been much experimentation with nano-enhanced textiles in extreme environments for exploring its use in fire, space, war and intense UV light. Silver nanoparticles, for example, provide antibacterial properties while platinum and palladium decompose harmful gases or toxic chemicals. The nanocomposites have pushed down the weight of most sports gear, with a manifold increase in strength.

2.1.8.5 Construction

Nanotechnology has the potential to make construction faster, cheaper and safer. Automation of nanotechnology construction can allow for the creation of structures from advanced homes to massive skyscrapers much more quickly and at much lower cost. The Silica (SiO_2) is present in conventional concrete as part of the normal mix. When nano silica is added to concrete the particle packing can be improved mechanical properties. The addition of nano silica to cement based materials can also control the degradation of the fundamental C-S-H (calcium silicate hydrate) reaction of concrete caused by calcium leaching in water as well as block water penetration and therefore lead to improvements in durability. The strength of concrete can also be increase by adding haematite (Fe_2O_3) nanoparticles.

Steel has been widely available material and has a major role in the construction industry. The use of nanotechnology in steel helps to improve the properties of steel. The nano size steel produce stronger steel cables which can be used in bridge construction.

The glass is also an important material in construction. There is a lot of research being carried out on the application of nanotechnology to glass. Titanium dioxide (TiO_2) nanoparticles are used to coat glazing since it has sterilizing and anti-fouling properties. The particles catalyze powerful reactions which breakdown organic pollutants, volatile organic compounds and bacterial membranes. Most of glass in construction is on the exterior surface of buildings. So the light and heat entering the building through glass has to be prevented. The nanotechnology can provide a better solution to block light and heat coming through windows. Coatings are an important area in construction. Coatings are extensively used to paint the walls, doors and windows.

Coatings should provide a protective layer which is bound to the base material to produce a surface of the desired protective or functional properties. Nanotechnology is being applied to paints to obtain the coatings having self healing capabilities and corrosion protection under insulation. These coatings are hydrophobic and repel water from the metal pipe and can also protect metal from salt water attack.

2.1.8.6 Electronics

Continuing advances in electronics have lead to increasingly miniaturized systems and components; nanotechnology has several electronic applications, allowing scientists to produce smaller, more energy-efficient and better-performing transistors and related devices.

i) Quantum dot

Certain types of light-emitting diodes, or LEDs, use a nanotechnology called quantum dots. These are tiny clusters of compounds such as zinc sulfide or cadmium selenide that range in size from 2 to 10 nanometers in diameter and contain about 50 atoms. These clusters produce light under electrical stimulation. The size of the quantum dot

dictates the wavelength of the light and therefore its color- small ones produce blue light and larger ones create red light. Quantum dots find their way into devices for lighting and video displays.

ii) Buckytube transistors

Computers, smart phones and other high-tech devices would not be possible without extreme miniaturization of transistors and other components; micron-scale transistors used in the integrated circuits of the 1980s and 1990s have given way to those measuring dozens of nanometers. Electronics manufacturers encounter great difficulties in shrinking these devices further, though nanotechnology may offer hope. Scientists have designed working transistors made of "buckytubes," tubes of pure carbon that measure less than 10 nanometers in diameter. These buckytube transistors have better power and speed characteristics than traditional silicon designs.

iii) Memory

Memory is an electronic component essential to modern digital devices. Nanotechnology approaches to data storage promise greater capacities in smaller packages than traditional technologies. One example of nanotechnology-based computer storage is "millipede memory," an array of sharp tips that write data bits as dimples in a plastic surface; the dimples measure 10 to 40 nanometers in diameter, giving a storage density of one trillion bits per square inch.

iv) Nanowires

Nanowires are thin electrical conductors measuring only a few atoms across. Whereas manufacturers make traditional wires by pulling copper until it becomes very thin, nanowires are grown like crystals from a metal "seed". Nanowires are potentially useful in display screens for laptop computers and cell phones; they carry electrical current to tiny elements in the display, yet are invisibly thin and allow light to pass through.

2.1.8.7 Catalysis

In general, nanoparticles have a high surface area, and hence provide higher catalytic activity. Catalysis is important for the production of chemicals. Nanoparticles serve as an efficient catalyst for some chemical reaction, due to the extremely large surface to volume ratio. Platinum nanoparticles are now being considered in the next generation of automotive catalytic converters because the very high surface area of nanoparticles could reduce the amount of platinum required. Some chemical reactions are also carried out using nanomaterials. For example, reduction of nickel oxide to the base metal Ni.

2.2 Metal oxides nanomaterials

In periodic table more than 75% of elements are metallic in nature such as gold, silver, platinum, mercury, uranium, aluminum, sodium, calcium etc. The metallic compounds which are formed with metal and oxygen in the form of oxide ion (O^{2-}) are called as metal oxide. Metal oxides represent an appealing and assorted class of materials whose properties cover the entire range from metals to semiconductors to insulators and almost all aspects of material science, chemistry, and physics in a very broad application area. In the past few years, progress has been made on the synthesis, structural, physical, and chemical characterization of self-assembled and hierarchically assembled metal oxide nanostructures that exhibit size-dependent properties. The field of metal-oxide nanostructured morphologies (e.g., nanowires, nanorods, and nanotetrapods) has become one of the most active research areas within the nanoscience community. New fundamental research is paralleled with original and inspired potential applications, including nanowire electronics and photonics, nanowires as electron sources, nanowires for energy conversion and storage, nanowires interfacing with living cells, and single-nanowire devices.

2.2.1 Oxides of manganese

Manganese (Mn) is the 10th most abundant element in the earth's crust and second only to iron as the most common heavy metal; on average crustal rocks contain about 0.1% Mn [24]. It occurs in natural systems mainly in three different oxidation states: +2, +3, and +4, giving rise to a range of multivalent phases. The most available oxides of manganese are MnO, Mn_3O_4, Mn_2O_3, MnO_2 and Mn_5O_8. The structural properties of these oxides are listed in Table 2.2

Table 2.2: Structural properties of different oxides of Mn

Oxide	MnO	Mn_3O_4	Mn_5O_8	Mn_2O_3	MnO_2
Mineral Name	Manganosite	Hausmannite	n/a	Bixbyte	Pyrolusite
Oxidation Number	+2	+2, +3	+2, +4	+3	+4
Crystal Structure	Cubic	Tetragonal	Monoclinic	Cubic	Tetragonal
Lattice Parameter	a = 4.446	a = 5.7621 c = 9.4696	a = 10. 392 b = 5.730 c = 4.866 β = 109.62	a = 9.409	a = 4.3999 c = 2.8740

2.3 Dyes

A dye is a colored substance that has an affinity to the substrate to which it is being applied. The dye is generally applied in an aqueous solution, and requires a mordant to improve the fastness of the dye on the fiber.

Both dyes and pigments appear to be colored because they absorb some wavelengths of light more than others. In contrast with a dye, a pigment generally is insoluble, and has no affinity for the substrate. Some dyes can be precipitated with an inert salt to produce a lake pigment.

Archaeological evidence shows that, particularly in India and Phoenicia, dyeing has been widely carried out for over 5,000 years. The dyes were obtained from animal, vegetable or mineral origin, with none to very little processing. By far the greatest source of dyes has been from the plant kingdom, notably roots, berries, bark, leaves and wood, but only a few have ever been used on a commercial scale.

2.3.1 Natural dye

The majority of natural dyes are from plant sources – roots, berries, bark, leaves, and wood, fungi, and lichens. Textile dyeing dates back to the Neolithic period. Throughout history, people have dyed their textiles using common, locally available materials. Scarce dyestuffs that produced brilliant and permanent colors such as the natural invertebrate dyes Tyrian purple and crimson kermes were highly prized luxury items in the ancient and medieval world. Plant-based dyes such as woad, indigo, saffron, and madder were raised commercially and were important trade goods in the economies of Asia and Europe. Across Asia and Africa, patterned fabrics were produced using resist dyeing techniques to control the absorption of color in piece-dyed cloth. Dyes from the New World such as cochineal and logwood were brought to Europe by the Spanish treasure fleets, and the dyestuffs of Europe were carried by colonists to America.

The discovery of man-made synthetic dyes late in the 19th century ended the large-scale market for natural dyes.

2.3.2 Synthetic dye

The first human-made organic dye, mauveine, was discovered serendipitously by William Henry Perkin in 1856, the result of a failed attempt at the total synthesis of quinine. Many thousands of synthetic dyes have since been prepared. Synthetic dyes quickly replaced the traditional natural dyes. They cost less, they offered a vast range of new colors, and they imparted better properties to the dyed materials. Dyes are now classified according to how they are used in the dyeing process.

2.3.3 Dye types

i) Acid dyes

This type of dyes are water-soluble anionic dyes that are applied to fibers such as silk, wool, nylon and modified acrylic fibers using neutral to acid dye baths. Attachment to the fiber is attributed, at least partly, to salt formation between anionic groups in the dyes and cationic groups in the fiber. Acid dyes are not substantive to cellulosic fibers. Most synthetic food colors fall in this category.

ii) Basic dyes

Basic dyes are water-soluble cationic dyes that are mainly applied to acrylic fibers, but find some use for wool and silk. Usually acetic acid is added to the dye bath to help the uptake of the dye onto the fiber. Basic dyes are also used in the coloration of paper.

iii) Direct or Substantive Dyeing

This type of dye is normally carried out in a neutral or slightly alkaline dye bath, at or near boiling point, with the addition of either sodium chloride ($NaCl$) or sodium sulfate (Na_2SO_4) or sodium carbonate (Na_2CO_3). Direct dyes are used on cotton, paper, leather, wool, silk and nylon. They are also used as pH indicators and as biological stains.

iv) Mordant dyes

Mordant dyes require a mordant, which improves the fastness of the dye against water, light and perspiration. The choice of mordant is very important as different mordants can change the final color significantly. Most natural dyes are mordant dyes and there is therefore a large literature base describing dyeing techniques. The most important mordant dyes are the synthetic mordant dyes, or chrome dyes, used for wool; these comprise some 30% of dyes used for wool, and are especially useful for black and navy shades. The mordant, potassium dichromate, is applied as an after-treatment. It is important to note that many mordants, particularly those in the heavy metal category, can be hazardous to health and extreme care must be taken in using them.

v) Vat dyes

Vat dyes are essentially insoluble in water and incapable of dyeing fibers directly. However, reduction in alkaline liquor produces the water soluble alkali metal salt of the dye, which, in this leuco form, has an affinity for the textile fiber. Subsequent oxidation reforms the original insoluble dye. The color of denim is due to indigo, the original vat dye.

vi) Reactive dyes

Reactive dyes utilize a chromophore attached to a substituent that is capable of directly reacting with the fiber substrate. The covalent bonds that attach reactive dye to natural fibers make them among the most permanent of dyes. "Cold" reactive dyes, such as Procion MX, Cibacron F, and Drimarene K are very easy to use because the dye can be applied at room temperature. Reactive dyes are by far the best choice for dyeing cotton and other cellulose fibers at home or in the art studio.

vii) Disperse dyes

Disperse dyes were originally developed for the dyeing of cellulose acetate, and are water insoluble. The dyes are finely ground in the presence of a dispersing agent and sold as a paste, or spray-dried and sold as a powder. Their main use is to dye polyester but they can also be used to dye nylon, cellulose triacetate, and acrylic fibers. In some cases, a dyeing temperature of 130 °C (266 °F) is required, and a pressurized dye bath is used. The very fine particle size gives a large surface area that aids dissolution to allow uptake by the fiber. The dyeing rate can be significantly influenced by the choice of dispersing agent used during the grinding.

viii) Azoic dyeing

This is a technique in which an insoluble azo dye is produced directly onto or within the fiber. This is achieved by treating a fiber with both diazoic and coupling components. With suitable adjustment of dye bath conditions the two components react to produce the required insoluble azo dye. This technique of dyeing is unique, in that the final color is controlled by the choice of the diazoic and coupling components. This method of dyeing cotton is declining in importance due to the toxic nature of the chemicals used.

ix) Food dye

One other class that describes the role of dyes, rather than their mode of use, is the food dye. Because food dyes are classed as food additives, they are manufactured to a higher standard than some industrial dyes. Food dyes can be direct, mordant and vat dyes, and their use is strictly controlled by legislation. Many are azo dyes, although anthraquinone and triphenylmethane compounds are used for colors such as green and blue. Some naturally-occurring dyes are also used.

2.3.4 Methylene blue

Methylene blue is a heterocyclic aromatic chemical compound with the molecular formula $C_{16}H_{18}N_3SCl$ and its IUPAC name is 3, 7-bis (Dimethylamino)-phenothiazin-5-ium chloride.
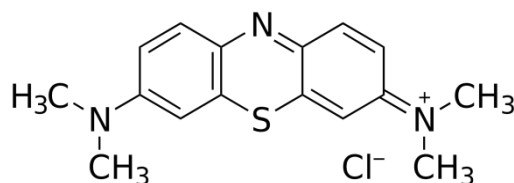
It has many uses in a range of different fields, such as biology and chemistry. At room temperature it appears as a solid, odorless, dark green powder that yields a blue solution when dissolved in water.

Methylene blue is widely used as a redox indicator in analytical chemistry. Solutions of this substance are blue when in an oxidizing environment, but will turn colorless if exposed to a reducing agent.

In biology methylene blue is used as a dye for a number of different staining procedures, such as Wright's stain and Jenner's stain. Since it is a temporary staining technique, methylene blue can also be used to examine RNA or DNA under the microscope or in a gel: as an example, a solution of methylene blue can be used to stain RNA on hybridization membranes in northern blotting to verify the amount of nucleic acid present. It can also be used as an indicator to determine if eukaryotic cells such as yeast are alive or not. The methylene blue is unable to penetrate viable cells leaving them unstained. However, dead cells are unable to keep the methylene blue from penetrating the cell membrane, staining the cells blue. Methylene blue can inhibit the respiration of the yeast as it picks up hydrogen ions made during the process and the yeast cell cannot then use those ions to release energy.

In the human body, methylene blue is highly stable; if ingested, it resists the stomach's acidic environment as well as the hydrolytic enzymes present. Methylene blue has some other adverse effect in human body that can be stated bellow [25, 26].

Cardiovascular	Central Nervous System	Dermatologic	Gastro-intestinal	Genito-urinary	Hemato-logic
• Hypertension • Precordial pain	•Dizziness • Mental confusion • Headache • Fever	• Staining of skin • Injection site necrosis (SC)	• Fecal discoloration • Nausea • Vomiting • Abdominal pain	• Discoloration of urine (doses over 80μg) • Bladder irritation	• Anemia

2.4 Literature review and plan of the present research

The synthesis of nanoparticles is a subject of intensive research in recent years due to their potential technological applications. Metal-oxide nanocrystals are expected to find useful applications in catalysis, magnetic data storage, energy storage and sensors [27-30]. In particular, metal-oxide nanocrystals are of great interest owing to their unique size dependent properties and excellent processability. Different forms of Mn-Oxide nanoparticles and their intriguing composites have potential applications in wastewater treatment, catalysis, sensors, super capacitors, rechargeable batteries and imaging technologies [31-35] due to their high theoretical capacity, low cost, environmental benignity, and special properties [36 - 38]. Very recently, several groups reported the synthesis of manganese oxides nanomaterials, characterization, variety of applications and oxidative study. Some of them are cited bellow:

H. Ying-Ying et al. [39] developed a method for the preparation of nanoporous Mn_3O_4 nanorods using ethanol and manganese acetate tetrahydrate. They found that

mesoporous Mn_3O_4 nanorods works as potential anode material for high performance Lithium-ion batteries.

M. Ristic et al. [40] prepared Hausmannite Mn_3O_4 nanoparticles following two procedures. One was based on the mixing of $Mn(NO_3)_2$ and NH_4OH solution and ageing of the suspensions obtained at 20°C. In the other process, the solution of $MnCl_2$, H_2O and NH_4OH were mixed and the suspensions obtained were aged at 20°C. They found that the phase composition of the precipitates is influenced by the order of adding H_2O or NH_4OH.

E. Karaoglue et al. [41] reported the synthesis of PEG-Mn_3O_4 nanocomposite via a hydrothermal route by using $Mn(acac)_2$, ethanol, NH_3 and PEG-400. They found that the conductivity and permittivity measurements strongly depend on the secondary thermal transition of nanocomposite beyond 100°C. Above that temperature, Mn_3O_4 particle may interact with each other yielding a percoalated path that will facilitate the conduction.

S. Rui eta al. [42] prepared Mn_3O_4 nanoparticles via a one step solvothermal route with $Mn(CH_3COO)_2.4H_2O$ as manganese source in the mixed solvent of acetone and water. They reported that acetone solvent plays an important role in the reaction as a weak reducing media. They also observed that the particle size of Mn_3O_4 nanocrystals becomes larger with the rising of solvothermal reaction temperature.

S. Xing et al. [43] prepared naanostructured Mn_3O_4 by oxidation – precipitation reaction of $Mn(NO_3)_2$ with citric acid. They found that with the increase of amount of citric acid the particle size is reduced and specific surface area was increased.

Tokeer Ahmed et al. [44] introduced nanorods of manganese oxalate as a single source precursor to different manganese oxide nanoparticles. Nanorods of anhydrous manganese oxalate were prepared by the reverse micellar method using CTAB as the surfactant. This precursor was then used to synthesize single phase nanoparticles of various manganese oxides such as MnO, Mn_2O_3, and Mn_3O_4 under specific reaction

conditions. Both MnO and α-Mn$_2$O$_3$ were established as cubic phase. α-Mn$_2$O$_3$ showed a weak antiferromagnetic transition (TN = 80 K), while the spinel Mn$_3$O$_4$ nano-particles showed a ferromagnetic transition at 43 K.

A low temperature synthesis of nanoparticles using manganese sulphate and hydrogen peroxide as strong materials was studied by Jin Mu et al. [45]. They established a solution method for preparing nanoparticles by using starch as capping agent. The distinct advantage of their method was avoiding the agglomeration of particles in high temperature treatment.

Ning Wang et al. [46] reported the synthesis of high quality tetragonal Mn$_3$O$_4$ nanoparticles and the large scale assembly of the nanoparticles into a wall-like pattern by using a mid solution method at 60°C without any post treatment modification. This made free spatial arrangement possible. They have also investigated the magnetic properties of the as-grown Mn$_3$O$_4$ nanopatterns by using the superconducting quantum interference devices.

Procedures for the preparation of Mn$_3$O$_4$ nanoparticles (about 20nm) or elongated α-MnOOH particles with length less than 2 μm and width 0.4 μm or less were described by M. Ocana [47]. Forced hydrolysis of aqueous manganese (II) acetate solutions was performed in the absence of HCl to obtain Mn$_3$O$_4$ and in the presence of HCl to obtain α-MnOOH. These solids were only produced under a very restricted range of reagent concentrations involving solutions of 0.2-0.4M manganese (II) acetate for Mn$_3$O$_4$ and of 1.6-2.0 M Mn (II) and 0.2-0.3 M HCl for α-MnOOH at low temperature (80°C).

Won Seok Seo et al. [48] reported a single reliable synthesis of size focused colloidal nanocrystals of two different manganese oxides, Mn$_3$O$_4$ and MnO from thermal decomposition of a single precursor manganese acetylacetonate in oleylamine. They also studied the size-dependent magnetic properties of colloidal Mn$_3$O$_4$ and MnO nanoparticles.

A versatile, convenient and nontoxic solvothermal method for the synthesis of nanocrystalline iron, chromium, and manganese oxides was described by Amanda L. Willis et al. [49]. This method employed the reactions of metal acetylacetonate precursors and oxygen containing solvents in a reaction to prepare metal oxide nanoparticles. A convenient reaction for the reparation of γ-Fe_2O_3 was discovered and had been expanded to the preparation of γ-Fe_2O_3, Mn_2O_3, Mn_3O_4, and Cr_2O_3. Characterization of these nanocrystalline materials was carried out employing transmission electron microscopy (TEM), high resolution TEM (HRTEM), X-ray diffraction (XRD) and elemental analysis.

Weixin Zhang et al. [50] prepared Mn_3O_4 nanoparticles and MnOOH nanorods through successfully controlling a solvothermal reaction. An aqueous ethanol solution was used as the solvent and they found that the ethanol volume percentage in the solvent and reaction temperature had important effect on the composition of the final products. Experiments showed that single phase of Mn_3O_4 nanoparticles can be prepared at higher reaction temperature and higher volume percent of ethanol, while single phase of MnOOH nanorods as single crystallites can be obtained at lower reaction temperature and lower volume percent ethanol.

Z. W. Chen et al. [51] reported a simple and effective method for the generation of bulk quantity nanorods of manganese oxide, Mn_3O_4 under surroundings of a suitable surfactant and alkaline solution. It was found that the Mn_3O_4 nanorod is smooth, straight and that the geometrical shape is structurally perfect, which is produced with lengths from several hundred nanometers to a few micrometers, and diameters range from 10 nm to 30 nm. The dripping speed of the NaOH solution was found to play an important role in formation of bulk-quantity Mn_3O_4 nanorods. The difference of dripping speed of the NaOH solution leaded to a large difference of Mn_3O_4 morphologies, which was observed in the transmission electron microscopy images.

J. Pike et al. [52] reported Mn_3O_4 nanoparticles with a faceted structure by mixing aqueous solutions of manganese nitrate and hexamethylenetetramine from 20 to 80°C. Activation energy for the particle formation increases from 0.5 to 0.8 kJ/mol with various nitrate concentrations. They described synchroton in-situ time resolved XRD experiments in which Mn_3O_4 nanoparticles were reduced to MnO and subsequently reoxidized in ramping temperature conditions.

Nana Zhao et al. [53] reported a two-phase route to shape- and size- controlled Mn_3O_4 nanocrystals that are capped with organic ligands and dissolved in a nonpolar solvent with excellent stability (at least a few months). They found that using controlled variations in the reaction conditions, the nanocrystals could be grown into either relatively monodisperse spherical shapes or almost perfect cubes.

C. B. Azzoni et al. [54] prepared Mn_5O_8 nanoparticles by prolonged thermal treatment of Mn_3O_4 in air at 723 K. They observed that Mn_5O_8 phase is stable up to 820 and transforms to Mn_3O_4 at about 1000 K.

In this study, attempt will be made to prepare manganese oxides nanoparticles and investigate the structural transformation occurs after calcining the manganese oxide precursor. The manganese oxide precursor will be formed through a gel formation method with the reaction of $KMnO_4$ and glycerol. This method differs from the traditional sol – gel technique in that no expensive alkoxides are used. Another distinct advantage of this method is that it avoids the aggregation of particles and it needs only very simple equipment and the process is very facile and it is a green process because no organic agent except the biodegradable glycerol is used.

Industrial dyestuffs constitute one of the largest groups of organic compounds that cause increasing environmental concerns and their degradation has, therefore, attracted much attention [55 - 57]. Although traditional physical techniques, such as adsorption on activated carbon and coagulation by chemical agents are generally efficient, they simply transfer organic compounds from water to another phase, and

thus cause secondary pollution. The stability of modern dyes has made ineffective their biological decoloration and degradation. Advanced oxidation processes (AOPs) have emerged during the last decades as a viable strategy to degrade dyes in aqueous media [58]. AOPs were based on the generation of very reactive species, such as hydroxyl radicals (OH) that oxidize a broad range of pollutants quickly and nonselectively.

Methylene Blue (MB) is a prototype of dyestuffs, which is particularly resistant to biodegradation [59]. Although there have been numerous reports of photocatalytic MB degradation over the TiO_2 based photocatalyst, most of the studies were performed under UV light irradiation [60]. Recently Zhoa et al [61] reported that some dyes could be degraded under visible light irradiation on TiO_2 by self photosensitized process, but MB is excluded. Up to now, only a few studies have been reported on MB dye degradation under visible light irradiation [62]. Furthermore the catalytic efficiency is limited by the light absorption characteristics of the TiO_2 based photocatalyst. In this research work, the obtained nanoparticles are planned to be investigated for their catalytic activities in the oxidation of an organic dye named MB.

Mn-oxides occur in numerous phases of extremely variable structures [63] that are enabled by the ability of their building units. The huge flexibilities of the units allow modifying the structures and properties through the engineering of the interlayer by a proper choice of preparative method [64]. Among the different methods hydrothermal [65], electrochemical route [66], template synthesis [67] and sol-gel process [68] are notable. Owing to the superiority of sol-gel, alternative methods other than using the expensive alkoxides are also proposed [69]. Despite the different reports of Mn-oxides *nps* synthesis and their characterization, to the best of our knowledge a systematic study on the relationship between crystal geometry and properties especially the oxidative properties has never been conducted. Consequently, in the present work attempt would be made to prepare *nps* of Mn-oxides through an

inexpensive sol-gel method without using expensive alkoxides and a systematic study of their structure and oxidative properties.

References

[1]. H. Cheng, J. Ma, Z. Zhao, L. Qi, *Chem. Mater., 7* (1995) 663.

[2]. S. Ge, X. Shi, K. Sun, C. Li, C. Uher, J. R. Baker, J. M. M. B. Holl, B. G. Orr, *J. Phys. Chem., C* 113 (2009) 13593.

[3]. Y. Kitamura, N. Okinaka, T. Shibayama, O. O. P. Mahaney, D. Kusano, B. Ohtani, T. Akiyama, *Powder Technology*, 176 (2007) 93.

[4]. A. C. Jones, P. R. Chalker, *J. Phys. D: Appl. Phys,* 36 (2003) R80.

[5]. W. Wang, I. W. Lenggoro, Y. Terashi, T. O. Kim, K. Okuyama, *Mat. Sci. Eng. B*, 123 (2005) 194.

[6]. S. Watson, D. Beydoun, J. Scott, R. Amal, *J. Nanopart. Res.*, 6 (2004) 193.

[7]. K. Nagaveni, M. S. Hedge, N. Ravishankar, G. N. Subbanna, G. Madras, *Langmuir*, 20 (2004) 2900.

[8]. K. Nagaveni, G. Sivalingam, M. S. Hegde, G. Madras, *Appl. Catal. B*, 48 (2004) 83.

[9]. O. Carp, C. L. Huisman, A. Reller, *Progress in Solid State Chem.*, 32 (2004) 33.

[10]. X. Chen, S. S. Mao, *Chem. Rev.*, 107 (2007) 2891.

[11]. J. Yang, S. Mei, J. M. F. Ferreira, *Mater. Sci. Eng.*, C 15 (2001) 183.

[12]. W. An, E. Thimsen, P. Biswas, *J. Phys. Chem. Lett.,* 1 (2010) 249.

[13]. K. L. Choy, *Prog. Mater. Sci.*, 48 (2003) 57.

[14]. O. Azzaroni, M. Fonticelli, P. L. Schilardi, G. Benitez, I. Caretti, J. M. Albella, R. Gago, L. Vazquez, R.C. Salvarezza, *Nanotechnology*, 15 (2004) S197.

[15]. K. J. Rao, B. Vaidhyanathan, M. Ganguli, P. A. Ramakrishnan, *Chem. Mater.*, 11 (1999) 882.

[16]. M. H. Bhat, B. P. Chakravarthy, P. A. Ramakrishnan, A. Levasseur, K. J. Rao, *Bull. Mater. Sci.,* 23 (2000) 461.

[17]. V. Subramanian, C. L. Chen, H. S. Chou, G. T. K. Fey, *J. Mater. Chem.*, 11 (2001) 3348.

[18]. C. J. Brinker, S. W. Scherer, Sol–Gel science: the physics and chemistry of sol–gel processing. *Academic Press, New York,* 1990.

[19]. C. J. Brinker, B. C. Bunker, D. R. Tallant, K. J. Ward, R. J. Kirkpatrick, Structure of Sol-Gel Derived Inorganic Polymers: Silicates and Borates, *ACS Symposium series,* Chapter 26, Vol. 360 (1988) 314.

[20]. R.W. Jones, Fundamental Principles of Sol-Gel Technology, Institute of metals, London (1989).

[21]. Z. Pu, M. Cao, J. Yang, K. Huang and C. Hu, *Nanotechnology,* 17 (2006) 799.

[22]. H. Dietz, S. M. Douglas, W. M. Folding, *Science*, 325 (2009) 724.

[23]. S. M. Douglas, H. Dietz, T. Liedl, *Nature,* 459 (2009) 414.

[24]. K. K. Turekian, K. L. Wedepohl, *Geol. Soc. Am. Bull.,* 72 (1961)175.

[25]. B. Mokhlesi, J. B. Leikin, P. Murray, T. C. Corbridge, *Chest* 123 (2003) 897.

[26]. J. W. Harvey, A. S. Keitt, Br. J. Haematol, 54 (1983) 29.

[27]. H. M. Kim, S. J. Kim, S. M. Oh, *Chem. Mater.,* 11 (1999) 557.

[28]. S. K. Nayak, P. Jena, *J. Am. Chem. Soc.,* 121 (1999) 644

[29]. J. Li, W. J. Wang, B. S. Zou, X. C. Wu, J. G. Lin, L. Guo, Q. S. Li, *Appl. Phy. Lett.,* 70 (1997) 3047.

[30]. J. C. Nardi, *J. Electrochem. Soc.,* 132 (1985) 1787.

[31]. J. Cao, Q. H. Mao, L. Shi, and Y. T. Qian, *J. Mater. Chem.,* 21 (2011) 16210.

[32]. D. Yan, S. Cheng, R. F. Zhuo, *Nanotechnology,* vol. 20 (2009) 10.

[33]. Y. W. Tan, L. R. Meng, Q. Peng, and Y. D. Li, *Chemical Communications,* 47 (2011) 1172.

[34]. X. Zhang, Z. Xing, Y. Yu, *Cryst. Eng. Comm. ,* 14 (2012), 1485.

[35]. R. Ma, Y. Bando, L. Zhang, and T. Sasaki, *Advanced Materials,* 16 (2004) 918.

[36]. F. Y. Cheng, J. Z. Zhao, W. Song, *Inorganic Chemistry,* 45 (2006) 2038.

[37]. F. Y. Cheng, J. A. Shen, B. Peng, Y. D. Pan, Z. L. Tao, and J. Chen, *Nature Chemistry,* 3 (2011) 79.

[38]. B. Sun, Z. X. Chen, H. S. Kim, H. Ahn, G. X. Wang, *J. Power Sources,* 196 (2011) 3346.

[39]. H. Ying – Ying, W. Zhoa – Yin, J. Jan, *J. Inorg. Mater.,* 28 (2013) 1045.

[40]. M. Ristic, S. Music, S. Popovic, D. Dragcevic, M. Marcius, M. Ivanda, *J. Mol. Structure,* 1044 (2013) 255.

[41]. E. Karaoglue, H. Deligoz, H. Sozeri, A. Baykal, M. S. Toprak, *Nano – Micro Lett.,* 3 (2011) 25.

[42]. S. Rui, W. Hong – Jan, F. Shou – Hua, *Chem. Res. Chinese Universities*, 28 (2012) 577.

[43]. S. Xing, Z. Zhou, Z. Ma, Y. Wu, *Materials Letters,* 65 (2011) 517.

[44]. T. Ahmed, K. V. Tamanujachary, S. E. Lofland, A. K. Ganguli, *J. Mater. Chem.,* 14 (2004) 3406.

[45]. Jin Mu, Zhenfang Gu, Hua Sun, Qinglian Wei, *Journal of Dispersion Science and Technology,* 27 (2006) 307.

[46]. Ning Wang, Lin Guo, Lin He, Xia Cao, Chinping Chen, Rongming Wang, Shihe Yang, *Small*, 3 (2007) 606.

[47]. M. Ocana, *Colloid Polym. Sci.*, 278 (2000) 443.

[48]. W. S. Seo, H. H. Jo, K. Lee, B. Kim, S. J. Oh, J. T. Park, *Angew. Chem. Int.*, 43 (2004) 1115.

[49]. A. L. Willis, Z. Chen, J. He, Y. Zhu, N. J. Turro, S. O. Brien, *Journal of Nanomaterials*, (2007) 7

[50]. W. Zhang, Z. Yang, Y. Liu, S. Tang, X, Han, M. Chen, *J. Crystal Growth*, 263 (2004) 394.

[51]. Z. W. Chen, J. K. L. Lai, C. H. Shek, *App. Phys. Lett,* 86 (2005) 181911.

[52]. J. Pike, J. Hanson, L. Zhang, S. W. Chan, *Chem. Mater.*, 19 (2007) 5609.

[53]. N. Zhao, W. Nie, X. Liu, S. Yian, Y. Zhang, X. Ji, *Small*, 4 (2008) 5609.

[54]. C. B. Azzoini, M. C. Mozzati, P. Galinetto, P. Aleari, V. Massarotti, D. Capsoni, M. Bini, Solid State Communications, 112 (1999) 375

[55]. R. Ashai, T. Morikawa, T. Ohwaki, K. Aoki, Y. Taga, *Science*, 293 (2001) 2 69.

[56]. I. K. Konstantinou, T. A. Albanis, *Appl. Catal. B,* 49 (2004) 1

[57]. J. W. Tang, Z. G. Zou, J. H. Ye, *Chem. Mater.,* 16 (2004) 1644.

[58]. S. F. Yin, B. Q. Xu, C. F. Ng, C. T. Au, *App. Catal. B* 48 (2004) 237.

[59]. T. Y. Zhang, T. Oyama, A. Aoshima, H. Hidaka, J. C. Zhao, N. Serpone, *J. Photochem. Photobiol. A* 140 (2001) 163.

[60]. A. Houas, H. Lachheb, M. Ksibi, E. Elaloui, C. Guillard, J. M. Herrmann, *Appl. Catal. B* 31 (2001) 145.

[61]. W. Zhao, C. Chen, X. Li, J. Zhao, H. Hidaka, N. Serpone, *J. Phys. Chem. B*, 1 06 (2002) 5022.

[62]. X. Z. Li, F. B. Li, *Environ. Sci. Technol.,* 35 (2001) 2381.

[63]. Q. Feng, H. Kenoh and K. Ooi, *J. Mater. Chem.* 9 (1999) 319.

[64] S. M. Auerbach , K. A. Carrado, P. K. Dutta, "Handbook of Layered Materials; Marcel Dekker, Inc., New York, Chapter 9, pp 475, 2004.

[65]. G. H. Du, Q. Chen, R. C. Che, *Applied Physics Letters*, 79 (2001), 3702.

[66]. C.-C. Hu, C.-C. Wang, *J. Electrochem. Soc.,* 150 (2003) 1079.

[67]. S. Mann, *Angewandte Chemie International Edition*, 39 (2000) 3392.

[68]. S. Franger, S. Bach, J. Farcy, *J. Power Sour.*, 109 (2002) 262.

[69]. S. Ching, S. L. Suib, *Comments on Inorganic Chemistry,* 19 (1997) 263

CHAPTER 3

CHARACTERIZATION TECHNIQUES

3.1 X-ray diffraction

The German Physicist Wilhelm Roentgen discovered X-rays in 1885. X-rays are electromagnetic waves of short wavelengths in the range of 10^{-2} to 10^{2} Å. Unlike ordinary light, these rays are invisible, but they travel in straight lines and affect photographic film in the same way as light. On the other hand, they were much more penetrating than light and could easily pass through the human body, wood, quite thick pieces of metal and other "opaque" objects.

3.1.1 Electromagnetic radiation

X-rays are electromagnetic radiation of exactly the same nature as light but of very much shorter wavelength. The unit of measurement of wavelength in the X-ray region is the Angstrom (Å), equal to 10^{-10} m and X-ray used in diffraction have wavelengths lying approximately in the range 0.5 to 2.5 Å, whereas the wavelength of visible light is of the order of 6000 Å.

X-ray therefore occupies the region between gamma and ultraviolet rays in the complete electromagnetic spectrum as shown in Fig.3.1.
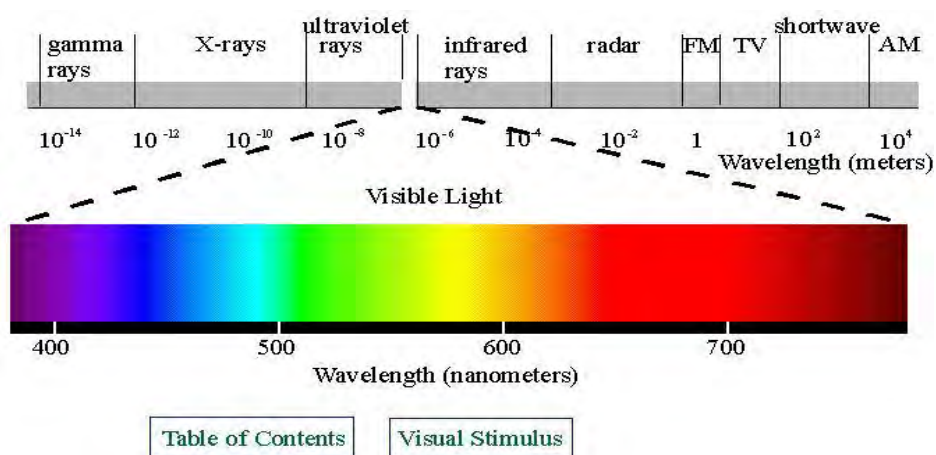
Fig.3.1: Electromagnetic spectrum

The approved SI unit for wavelength in the X-ray region is nanometer:

1 nanometer = 10^{-9} m = 10 Å.

3.1.2 Production of X-ray

We have seen that X-rays are produced whenever high-speed electrons collide with a metal target. Any X-ray tube must therefore contain (i) a source of electrons, (ii) a high accelerating voltage and (iii) a metal target. Furthermore since most of the kinetic energy of the electron is converted into heat, the latter is almost always water-cooled to prevent its melting.

All X-ray tubes contain two electrodes, an anode (the metal target) maintained, few exceptions, at ground potential, on a cathode maintained at a high negative potential, normally of the order of 30000 to 50000 volt for diffraction work. X-ray tubes may be divided into two basic types, according to the way in which sections are produced by the ionization of small quantity of gas (residual) air in a partly evacuated tube and filament tubes, in which the source of the electrons is a hot filament.

3.1.3 X-ray diffractometer

Thin sheets of the samples were prepared from the alloy ingot by rolling the ingot. Sharp strip like samples were cut from the thin sheet for Debye-Scherrer experiment. After heat treatment of the samples separately to remove strain the lattice parameter of the quenched specimen in the disordered state were measured by Debye-Scherrer method using Cu radiation. In the present case, a special technique was used to determine the lattice parameter using Debye-Scherrer method. The shape of the sample was used as the same of Debye-Scherrer method sample. But in the conventional Debye-Scherrer experiment, sharp strip sample rotates and X-ray tube and camera remain fixed. In the present case, sample was kept fixed and X-ray tube and detector were moved to the θ and 2θ ranges respectively. Instead of the film, digital data was recovered for the whole 2θ range.

After the pattern is obtained the value of 2θ is calculated for each diffraction line; set of 2θ values is the raw data for the determination of the lattice parameters of the unit cell. Fig.3.2 shows the block diagram of Phillips PW3040 X' Pert PRO X-ray diffractometer.
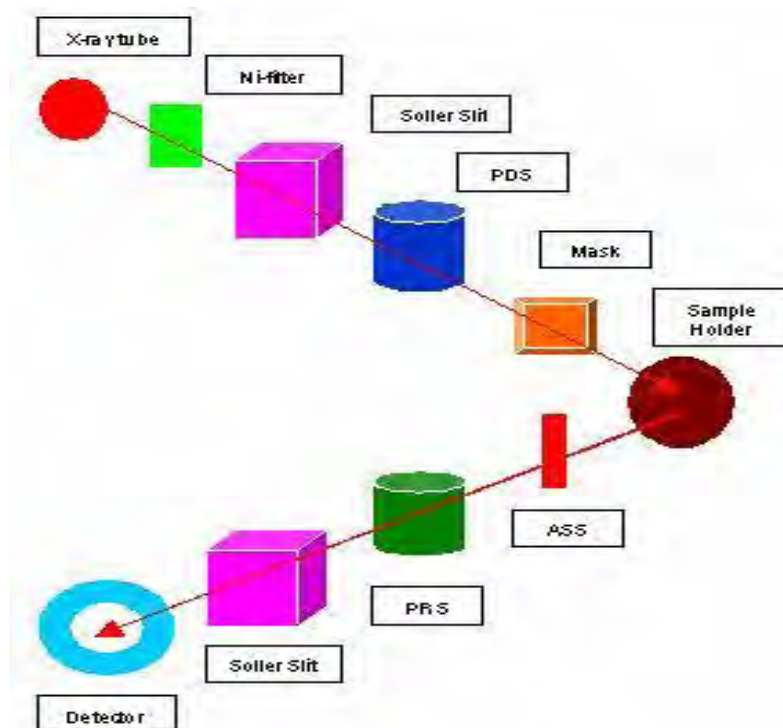
Fig.3.2: Block diagram of the PHILIPS PW 3040 X'Pert PRO XRD system

A PHILIPS PW 3040 X'Pert PRO X-ray diffractometer was used for the lattice parameter determination in the Materials Science Division, Atomic Energy Center, Dhaka. Fig. 3.3 shows the inside view of the X'Pert PRO XRD system.
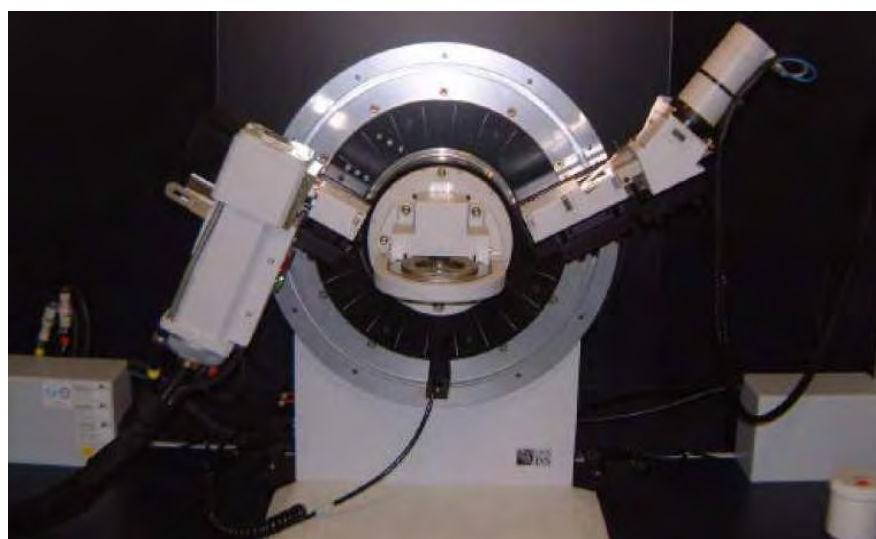
Fig. 3.3: A PHILIPS PW3040 X'Pert PRO X-ray diffractometer

The X'Pert PRO XRD system contains the following parts:

(i). "Cu-Tube" with maximum, input power of 60 kV and 55 mA

(ii). "Ni-Filter" to remove the CuK_α component.

(iii). "Programmable Divergent Slit" (PDS) to reduce divergence of beam and control irradiated beam area.

(iv). "Mask" to get desired beam area.

(v). "Sample holder" for powder sample.

(vi). "Anti Scatter Slit" (ASS) to reduce air scattering background.

(vii). "Programmable Receiving slit "(PRS) to control the diffracted beam intensity.

(viii). "Soller Slit" to stop scattered beam and pass parallel diffracted beam.

X-ray diffractometer was used to study the crystalline phases of the prepared samples. The powder diffraction technique was used with a primary beam power of 40 kV and 30 mA for Cu radiation. A nickel filter was used to reduce CuK_β radiation and finally Cu-K_α radiation was only used as the primary beam. A 2θ scan was taken from 10° to 70° to get possible fundamental peaks with the sampling pitch of 0.02° and time for each step data collection was 1.0 sec. After that data of the samples were analyzed by computer software. A schematic diagram of X-ray is shown in Fig. 3.4.
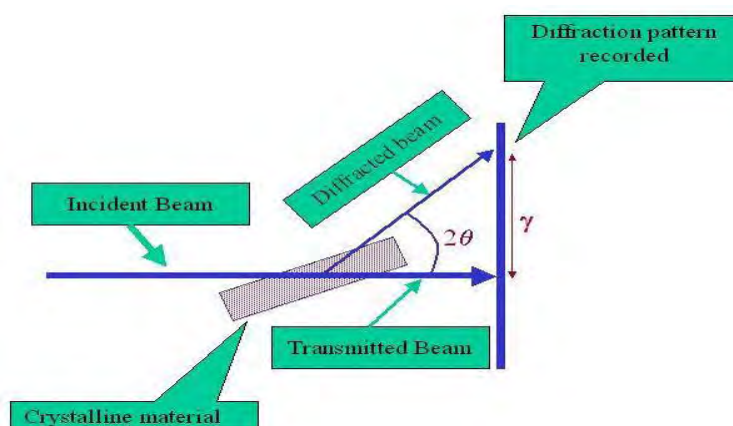
Fig. 3.4: Schematic diagram of X-ray

The aim of the present study was to determine the grain size of manganese oxides nanoparticles. The grain size of the prepared samples were determined from the strongest peak of each XRD patterns using Scherrer's formula,

$$D_g = \frac{0.9\lambda}{\beta \cos\theta} \dots \dots \dots \dots \dots (3.1)$$

Where D_g is the average grain size, λ is the wavelength of the radiation used as the primary beam of Cu-K_α ($\lambda = 1.54178$ Å), θ is the angle of incident in degree and β is the full width at half maximum (FWHM) of the strongest reflection in radian which was determined experimentally after correction of instrumental broadening (in the present case it is 0.07^o)

The peaks in an X-ray diffraction pattern are directly related to the atomic distance. Let us consider an incident X-ray beam interacting with the atoms arranged in a periodic manner as shown in Fig. 3.5. The atoms represented as block spheres in the figure, can be viewed as forming different sets if planes in the crystal.
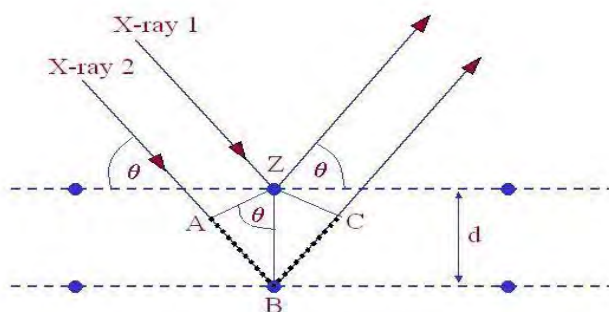
Fig.3.5: Bragg's diffraction pattern

For a given set of lattice plane with an inter planner distance of d, the condition for a diffraction to occur can simply written as

$$2d_{hkl}\sin\theta = n\lambda \dots \dots \dots \dots \dots (3.2)$$

which is known as Bragg's law. Where, λ is the wavelength of the X-ray, θ is the scattering angle and n is an integer representing the order of the diffraction.

3.1.4 Determination of nanometric grain Size by X-ray diffraction

Nanocrystalline alloys are above all crystalline and because of their crystallinity exhibit Bragg scattering peaks in X-ray diffraction experiments. However, due to their small size, significant fine particle broadening is observed in the Bragg peaks. The condition for constructive interference, reinforcement of X-ray scattering from a crystalline solid is given by Bragg's law:

$$n\lambda = 2d\ sin\theta\ ...\quad ...\quad ...\quad ...\quad ...(3.3)$$

This equates the path difference of X-rays scattered from parallel crystalline planes spaced $d = d_{hkl}$ apart to an integral (n) number of X-ray wavelengths λ. Here θ is the X-ray angle of incidence (and of diffraction) measured with respect to the crystalline planes. For an infinite crystal Bragg scattering occurs at discrete values of 2θ satisfying the Bragg condition, i.e., Bragg peaks are δ-functions. For finite sized crystals the peaks are broadened over a range of angles as shown in Fig. 3.6.
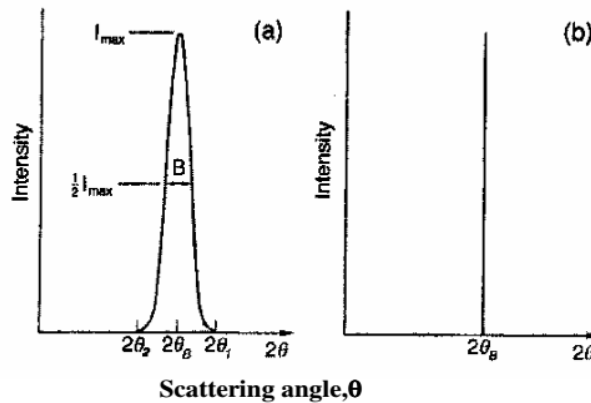
Fig.3.6: Effect of fine particle size on diffraction curves (schematic)

To better understand the phenomenon of fine particle broadening following argument of Cullity, [1] we consider a finite crystal of thickness, $D = md$, where m is an integer, and d is the distance between crystalline planes, i.e., there are m planes in D. Now if the broadened Brag peak begins at an angle $2\theta_2$ and ends at $2\theta_1$, the breadth of

the peak or full width at half maximum is given as:

$$\beta = \frac{1}{2}(2\theta_1 - 2\theta_2) = \theta_1 - \theta_2 \dots \quad \dots \quad \dots \quad \dots \quad \dots (3.4)$$

Now consider the path differences for each of the two angles θ_1 and θ_2, for X-rays traveling the full thickness of the crystal. The width β is usually measured in radians.

We now write path difference equations for these two angles, related to the entire thickness of the crystal rather to the distance between adjacent planes.

$$2D\, sin\theta_1 = (m+1)\lambda \dots \quad \dots \quad \dots \quad \dots \quad \dots (3.5)$$

$$2D\, sin\theta_2 = (m-1)\lambda \dots \quad \dots \quad \dots \quad \dots \quad \dots (3.6)$$

By subtracting we find,

$$D\,(sin\theta_1 - sin\theta_2) = \lambda \dots \quad \dots \quad \dots \quad \dots \quad \dots (3.7)$$

$$D\, 2cos\left(\frac{\theta_1 + \theta_2}{2}\right) sin\left(\frac{\theta_1 - \theta_2}{2}\right) = \lambda \dots \quad \dots \quad \dots \quad \dots (3.8)$$

But θ_1 and θ_2 are both very nearly equal to θ, so that $\theta_1 + \theta_2 \approx 2\theta$ and $sin\left(\frac{\theta_1 - \theta_2}{2}\right) \approx \left(\frac{\theta_1 - \theta_2}{2}\right)$ so that the equation (3.8) can be written as

$$2Dcos\theta\left(\frac{\theta_1 - \theta_2}{2}\right) = \lambda \dots \quad \dots \quad \dots \quad \dots (3.9)$$

From equation (3.4) and (3.9) we can write

$$\beta D\, cos\theta = \lambda \dots \quad \dots \quad \dots \quad \dots (3.10)$$

$$D = \frac{\lambda}{\beta\, cos\theta} \dots \quad \dots \quad \dots \quad \dots (3.11)$$

A more exact empirical treatment yields:

$$D = \frac{0.9\lambda}{\beta \, co\theta} \dots \quad \dots \quad \dots \quad \dots \quad \dots (3.12)$$

which is known as the Scherrer's formula. It is used to estimate the particle size of very small crystals from the measured width of their diffraction curves.

3.1.5 Determination of nanometric lattice parameters by X-ray diffraction

A crystal consists of a periodic arrangement of the unit cell into a lattice. The unit cell can contain a single atom or atoms in a fixed arrangement. Crystals consist of planes of atoms that are spaced a distance d apart, but can be resolved into many atomic planes, each with a different d-spacing. Fig.3.7 represents the view of a crystal lattice.
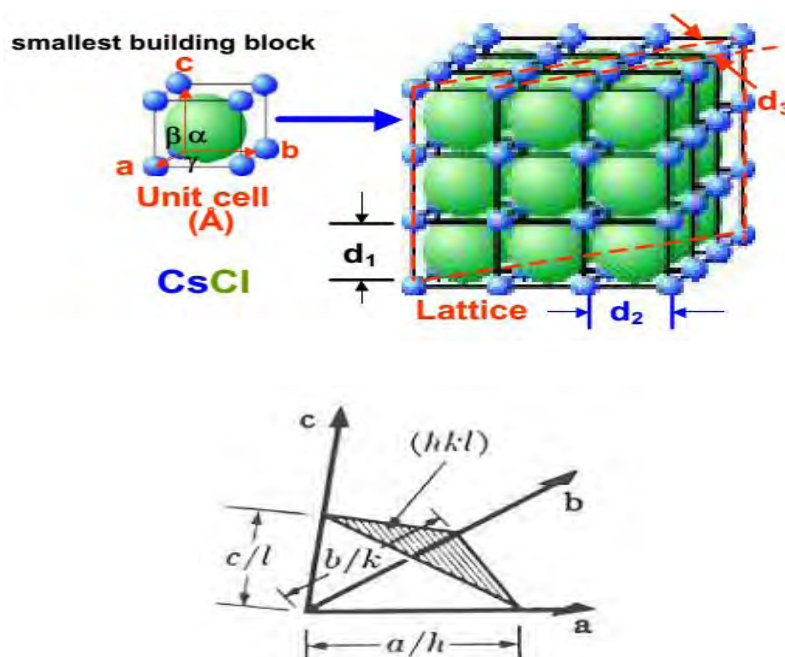
Fig.3.7: A view of crystal lattice with lattice parameters

In the figure a, b and c (length) and α, β and γ are angles between a, b and c which are lattice constants or parameters and can be determined by XRD.

The distance d, between adjacent planes in the set (hkl) may be found from the following equations where a, b, c, α, β and γ represent the lattice parameters of the unit cell [2].

$Cubic$ $: \dfrac{1}{d^2} = \dfrac{h^2 + k^2 + l^2}{a^2} \dots \dots \dots \dots$ (3.13)

$Monoclinic$ $: \dfrac{1}{d^2} = \dfrac{1}{\sin^2 \beta}\left(\dfrac{h^2}{a^2} + \dfrac{k^2 \sin^2 \beta}{b^2} + \dfrac{l^2}{c^2} - \dfrac{2hl \cos\beta}{ac}\right) \dots \ \dots \ \dots$ (3.14)

$Tetragonal$ $: \dfrac{1}{a^2} = \dfrac{h^2 + k^2}{a^2} + \dfrac{l^2}{c^2} \dots \dots \dots \dots$ (3.15)

The values of the lattice parameters (a, b and c) obtained for each reflected plane are plotted against the function F (θ)

$$where, F(\theta) = \frac{1}{2}\left[\frac{\cos^2 \theta}{\sin^2 \theta} + \frac{\cos^2 \theta}{\theta}\right]^{\frac{1}{2}} \ \dots \ \dots \ \dots \ \dots \ \dots (3.16)$$

Here, θ is the Bragg's angle

Straight lines are obtained and the accurate values of lattice parameters (a_o, b_o and c_o) are determined from the extrapolation of these lines to $\theta = 0$ [1]

3.2. Scanning Electron Microscopy (SEM)

Electron microscopes were developed in the 1930s to overcome the limitations of optical microscopy and provide increased magnification and resolution, far superior to optical systems. The first commercialized SEM was built by Cambridge Instruments [3].

SEM is a powerful tool for examining and interpreting microstructures of materials, and is widely used in the field of material science. The principle of SEM is based on the interaction of an incident electron beam and the solid specimen [4]. Electron bombardment can produce a wide variety of emissions from the specimen, including backscattered electrons, secondary electrons, Auger electrons, X-rays, visible photons and so on.

1) **Secondary Electrons:** If an incident electron collides with an electron in a sample atom, it will knock the electron out of its orbital shell and the atom will become ionized. Because the incident electron loses little energy during each collision, multiple collisions are possible, continuing until the incident electron no longer has the energy to dislodge secondary electrons. Each freed secondary electron has a very small kinetic energy (<50 eV), which is independent of the incident electron energy. If generated close enough to the sample surface (<10 nm), these secondary electrons can escape to be collected by the detector. As a direct result, secondary electron imaging is closely related to sample topography.

2) **Backscattered Electrons:** If an incident electron collides with the nucleus of surface atom, the electron will bounce or scatter 'backward' out of the sample as a backscattered electron (BSE). These electrons have high energies, typically between 50 eV and that of the original incident electron. The production of backscattered electrons varies directly with atomic number, and thus backscattered electron images can be used to discern differences in sample atomic number.

3) **Auger Electrons:** As a result of secondary electron generation, a vacancy is left in an ionized atom's electron shell. To fill this vacancy, an electron from a

higher energy outer shell (from the same atom) can drop down to fill the vacancy. This creates an energy surplus in the atom that can be corrected by emitting an outer electron, an Auger electron. Auger electrons have a characteristic energy unique to the element from which they are emitted and can be used to give compositional information about the target sample. Auger electrons have a relatively low kinetic energy and are only emitted from shallow sample depths (<3 nm).

4) Characteristic X-rays: X-rays are also produced by interactions of the incident electron beam with a sample surface. Similar to the Auger electron generating process, the excess energy produced by reshuffling electrons to fill shell vacancies can also be emitted in the form of an X-ray rather than an Auger electron. X-rays have a characteristic energy unique to the element from which they originate and so provide compositional information about a sample.

Secondary electron imaging and X-ray analysis were the primary functions used for SEM sample characterization in this study.

A SEM consists of three distinct parts: an electron column; a detection system; and a viewing system. Fig. 3.8 shows a schematic of a simple scanning electron microscope. Two electron beams are controlled simultaneously by the same scan generator: one is the incident electron beam; the other is for the cathode ray tube (CRT) screen. The incident beam is scanned across the sample, line by line, and the signal from the resulting secondary electrons is collected, detected, amplified and used to control the intensity of the second electron beam. Thus a map of intensity of secondary electron emission from the scanned area of the sample will be shown on the CRT screen as variations in brightness, reflecting the surface morphologies of the specimen. Given this mechanism, the magnification of the SEM image can be adjusted simply by changing the dimensions of the area scanned on the sample surface.
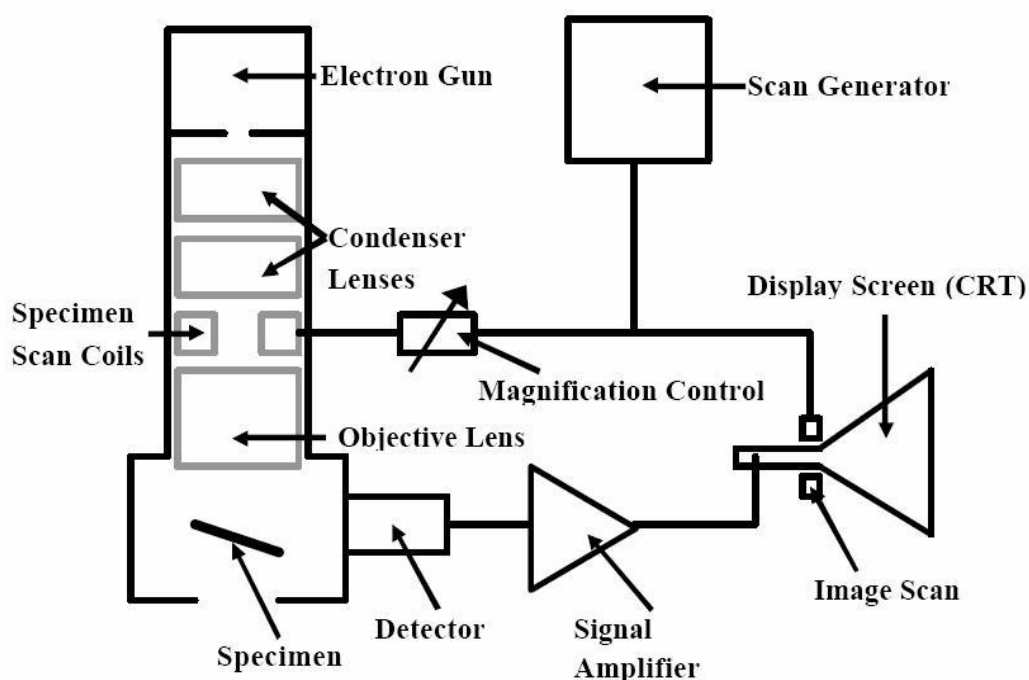
Fig.3.8: Schematic diagram of a scanning electron microscope

The spatial resolution of the SEM is strongly dependent on diameter (spot size) of the electron probe beam at the specimen surface. In a SEM system, the diameter of the incident electron beam is demagnified using two or more electron lenses before it reaches the sample surface. At the same time, the effective diameter of the electron source is a key factor in determining the resolution of the SEM. There are two basic types of electron guns in current use: thermionic electron gun and field emission electron gun. The diameters of the electron beam originating from these gun types are about 20-50 μm and 10 nm, respectively. Thus, field emission SEM (FESEM) is the electron source of choice for high-resolution SEM images.

The SEM systems employed in this work is field emission scanning electron microscopy. Fig.3.9 shows a photo of the JSM-7600F (FE-SEM, Tokyo, Japan) system using in the Department of Glass and Ceramic Engineering, Bangladesh University of Engineering and Technology (BUET).

Fig.3.9: A photo of SEM JSM-7600F

3.3 Energy Dispersive X-ray Spectroscopy (EDX)

Energy dispersive X-ray spectroscopy (EDX or EDS) is an analytical tool predominantly used for chemical characterization. Being a type of spectroscopy, it relies on the investigation of a sample through interactions between light and matter, analyzing X-rays in this particular case. High energy electron beams (in an SEM or TEM) strike the material to be analyzed, and X-rays are emitted. These X-rays can be detected by a Si Li detector, calibrated with respect to cobalt metal emission (6.925 keV), and then used to identify and analyze the elemental composition of the specimen surface. Its characterization capabilities are due in large part to the fundamental principle that each element of the Periodic Table has a unique electronic structure and, thus, a unique response to electromagnetic waves [5].

Essentially, an X-ray photon hits a diode in the detector producing a charge that is converted into a positive voltage pulse via a field effect transistor (FET). The pulse is subsequently converted by an analogue to digital converter, into a numerical value relative to the X-ray's incoming energy. The signal is then assigned to a particular energy channel and registered as a single count. Counts are compiled to produce an energy dispersive spectrum. The various emission lines associated with X-rays emitted from an atom are named after the shell of the initial vacancy, i.e. K, L, M, etc. A Greek letter subscript is used to indicate the shell of the electron that fills the gap.

For example, K_α radiation refers to radiation resulting from a vacancy in the K shell being filled by an electron from the next highest shell. K_β denotes a K-shell vacancy filled by an electron from two shells above. There are some basic rules that apply for the order and energy of the X-rays:

1. For a given element, the lower line series has a higher energy, i.e. the energies of the K lines are greater than those of the L lines.

2. Within a line series, the higher atomic number elements emit higher energy X-rays. i.e., the oxygen K lines are higher in energy than carbon K lines.

3. The lower line series have simpler structures than the high line series, i.e. the K lines are simple, whilst the L and M lines get more complex and overlapping starts to occur.

EDX spectra can be acquired over short time-periods and be displayed almost simultaneously, providing a near instant visual representation of the chemical analysis. Qualitative analysis determines what elements are present in a sample by identification of the peaks in the spectrum, whilst quantitative analysis is used to derive the relative abundance of the elements from their corresponding peak intensities, either compared to other elements present in the spectrum or to standards.

For EDX, as a general rule of thumb, elements of $Z>11$ can be analyzed if they are in a concentration of greater than 5 weight% with an accuracy of around ±3% if there are no significant peak overlaps. The analyst needs to think carefully about the sample (i.e. topography, porosity, etc), the lateral and depth resolution of the X-ray emission in relation to the sample microstructure, and the quoted accuracy of any computer generated results, before regarding EDX as a completely reliable black-box technique.

In this study, EDX analysis was used mainly to determine the bulk composition of the sample materials. In an SEM, a fixed accelerating voltage of 20 kV was used in order to obtain high signal intensity.

3.4 Fourier Transform Infrared spectroscopy (FTIR)

Fourier Transform Infrared spectroscopy (FTIR) is a technique based on the vibrations of the atoms within a molecule. An infrared (IR) spectrum is obtained by passing IR radiation through a sample and determining what fraction of the incident radiation is absorbed at a particular energy. The energy at which any peak in an absorption spectrum appears corresponds to the frequency of a vibration of a part of a sample molecule [6]. Moreover, chemical bonds in different environments will absorb varying intensities and at varying frequencies. Thus IR spectroscopy involves collecting absorption information and analyzing it in the form of a spectrum - the frequencies at which there are absorptions of IR radiation ('peaks' or 'signals') can be correlated directly to bonds within the compound in question. Each inter-atomic bond may vibrate in several different motions (stretching or bending), individual bonds may absorb at more than one IR frequency. Stretching absorptions usually produce stronger peaks than bending, however the weaker bending absorptions can be useful in differentiating similar types of bonds (e.g. aromatic substitution).

The basic components of an FTIR spectrometer are shown schematically in Fig. 3.10. The radiation emerging from the source is passed to the sample through an interferometer before reaching a detector. Upon amplification of the signal, in which high-frequency contributions have been eliminated by a filter, the data are converted to a digital form by an analogue-to-digital converter and then transferred to the computer for Fourier transformation to be carried out [6].
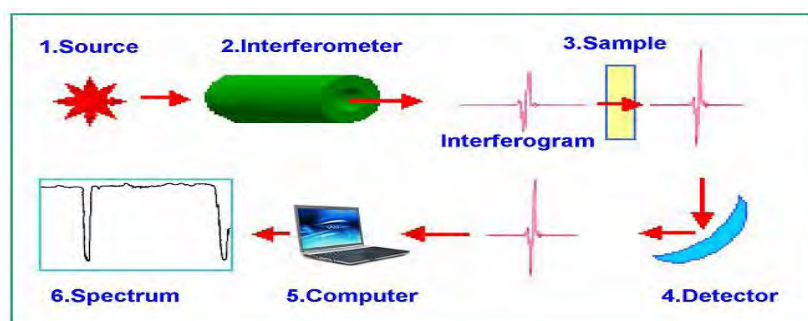

Fig.3.10: Schematic illustration of an FTIR system

One of the great advantages of infrared spectroscopy is that virtually any sample in nearly any state can be studied. Liquids, solutions, pastes, powders, films, fibers, gases and surfaces can all be examined by a judicious choice of sampling technique. An FTIR spectroscopy (JASCO 6300) in the Chemistry Division, Atomic Energy Centre, Dhaka, was carried out to study the potential existence of Mn-Mn, Mn-O, O=O bonds in the Mn-Oxides nanomaterials. The photo image of the instrument is shown in Fig. 3.11.

Fig.3.11: A photo of Jasco-FT/IR-6300 FTIR machine

The FTIR sample handling is to grind finely a quantity of the sample with a specially purified salt (usually potassium bromide) to remove scattering effects from large crystals. This powder mixture is then crushed in a mechanical die press to form a translucent pellet through which the beam of the spectrometer can pass.

3.5 Thermogravimetric Analysis (TGA)

Thermogravimetric analysis (TGA) is a technique in which the mass of the sample is measured against time or temperature while the temperature is changed under a certain atmosphere. This method is used for the determination of sample purity, water content, carbonate or organic content present in it and also for studying decomposition reactions. The graph of the resultant change in mass with respect to temperature is called a thermogravimetric curve [7]. An arbitrary TGA thermogram is displayed in Fig.3.12 showing the change in sample mass with the increase in

temperature. In the figure each slope corresponds to a weight loss produced by the evaporation of one or more compounds of the analyzed mixture.
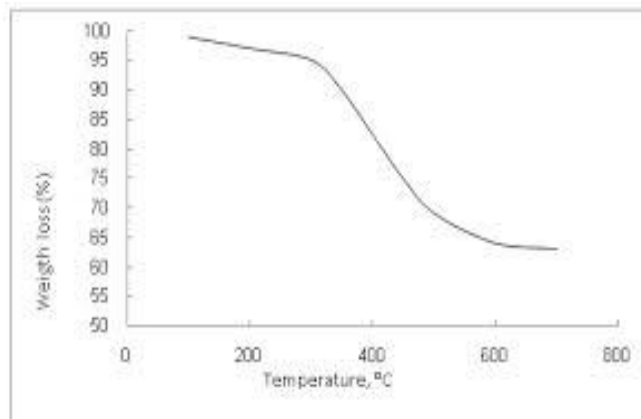

Fig.3.12: Weight loss as a function of temperature

In fact the kinetics i.e. the rate at which the property changes with temperature can also be measured. The instrument or the detector for TGA is a balance, called a thermobalance or thermogravimetric analyzer. The TGA apparatus detects small mass changes of a specimen, kept in thermobalance, which caused with change in temperature of the furnace. The flow of temperature in furnace is under a controlled temperature program. Any change in sample weight can be detected by thermobalance. Sensitivities of the order of 0.1 μg or less are determined. It can be carried out in both inert or air atmosphere. Continuously, mass change with time and temperature is recorded. Some of the major factors affecting TGA measurements include sample size, heating rate, buoyancy, electrostatic effects, gas flow and sample holder. By analyzing the TGA curve, relative mass change with respect to the initial quantity (%) is obtained.

3.6 Differential Scanning Calorimetry (DSC)

Differential Scanning Calorimetry (DSC) is a technique in which the difference in the amount of heat required to increase the temperature of a sample and reference are measured as a function of temperature. In the present study TA instrument, SDT Q-600 was used in the Nuclear and Radiation Chemistry Division, Institute of Nuclear

Science and Technology, Atomic Energy Research Establishment, Savar, Dhaka, which had a temperature scanning range from room temperature to ~900°C. DSC measurement was used to identify the phase transformation of Mn-oxides nanomaterials. The sample was put in a Pt pan and placed on a Pt holder. An empty pan was placed in the other Pt holder for a reference. The sample pans were designed to have a very high thermal conductivity. In the present investigation the amount of each sample was 10 mg. Fig.3.13 shows a schematic diagram of a DSC system.
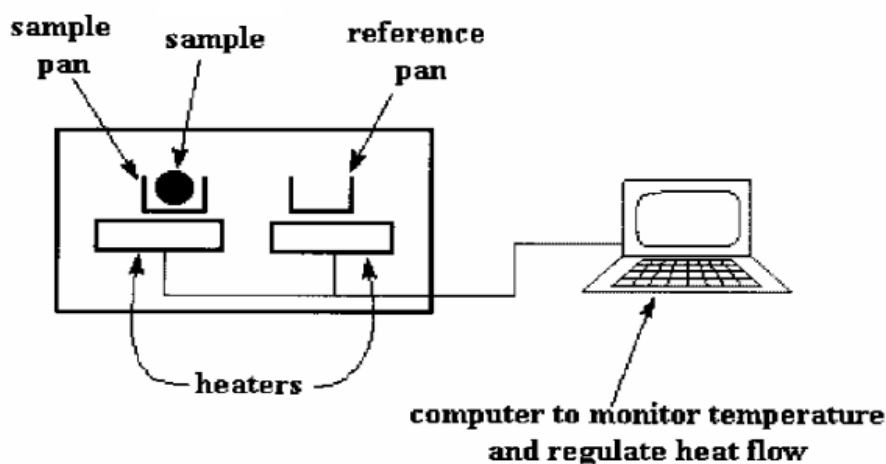
Fig.3.13: Schematic diagram of Differential Scanning Calorimetry (DSC)

The instrument cells are often airtight to shield the sample and reference from external thermal perturbations. This also allows experiments to be performed under variable pressures and atmospheres. The whole system was purged with high purity Ar gas to minimize sample oxidation. The heating rate for non-isothermal scans was 10 K/min. The temperature and enthalpy were calibrated using pure In and Zn standards. In isothermal mode, the temperature of the reference and the sample was raised to the pre-setting temperature and kept isothermally. In our experiment non-isothermal DSC were used to study the phase transformation kinetics. Whether more or less heat must flow to the sample depends on whether the process is exothermic or endothermic. For example, as a solid sample melts to a liquid it will require more heat flowing to the sample to increase its temperature at the same rate as the reference. This is due to the absorption of heat by the sample as it undergoes the endothermic

phase transition from solid to liquid. By observing the difference in heat flow between the sample and reference, differential scanning calorimeters are able to measure the amount of heat absorbed or released during such transitions. DSC may also be used to observe more subtle phase changes. DSC is widely used in industrial settings as a quality control instrument due to its applicability in evaluating sample purity and for studying polymer curing.

A typical differential scanning calorimeter consists of two sealed pans: a sample pan and a reference pan which is generally an empty sample pan. These pans are often covered by or composed of aluminum, which acts as a radiation shield. The two pans are heated, or cooled, uniformly while the heat flow difference between the two is monitored. This can be done at a constant temperature, but is more commonly done by changing the temperature at a constant rate, a mode of operation also called temperature scanning. Fig.3.14 shows a pictorial view of a DSC setup of Thermal Analysis, SDT Q-600.

Fig.3.14: DSC & TGA analyzer (TA instrument, SDT Q-600)

During the determination, the instrument detects differences in the heat flow between the sample and reference. This information is sent to an output device, most often a computer, resulting in a plot of the differential heat flow between the reference and sample cell as a function of temperature. When there are no thermodynamic physical or chemical processes occurring, the heat flow difference between the sample and reference varies only slightly with temperature, and shows up as a flat or very shallow

base line on the plot. However, an exothermic or endothermic process within the sample results in a significant deviation in the difference between the two heat flows. The result is a peak in the DSC curve. Generally, the differential heat flow is calculated by subtracting the sample heat flow from the reference heat flow. When following this convention, exothermic processes will show up as positive peaks above the baseline while peaks resulting from endothermic processes are negative below the baseline.

The result of a DSC experiment is a heating or cooling curve. This curve can be used to calculate enthalpies of transitions. This is done by integrating the peak corresponding to a given transition. It can be shown that the enthalpy of transition can be expressed using the following equation:

$$\Delta H = KA$$

where ΔH is the enthalpy of transition, K is the calorimetric constant, and A is the area under the curve. The calorimetric constant will vary instrument to instrument, and can be determined by analyzing a well-characterized sample with known enthalpies of transition [8]. An arbitrary DSC thermogram is displayed in Fig.3.15 showing various transformations.
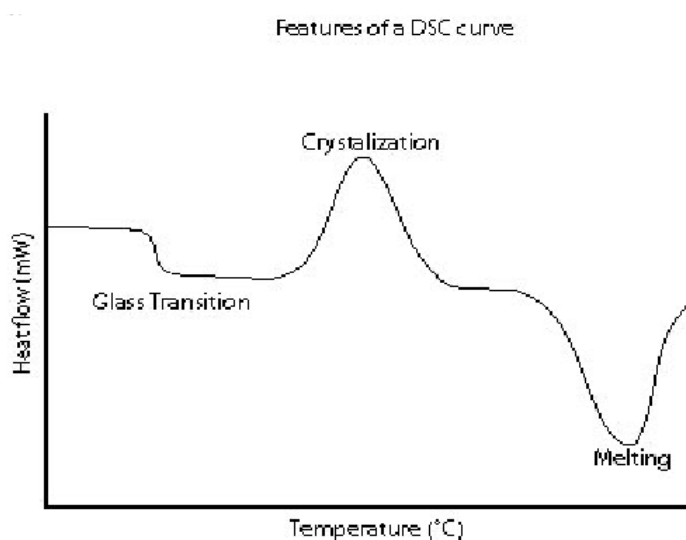
Fig. 3.15: Heat flow as a function of DSC curve

As the temperature increases, an amorphous solid will become less viscous. At some point the molecules may obtain enough freedom of motion to spontaneously arrange themselves into a crystalline form. This is known as the crystallization temperature (T_c). This transition from amorphous solid to crystalline solid is an exothermic process, and results in a peak in the DSC signal. As the temperature increases the sample eventually reaches its melting temperature (T_m). The melting process results in an endothermic peak in the DSC curve. The ability to determine transition temperatures and enthalpies makes DSC an invaluable tool in producing phase diagrams for various chemical systems [8].

3.7 Ultraviolet – visible (UV-Visible) absorption spectroscopy

Ultraviolet-visible spectroscopy (UV-VIS) uses light in the visible and adjacent near ultraviolet (UV) ranges. At these wavelengths, molecules undergo electronic transitions [9]. In this technique, the light passes through the sample to be analyzed, and some of the light is absorbed by the sample. Thus, the sample has to be thin enough such that some of the light is transmitted. Another factor is that the sample must be placed onto a supporting substrate, for example, quartz, that is transparent at the wavelengths of light used.

When visible or ultraviolet light is absorbed by the valence electrons of the material, these electrons are promoted from their ground states to higher energy excited states (Fig.3.16). The energies of the orbitals involved in electronic transitions have fixed values. The difference between the initial and final intensities is recorded. When plotted into a spectrum as wavelength against absorbance, the absorbance is defined by using the Beer-Lambert law:

$$A = -log_{10}\left(\frac{I}{I_0}\right)$$

Where, A is the measured absorbance, I_0 is the intensity of the incident light at a given wavelength, and I is the transmitted intensity, respectively. Most spectrometers display absorbance on the vertical axis, and the commonly observed range is from 0

(100% transmittance) to 2 (1% transmittance). The wavelength of maximum absorbance is a characteristic value, designated as $\lambda_{max.}$
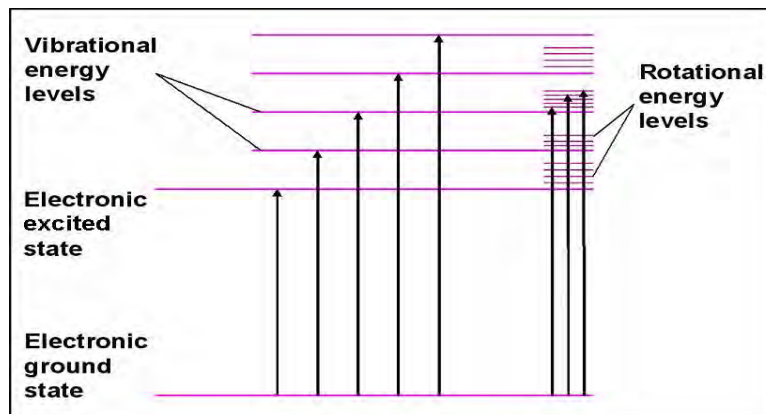
Fig.3.16: Illustration of the electronic transitions process during light absorption

In this study, A UV-visible spectrophotometer (Shimadzu-1800) was used in the Chemistry Division, Atomic Energy Centre Dhaka, to monitor the changes in absorbance of the dye solution a small amount of dye solution suspended with nanomaterials was pipetted into a quartz cuvette. Then the absorbance was recorded before and after the suspension of nanomaterial into the dye solution at different interval of time.

References

[1]. B. D. Cullity, Elements of X-ray diffraction, Addision-Wesley, 1972

[2]. C. Suryanarayana, M. G. Norton, X-ray Diffraction, A Practical Approach, Plenum Press, New York, 1998

[3]. J. I. Goldstein, D. E. Newbury, P. Echlin, Scanning Electron Microscopy and X-ray Microanalysis, 2nd ed., Plenum Press, New York and London, 1992.

[4]. P. J. Grundy, G. A. Jones, Electron microscopy in the study of materials, Edward Arnold Publishers Limited, 1976.

[5]. http://en.wikipedia.org/wiki/Energy-dispersive_X-ray_spectroscopy

[6]. B. Stuart, Modern Infrared Spectroscopy, John Wiley & Sons Ltd, West Sussex, England, 1996

[7]. http://en.wikipedia.org/wiki/UV/VIS_spectroscopy.

[8]. J. A. Dean, The Analytical Chemistry Handbook. New York. McGraw Hill, Inc. 1995

CHAPTER 4
EXPERIMENTAL

4.1 Materials and Instruments

4.1.1 Chemical and reagents

The chemicals and reagents used in this work were analytical grade and used without further purification. De-ionized water was used as solvent to prepare most of the solutions of this work. The chemicals and reagents used in this work are listed below:

(i) Potassium permanganate (Merck, India)

(ii) Glycerol (JHD, China)

(iii) Sulfuric acid (E. Merck, Germany)

(iv) Methylene Blue (E. Merck, Germany)

4.1.2 Instruments

Analysis of the samples was performed using the following instruments:

(i)   X-ray Diffractometer (Philips, Expert Pro, Holland)

(ii)   Fourier Transform Infrared Spectrophotometer (Jasco-FTIR-6300)

(iii)   Field Emission Scanning Electron Microscopy (JSM-7600F, Tokyo, Japan)

(iv)   UV-visible Spectrophotometer (Shimadzu-1800)

(v)   DSC and TGA machine (TA instrument, SDT Q-600)

(vi)   Furnace (Naber Therm, N-7, Germany)

(vii)   pH meter (Hanna, pH 209, India)

(viii) Centrifuge machine (ABT-028C, USA)

(ix)   Digital Balance (AB 265/S/SACT METTLER, Toleto, Switzerland)

4.2 Synthesis of Mn-oxide nanoparticles

Mn-oxide was prepared by a gel formation route based on reduction of $KMnO_4$ with glycerol. The gel precursor was obtained by adding 50 mL 0.4 M glycerol solution into 100 mL 0.3 M $KMnO_4$ solution with the help of a burette under intensive stirring for 60 ± 10 seconds. The gel was formed within few seconds. The solution was set aside to gel undisturbed for 24 hours. The gel was heated on a hot plate at 80^0C

temperature. Then the residue was dispersed in water and excess K^+ was washed with de-ionized water and centrifuged at 3000 rpm for 10 min for several times. The product was dried at 80 °C in an electric oven to get brown powder. The dried product was then stored in a desiccator.

4.3 Spectral analysis

4.3.1 X-ray diffraction

Manganese oxide nanomaterials were analyzed for their X-ray diffraction pattern in the powder state. The powder samples were pressed in a square aluminum sample holder (40mm × 40mm) with a 1 mm deep rectangular hole (20mm x 15mm) and pressed against an optical smooth glass plate. The upper surface of the sample was labeled in the plane with its sample holder. The sample holder was then placed in the diffractometer.

4.3.1.1 Effect of temperature on phase transformation

To investigate the effect of temperature on phase transformation, the nanoparticles were heat treated at 200 °C, 250 °C, 300 °C, 350 °C, 400 °C, 450 °C, 500 °C, 550 °C, 600 °C, 650 °C and 700 °C for three hours in a muffle furnace. The heat treated nanoparticles were analyzed using X-ray diffractometer as the procedure described in section 3.1.3.

4.3.1.2 Phase transformation as a function of time

The phase transformations of Mn-oxide nanoparticles after heat treatment at different temperatures were investigated as a function of time. When the phase transformation was found at a certain temperature then the influence of time was also monitored. The XRD patterns of the nanoparticles were investigated after heat treatment at time interval: 30 minutes, 60 minutes, 90 minutes, 120 minute, 150 minutes and 180 minutes in the temperature at which a new phase was formed.

4.3.2 Energy Dispersive X-ray (EDX) spectra

Elemental analyses of the synthesized different Mn-oxides nanomaterials were performed by EDX spectra. The dried powders of Mn-oxides nanomaterials were placed on a 1 cm × 1cm conducting steel plate. The steel plate was then placed on a conducting carbon glued strip. The sample was then placed in the main FESEM chamber integrated with the EDX instrument.

4.3.3 Infrared spectra

The infrared spectra of the dried samples of different Mn-oxide nanomaterials were recorded on an FTIR spectrometer in the region of 4000 – 400 cm^{-1}. IR spectra of the solid samples were frequently obtained by mixing and grinding a small amount of materials with dry and pure KBr crystals. The mixing and grinding were done in a mortar by a pestle. The powder mixture was then compressed in a metal holder under a pressure of 8–10 tons to make a pellet. The pellet was then placed in the path of IR beam for measurements.

4.3.4 Ultraviolet – visible spectra

The ultraviolet-visible spectral analysis of the sample solutions employed a double beam spectrophotometer. UV-visible spectroscopic analysis for the degradation studies involved aqueous solution. The amount of dye degraded by Mn-oxides nanomaterials was determined spectroscopically.

4.4 Surface morphology

The surface morphology of the different oxides of manganese was adopted using Field Emission Scanning Electron Microscopy. The dried powders of the synthesized Mn-oxide nanomaterials were dispersed on a conducting carbon glued strip. The sample loaded strip was then mounted to a chamber that evacuated to ~ 10^{-3} to 10^{-4} torr and then a very thin gold layer (~few nanometers thick) were sputtered on the sample to ensure the conductivity of the sample surface. The sample was then placed

in the main SEM chamber to view its surface. The system was computer interfaced and thus provides recording of the surface images in the computer file for its use as hard copy.

4.5 Decolorization of dye using Mn-oxides nanoparticles

4.5.1 Decolorization of Methylene Blue (MB)

4.5.1.1 Structural dependence on decolorization of MB

The structural dependence of oxidative property of synthesized Mn-oxides nanoparticles such as is Mn_3O_4, Mn_5O_8 and Mn_2O_3 nanoparticles is demonstrated by their comparative oxidative capacity in the decolorization of dye solution. Methylene Blue (MB) was taken as a model of an organic dye. The performance of Mn-oxides nanoparticles on the decolorization of MB dye was investigated spectroscopically. The UV-vis. spectra of the 10μM MB solution was taken before and after charging Mn_3O_4, Mn_5O_8 and Mn_2O_3 nanoparticles suspensions (1.0 g L^{-1}) in neutral media.

4.5.1.2 Various concentrations of MB studied for decolorization

Stock MB solution was prepared by dissolving 0.036 g solid MB to 500 mL deionized water. In this way, 2×10^{-4} M MB solution was prepared which was used as stock MB solution. 1×10^{-5} M, 2×10^{-5} M and 3×10^{-5} M MB solutions were prepared by diluting 5 mL, 10 mL and 15 mL of stock solution respectively to 100 mL with deionized water. 1 mL sulfuric acid and 5 mL Mn-oxide nanoparticle suspensions (250 mg L^{-1}) were added to 5 mL of each of these MB concentrations. After 1 min, absorbance of each of the reaction mixtures was taken.

4.5.1.3 Influence of amount of Mn-oxide nanoparticles on MB decolorization

To investigate the effect of amount of Mn-oxide nanoparticles on MB decolorization, 3×10^{-5} M MB solution was prepared by diluting 15 mL of stock solution to 100 mL with deionized water. To 5 mL of this MB and 1 mL H_2SO_4 different amount of Mn-oxide nanoparticles suspensions, 1 mL, 3 mL, 5 mL and 7 mL were added and

allowed to react for 1 min. UV-vis absorption spectra of MB solutions were measured in every case.

4.5.1.4 Effect of pH on MB decolorization

Effect of pH on MB decolorization was studied at low pH *i.e.*, 3 and 5 keeping the amount of nanoparticles and concentration of MB fixed. The pH of the solution was controlled by adding H_2SO_4 into the solution. 3 mL of nanoparticles suspension was added to 5mL of 3×10^{-5} M MB solution at pH 3 and 5. After 1 min UV-visible absorption spectrum was taken for each solution and absorbance was recorded.

4.5.1.5 MB decolorization as a function of time

The performance of Mn-oxide nanoparticles on the degradation of MB dye was monitored as a function of time. The reaction was carried out in a 250 mL beaker which contains 50 mL 3×10^{-5} M MB solution and 50 mL nanoparticle suspension at pH 3 and 5. The mixture was allowed to react at room temperature. For optical absorption measurements approximately 1 mL of the mixture was taken out into the UV quartz cell for a given time interval: 1 min, 2 min, 3 min, 5 min, 7 min, 10 min, 20 min, 30 min, 1 hr and 24 hrs.

4.5.2 Structural change of Mn-oxides due to decolorization of MB

The structural change of Mn-oxides nanoparticles due to decolorization of MB was investigated by XRD analyses. 200 mL of 3×10^{-5} M MB solution was taken in a beaker. Then Mn-oxides nanoparticles suspension (250 mg L^{-1}) was added to the MB solution at pH 3. After 24 h, Mn-oxides nanoparticles were separated from the mixtures and washed repeatedly with deionized water. Then the washed Mn-oxide nanoparticles were dried at 80 °C and XRD analyses were carried out for structural characterization.

CHAPTER 5

RESULTS

AND

DISCUSSION

5.1 Structural Characterization

5.1.1 X-ray diffraction analysis

5.1.1.1 Phase identification

The X-ray Diffraction (XRD) patterns of the samples are obtained as a function of Bragg angle, 2θ with Cu-K$_\alpha$ radiation of wavelength $\lambda = 1.54178$ Å using a Philips X'pert PRO X-ray diffractometer as described in the Section 3.1. Fig.5.1 (a) shows the XRD patterns of as prepared Mn_3O_4 nanoparticles. The diffraction peaks correspond to the tetragonal (space group 141/amd) Mn_3O_4 single phase (JCPDS Card No.00-001-1127)
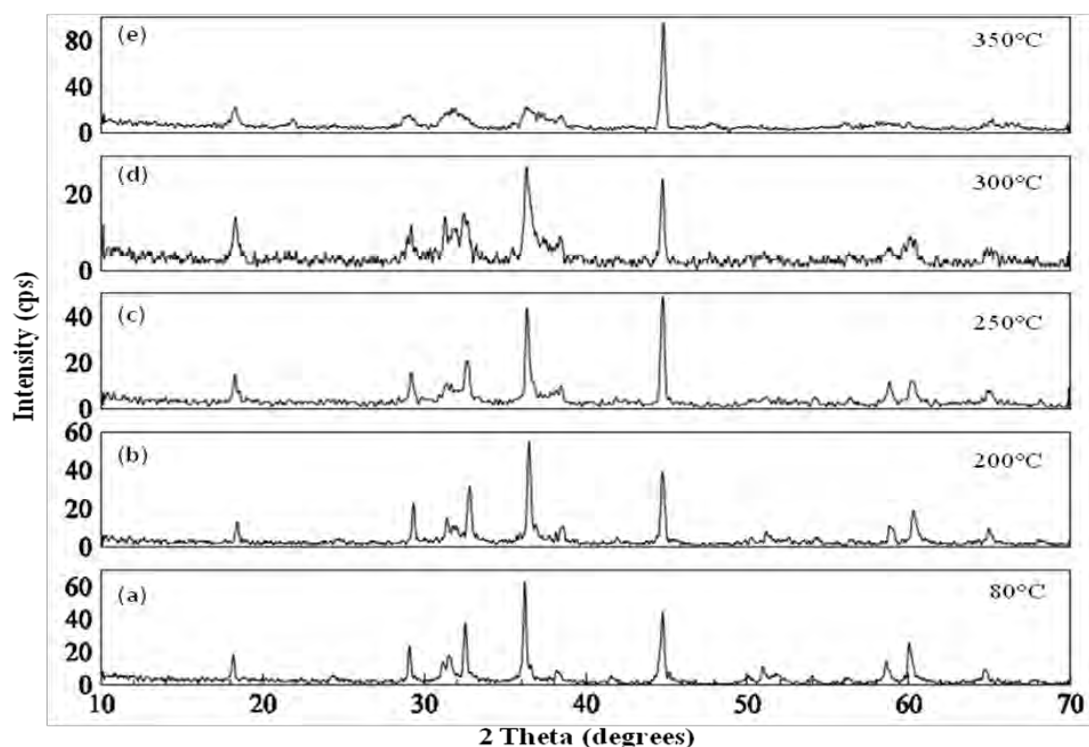

Fig. 5.1: XRD patterns of Mn-oxides nanoparticles heat treated at temperatures from 80 - 350°C

The as prepared Mn_3O_4 nanoparticles were heat treated in a muffle furnace at temperatures from 200 - 700 °C for three hours with 50 °C intervals and they were

immediately submitted for XRD measurement in order to investigate the phase stability as well as phase transformation of the samples. The XRD of the products treated up to 300 °C is similar to the base sample (Fig. 5.1 a – d). This means that Mn_3O_4 nanoparticles are stable up to 300 °C. In the temperature range of 80 - 300 °C, XRD peaks gradually became broader probably indicating phase transformation. The XRD spectra at 350 °C show peaks other than the base peaks as shown in Fig. 5.1 (e). The corresponding phase is identified as Mn_5O_8 (JCPDS Card No.01-072-1427) with monoclinic crystal structure (space group C2/m)

The XRD spectra at 550 °C show some new peaks as shown in Fig.5.2 (e) indicating that a new phase Mn_2O_3 is going to start to form with Mn_5O_8 (JCPDS Card No. 00-010-0069 & 00-020-0718). However, at 700 °C a complete transformation from Mn_5O_8 to Mn_2O_3 (JCPDS Card No. 00-071-0635) was found with cubic crystal structure (space group Ia3) and is shown in Fig. 5.2 (h).
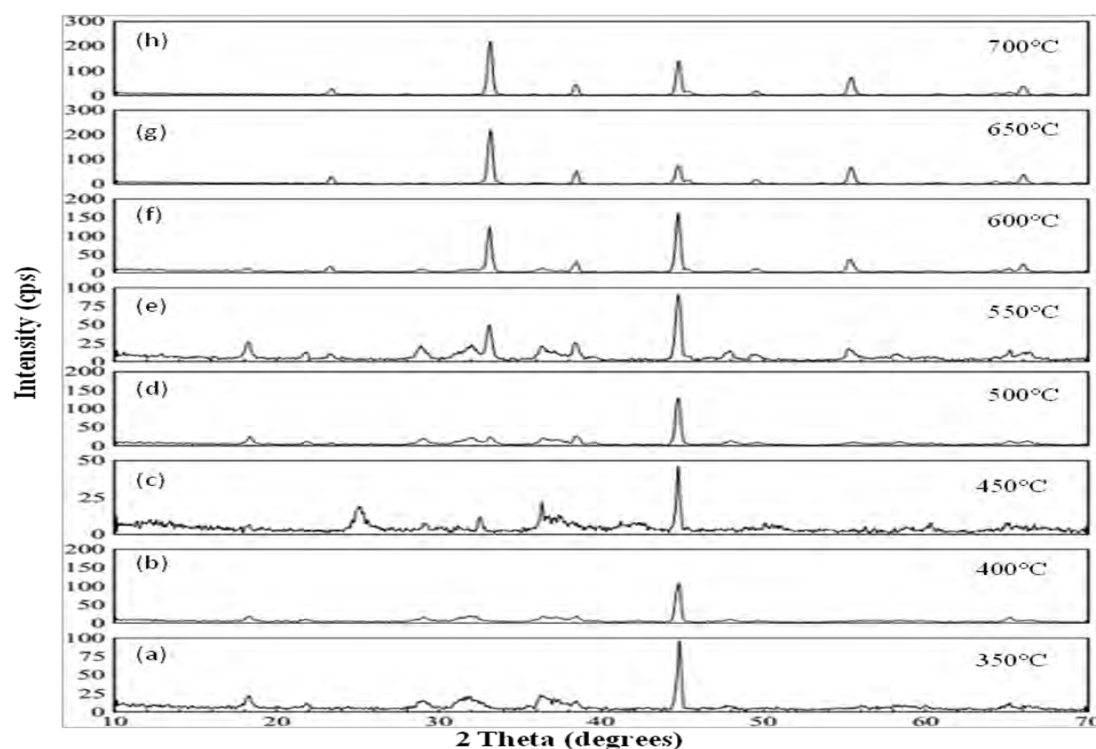

Fig. 5.2: XRD patterns of Mn-oxides nanoparticles heat treated at temperatures from 350 - 700 °C

Now in order to optimize the heating time for phase transformation, the samples were heat treated for different times with thirty minutes interval at the temperature at which the phase transformation occurred and the XRD patterns were investigated. The corresponding XRD patterns for Mn_5O_8 formation are shown in Fig. 5.3. It was observed that the heat treatment of the as prepared Mn_3O_4 nanoparticles at 350 °C, it requires three hours of heating for a complete transformation from Mn_3O_4 to Mn_5O_8 with single phase. However, a new phase Mn_2O_3 was formed after heating the as prepared Mn_3O_4 at 700 °C for one hour only. The corresponding XRD patterns are shown in Fig. 5.3 and 5.4 respectively.
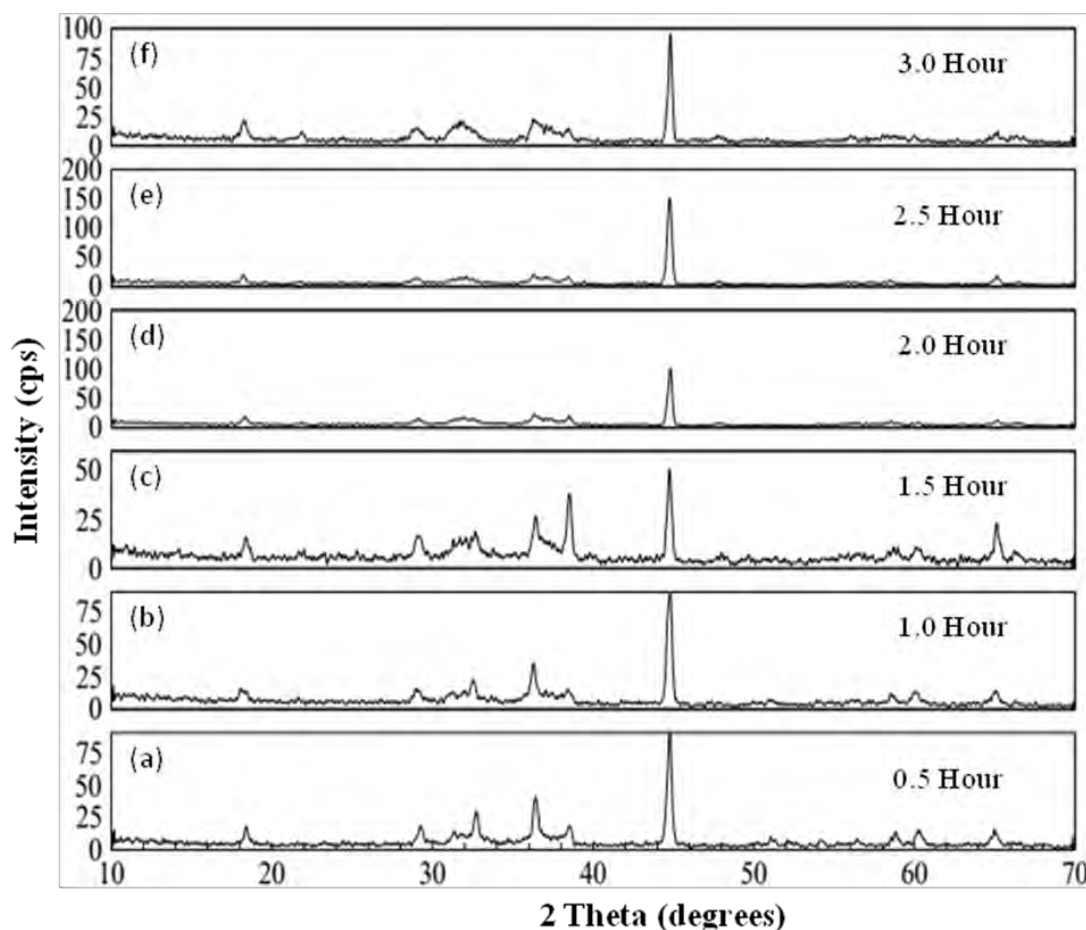

Fig. 5.3: XRD patterns of Mn-oxides nanoparticles heat treated at 350 °C for different time
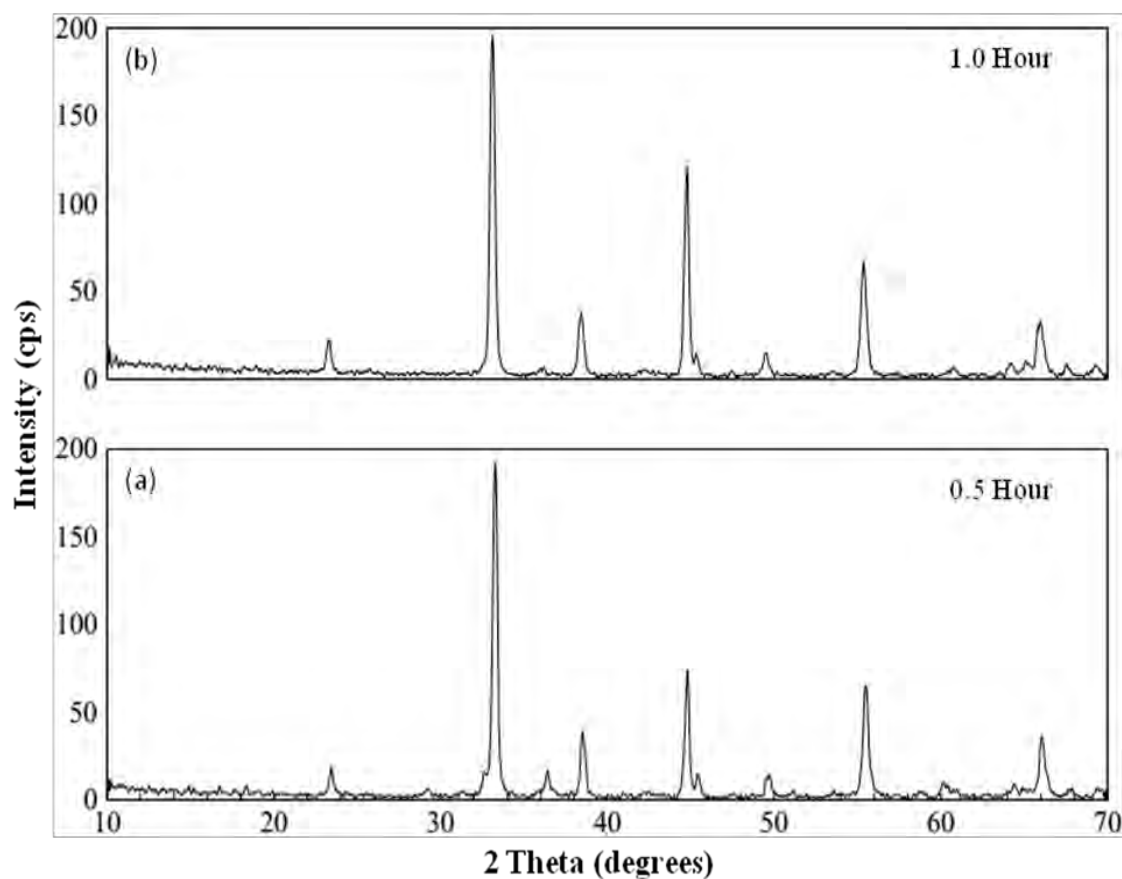
Fig. 5.4: XRD patterns of Mn-oxide nanoparticles heat treated at 700°C for different time

Therefore, from the XRD patterns it can be concluded that Mn_3O_4 nanoparticles with tetragonal crystal geometry have been synthesized via a gel formation route by the reduction of $KMnO_4$ with glycerol at 80 °C. After heating the as prepared Mn_3O_4 nanoparticles at 350°C for three hours a new single phase of Mn_5O_8 with monoclinic crystal geometry was formed and thereafter at 700 °C heat treatment for one hour another new single phase termed as Mn_2O_3 was formed with cubic crystal structure.

5.1.1.2 Crystallite size and lattice parameters

The crystallite size of the Mn_3O_4, Mn_5O_8 and Mn_2O_3 nanomaterials were calculated using the procedure mentioned in Section 3.1.4. The crystallite sizes were measured from the base peaks of (211), (112) and (222) for Mn_3O_4, Mn_5O_8 and Mn_2O_3 respectively and are summarized in Table 5.1. The lattice parameters of Mn_3O_4, Mn_5O_8 and Mn_2O_3 nanomaterials were calculated following the procedure mentioned in Section 3.1.5 and are also summarized in Table 5.1

Table 5.1: Crystallite size and lattice parameters of Mn_3O_4, Mn_5O_8 and Mn_2O_3 nanoparticles

Oxides of Mn	Crystallite size (nm)	Crystal system	Lattice parameters		
			a (Å)	b (Å)	c (Å)
Mn_3O_4	42	Tetragonal	5.75	5.75	9.42
Mn_5O_8	35	Monoclinic	10.347	5.724	4.852
Mn_2O_3	28	Cubic	9.411	9.411	9.411

5.1.2 Energy Dispersive X-ray spectral analysis

Elemental analyses of the Mn_3O_4, Mn_5O_8 and Mn_2O_3 have been performed by Energy Dispersive X-ray (EDX) method. The principle of EDX is described in Section 3.3. The EDX patterns are presented in Fig. 5.5 - 5.7. The peaks observed at 0.525 keV for K lines of O and at 5.894 keV for K lines of Mn elements. The percentages of Mn and O were determined from the intensity of the lines and are summarized in Table 5.2.

Table 5.2: Elemental composition of Mn-oxides nanoparticles

Sample location	Manganese (%)	Oxygen (%)	Tentative formula	Chemical formula
Location - 1	72.13	27.87	Mn_3O_4	
Location - 2	71.95	28.05	Mn_3O_4	
Location - 3	71.84	28.16	Mn_3O_4	Mn_3O_4
Location - 4	72.03	27.97	Mn_3O_4	
Location - 1	68.21	31.79	Mn_5O_8	
Location - 2	68.13	31.87	Mn_5O_8	
Location - 3	67.96	32.04	Mn_5O_8	Mn_5O_8
Location - 4	68.03	31.97	Mn_5O_8	
Location - 1	70.05	29.95	Mn_2O_3	
Location - 2	69.53	30.47	Mn_2O_3	
Location - 3	69.85	30.15	Mn_2O_3	Mn_2O_3
Location - 4	69.73	30.27	Mn_2O_3	

From the chemical compositions obtained from the EDX spectra, it can be concluded that the prepared Mn-oxides are of Mn_3O_4, Mn_5O_8 and Mn_2O_3 with single phase.
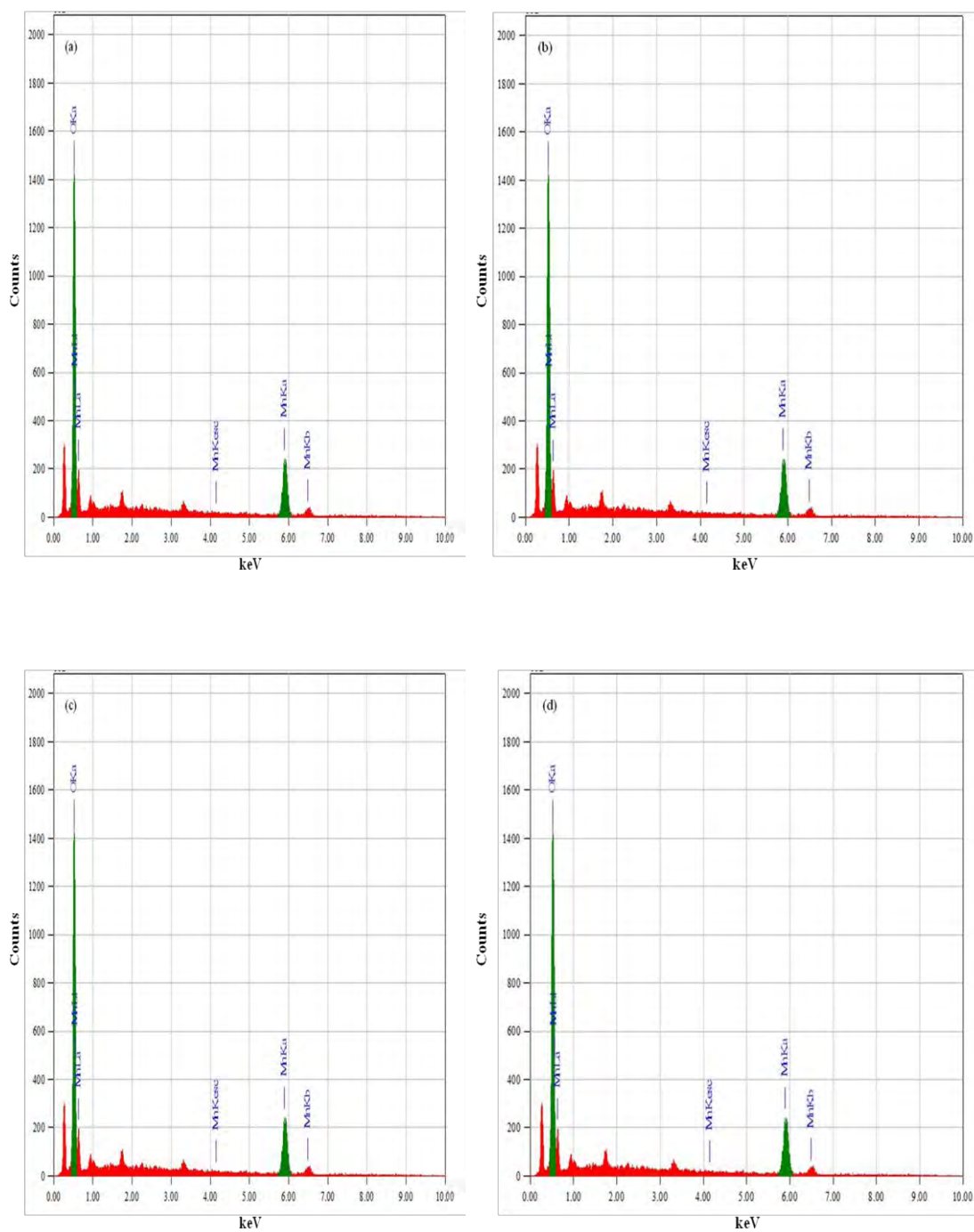
Fig.5.5: EDX analysis of Mn_3O_4 nanoparticles at (a) location 1, (b) location 2, (c) location 3 and (d) location 4.
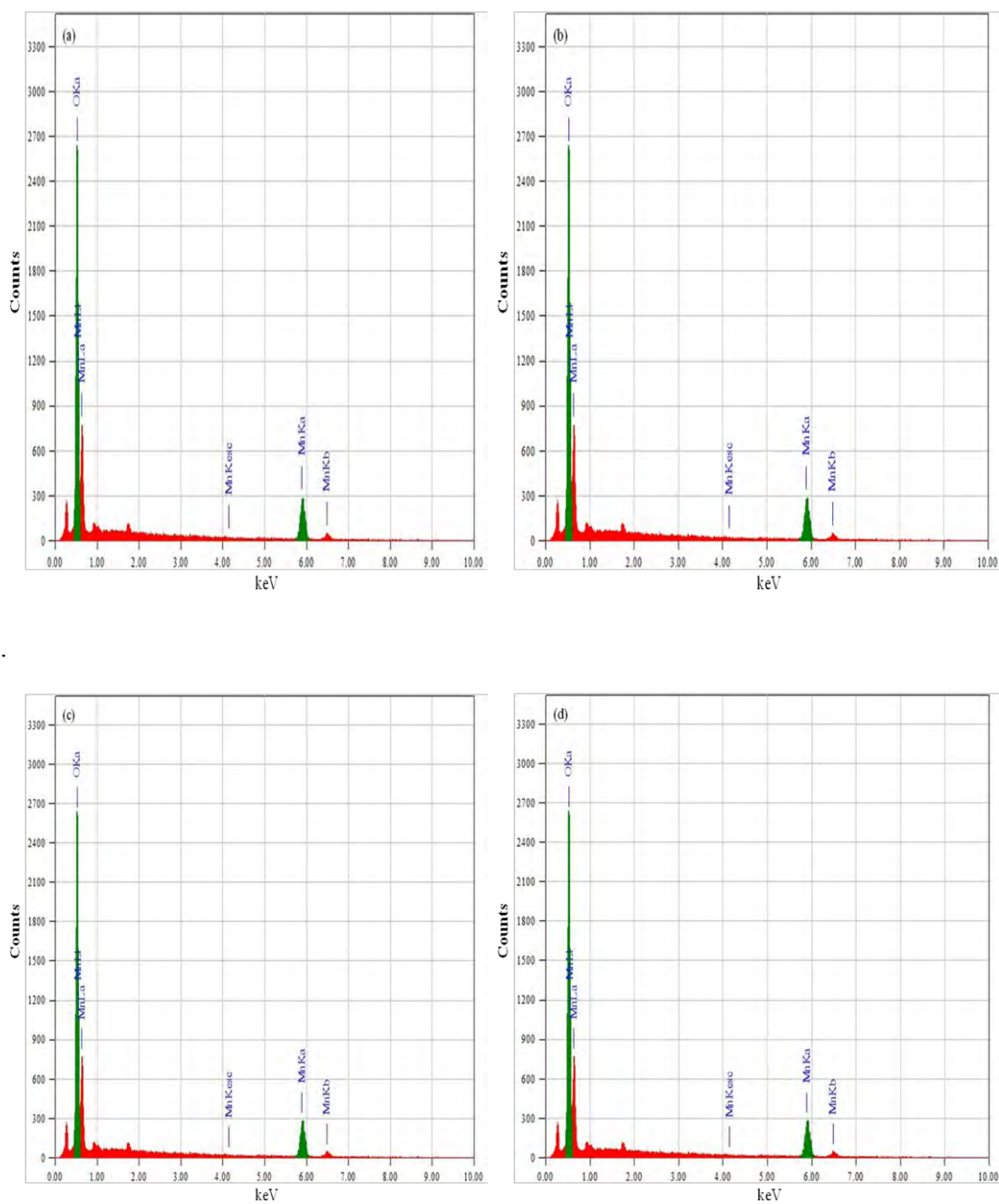
Fig. 5.6: EDX analysis of Mn_5O_8 nanoparticles at (a) location 1, (b) location 2, (c) location 3 and (d) location 4.
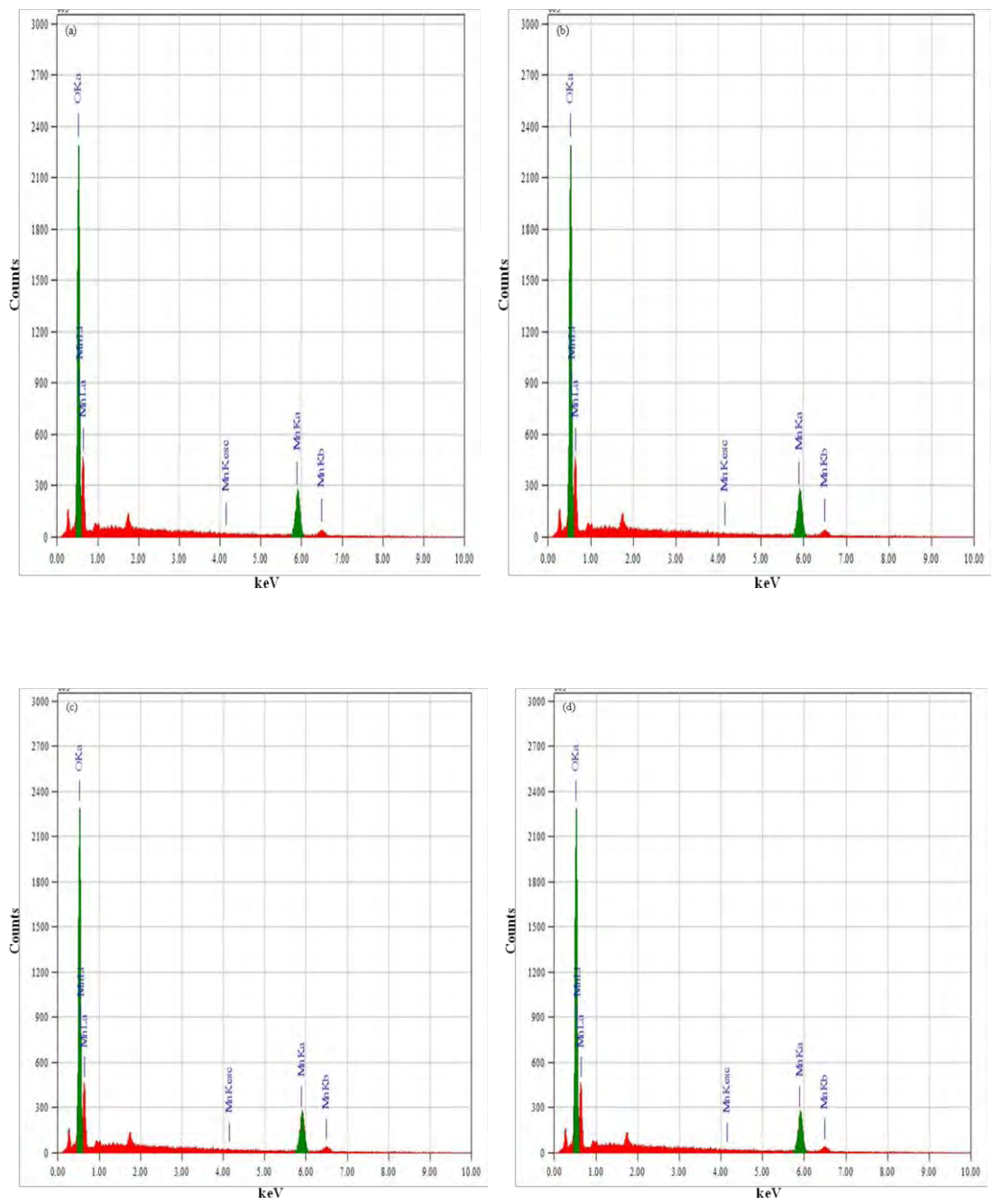
Fig.5.7: EDX analysis of Mn$_2$O$_3$ nanoparticles at (a) location 1, (b) location 2, (c) location 3 and (d) location 4

5.1.3 Fourier Transform Infrared (FTIR) analysis

The Infrared spectra of Mn_3O_4, Mn_5O_8 and Mn_2O_3 nanoparticles are shown in Fig. 5.8. The IR spectrum of the as prepared Mn_3O_4 nanoparticles display three significance peaks in the range of 400 - 650 cm^{-1}. The vibration frequency located at 624.8 cm^{-1} is characteristic of Mn-O stretching modes in tetrahedral sites, whereas the vibration frequency located at 526.5 cm^{-1} corresponds to the distortion vibration of Mn-O in an octahedral environment. The third vibration band, located at 415.6 cm^{-1} is attributed to the vibration of Mn species (Mn^{3+}) in the octahedral site of Mn_3O_4 [1]. Moreover, the narrow band at 1546.6 cm^{-1} and the broad band at 3662.2 cm^{-1} correspond to the O-H vibrating mode of the adsorbed water [2] or may from the OH group of glycerol.

During the heat treatment of Mn_3O_4, removal of water molecules is well demonstrated by the IR spectra. During the heating process, a clear difference is observed in the IR spectra, in the range 400 - 700 cm^{-1}, corresponding of the stretching bands of Mn-O. This change in the position bands at 350 °C and 700 °C can be related to the phase transformation of Mn_3O_4. This result is in a good agreement with X-ray diffraction data.
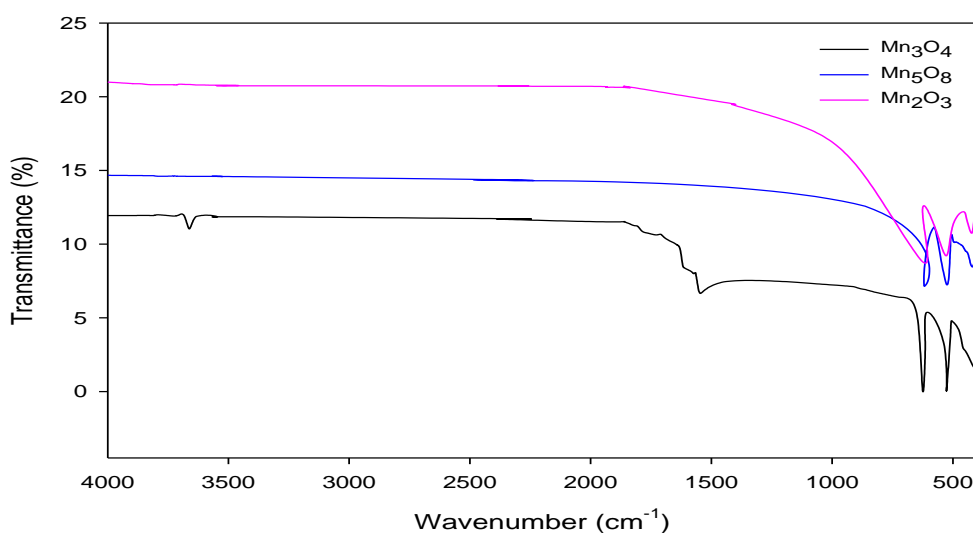

Fig.5.8: FTIR spectra of Mn_3O_4, Mn_5O_8 and Mn_2O_3 nanoparticles

5.1.4 Thermal analysis

In order to examine the thermal stability and phase transformation of Mn-Oxides nanoparticles, Thermo Gravimetric Analysis (TGA) and Differential Scanning Calorimetry (DSC) were carried out between 25 and 700 °C, following the procedure mentioned in Section 3.5 and 3.6. The corresponding figures are shown in Fig. 5.9 - Fig. 5.10. As shown in Fig. 5.9, the first weight loss was observed up to 250 °C and may be attributed to the release of water molecules weakly adsorbed on the particles surface. A broad exothermic peak was obtained at about 404.1 °C. As confirmed by earlier studies [3-5], this thermal event can be corroborated by the fact that Mn_3O_4 can be transformed into Mn_5O_8 in the temperature range of 300 - 450 °C. The new (Mn_5O_8) phase is formed according to the following reaction scheme:

$$Mn_3O_4 + {}^2\!/_5\, O_2 \rightarrow {}^3\!/_5\, Mn_5O_8 \ldots \ldots \ldots (5.1)$$
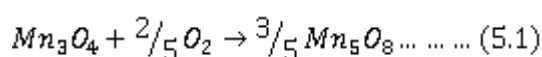
Mn_5O_8 is isostructural with $Cd_2Mn_3O_8$ and crystallizes in the monoclinic system (C2/m) [6]. Mn_5O_8 was observed during the decomposition of manganese oxalate [7] as well as in the transformation hydrohausmannite into anhydrous hausmannite [6, 8]. The oxidation of Mn^{3+} to Mn^{4+} in the temperature range of 300 - 450 °C leads to the crystallization of the Mn_5O_8 phase.

The broad peak observed in the DSC curve and the endothermic event at 636.5 °C, associated to the consequent release of oxygen due to the reduction of Mn_5O_8 to Mn_2O_3. The reaction scheme can be written as follows:

$$^3\!/_5\, Mn_5O_8 \rightarrow {}^3\!/_2\, Mn_2O_3 + {}^3\!/_{20}\, O_2 \ldots \ \ldots \ \ldots \ \ldots \ \ldots (5.2)$$
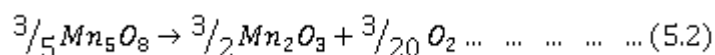
The weight loss still constant at temperature higher than 700 °C, indicating the completion of the thermal decomposition of the intermediate phase Mn_5O_8 and the beginning of the crystallization of Mn_2O_3 as new phase.
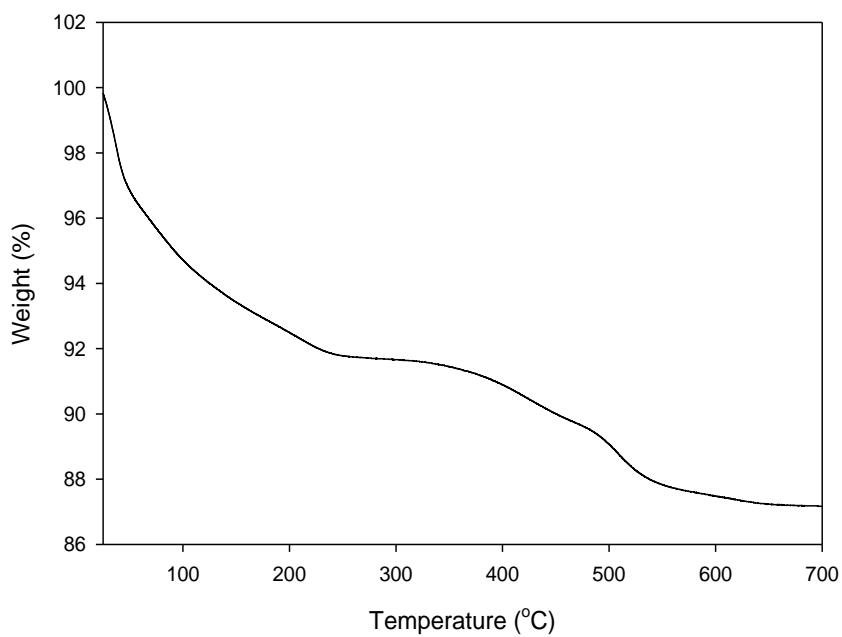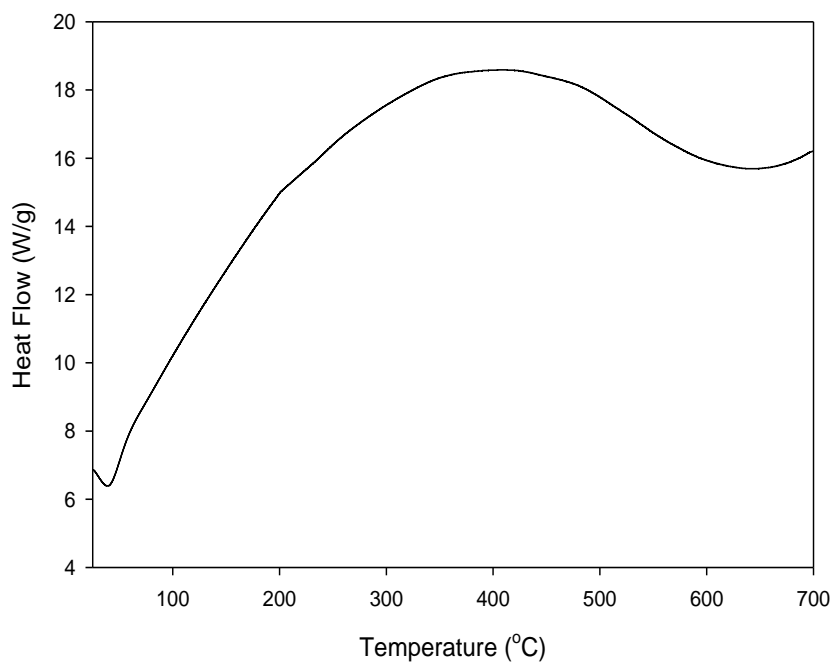
Fig. 5.9: TGA plot of Mn-oxides nanoparticles

Fig. 5.10: DSC plot of Mn-oxides nanoparticles

5.1.5 Surface morphologies of Mn-oxides nanoparticles

Surface morphologies of Mn_3O_4, Mn_5O_8 and Mn_2O_3 nanoparticles obtained at different temperatures were investigated by virtue of Field Emission Scanning Electron Microscopy (FESEM) as shown in Fig. 5.11 - Fig. 5.13. Mn_3O_4 nanoparticles were obtained by reacting $KMnO_4$ and glycerol at 80 °C. As shown in Fig. 5. 11, shows the morphology of the as prepared Mn_3O_4 nanoparticles with the size of about 50 - 100 nm.
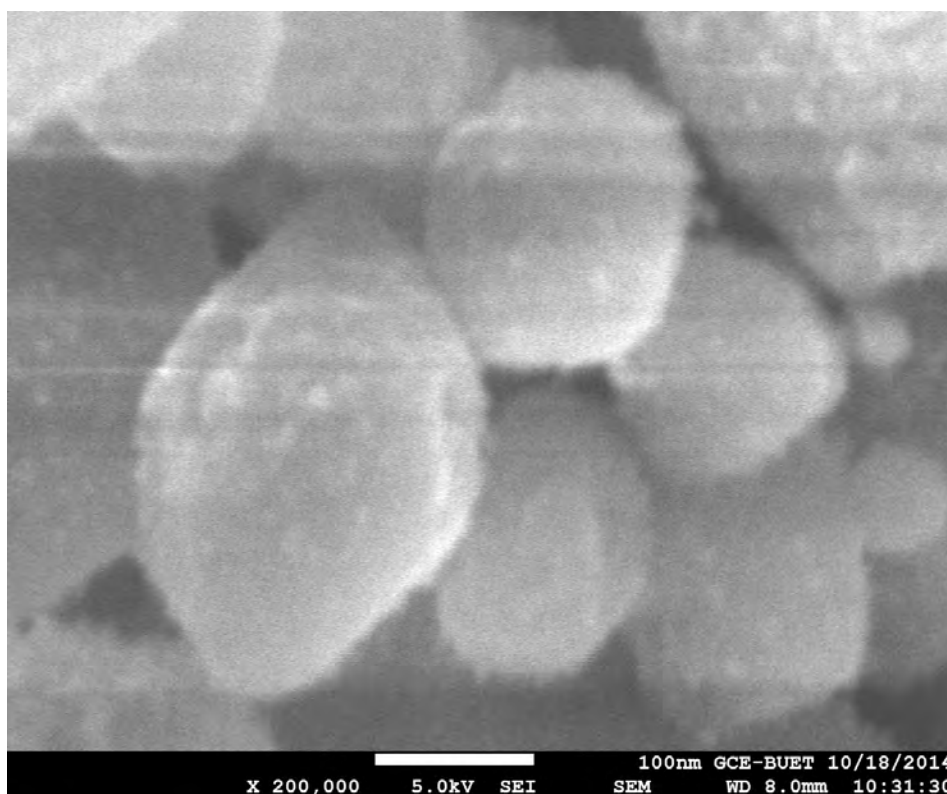

Fig. 5.11: SEM image of as prepared Mn_3O_4 nanoparticles.

From the SEM image of Mn_3O_4 nanoparticles, it can be seen that the nanoparticles are of nanoporous materials which may enhance the functionality of the materials. It seems from the image that the material is in the form of nanoporous or in the form of nanoflower.

Fig. 5.12 shows the SEM image of the Mn_5O_8 nanorods, the three hours heat treated products of as prepared Mn_3O_4 nanoparticles at 350 °C. It can be seen that the sample

consisted of a large amount of rod like products, which maintain the morphology of the product. These rods, about 10-20 nm in diameter, have a lengths about 1-2μm. The surfaces of the rods are almost smooth along their entire length. This result indicates that this route might provide a new mild approach for the synthesis of Mn_5O_8 nanorods.
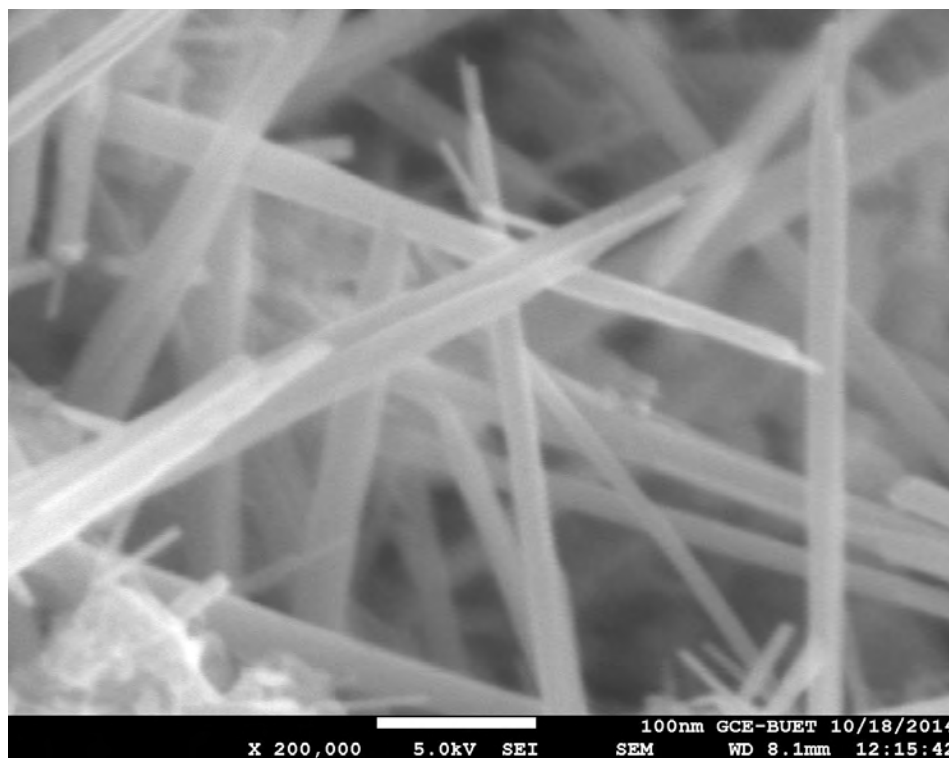

Fig. 5.12: SEM image of Mn_5O_8 nanorods obtained from the three hours heat treated of Mn_3O_4 nanoparticles at 350 °C.

Mn_5O_8 nanorods having mixed valence states may be a metastable oxide of Mn that may show high functionality.

Fig. 5.13 shows the SEM image of Mn_2O_3 nanoparticles obtained from one hour heat treated of as prepared Mn_3O_4 nanoparticles at 700 °C. From the image it reveals that the particles are uniform with cubic structure and the particle size is about 50 – 100 nm.
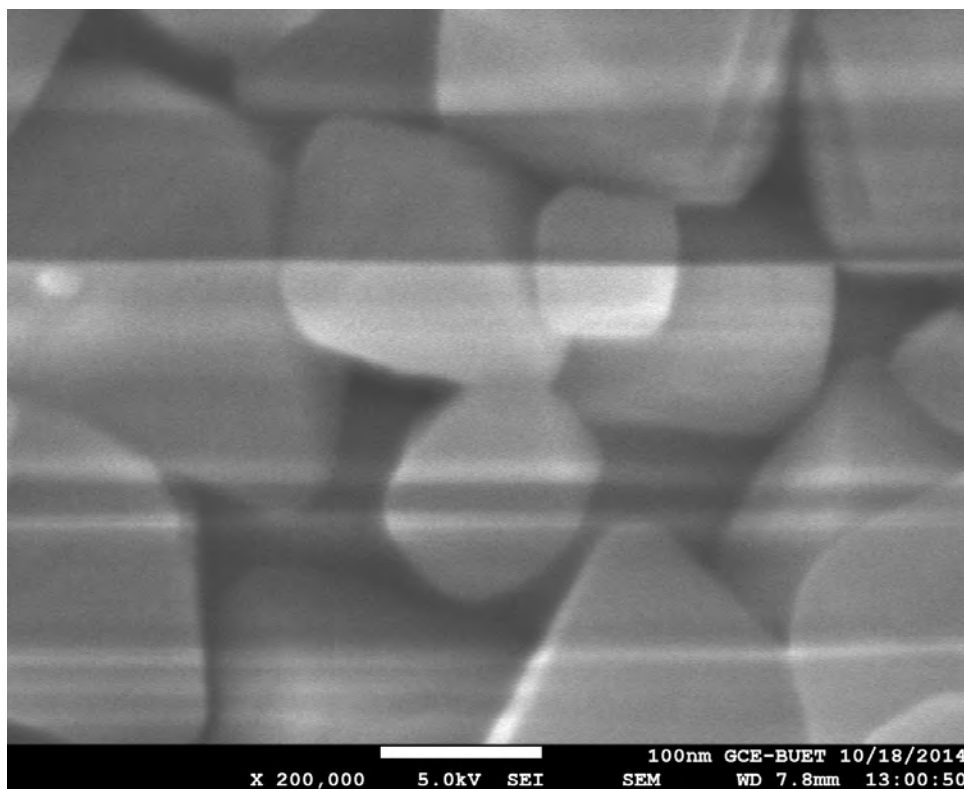
Fig. 5.13: SEM image of Mn_2O_3 nanoparticles obtained from one hour heat treatment of Mn_3O_4 at 700 °C.

Now from the X-ray Diffraction (XRD), Energy Dispersive X-ray spectroscopy (EDX), Fourier Transform Infrared spectra (FTIR), Thermogravimetric analysis (TGA), Differential Scanning Calorimetry (DSC) and Scanning Electron Microscopy (SEM) analyses, it can be concluded that Mn-oxides with variable oxidation states as well as single and mixed valence states can be formed by reacting $KMnO_4$ and glycerol through a single gel formation route after heating at different temperatures. Here, Mn_3O_4 nanoparticles with tetragonal crystal geometry were formed at 80 °C and after the heating of the as prepared Mn_3O_4 nanoparticles at 350 °C for three hours Mn_5O_8 nanorods with monoclinic geometry were formed, and finally after heating the Mn_3O_4 nanoparticles at 700 °C for one hour, Mn_2O_3 nanoparticles with cubic crystal geometry were formed.

5.2 Structural dependence of oxidative property of Mn-oxides nanoparticles

5.2.1 Decolorization of dye using Mn-oxides nanoparticles

The structural dependence of oxidative property of synthesized Mn-oxides nanoparticles such as Mn_3O_4, Mn_5O_8 and Mn_2O_3 nanoparticles are demonstrated by their comparative oxidative capacity in the decolorization of dye solution. Methylene Blue (MB) was taken as a model of an organic dye. The performance of Mn-oxides nanoparticles in the decolorization of MB dye was investigated spectroscopically. Fig.5.14 shows the UV-vis. spectra of the 1×10^{-5} M MB solution before (a) and after (b-d) charging Mn_3O_4, Mn_5O_8 and Mn_2O_3 nanoparticles suspensions (1.0 g L^{-1}) respectively.
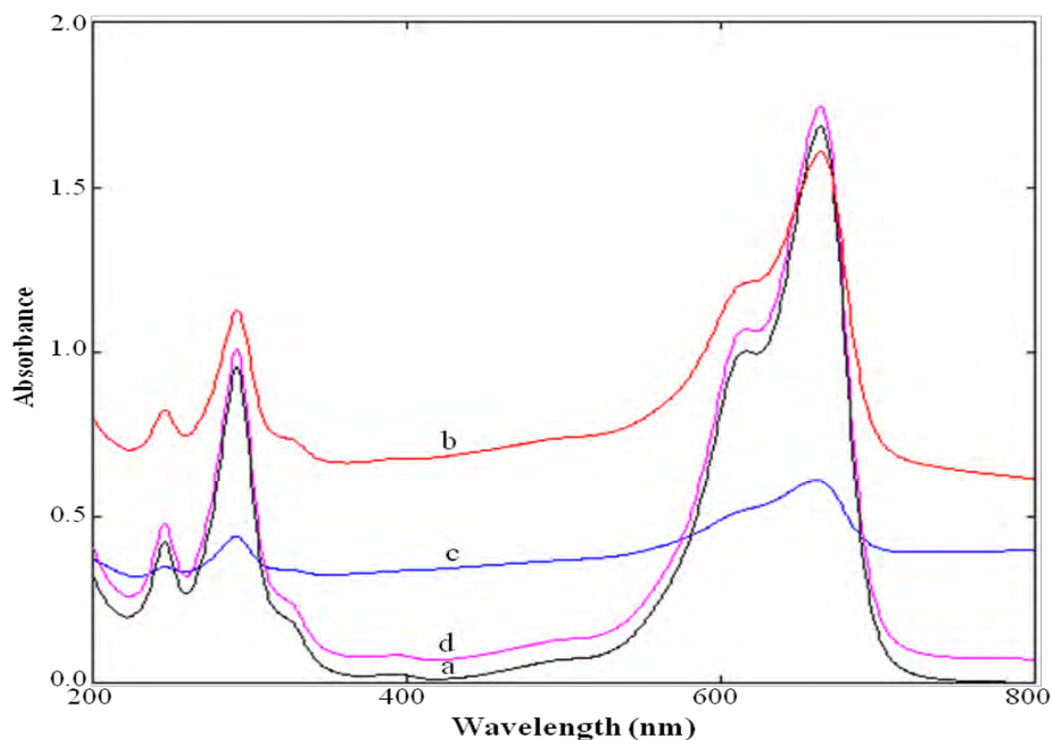

Fig. 5.14: UV-vis spectra of 1×10^{-5} M MB dye solution before (a) and at thirty minutes after (b-d) charging the Mn_3O_4, Mn_5O_8 and Mn_2O_3 nanoparticles respectively

Spectrum (a) clearly exhibits the characteristic peaks of MB in the visible range at *ca.* 614 and 664 nm which are in good agreement to that reported previously [9]. As soon

as the Mn_3O_4, Mn_5O_8 and Mn_2O_3 nanoparticles were added in the dye solution, no remarkable change occurred for Mn_3O_4 (spectrum-b) and Mn_2O_3 (spectrum-d), but for Mn_5O_8 the blue color of the reaction mixture turned to initially light violet and within thirty minutes the characteristic MB peaks plummeted sharply (spectrum-c) showing ca. 63 % decolorization of the dye. It can be seen from the results (Fig. 5.14) that, only Mn_5O_8 nanoparticles with monoclinic crystal structure shows decolorization properties. After the decolorization experiments no color was observed at the time of washing *i.e.* no desorption of dye was observed. The result suggests that the decolorizatrion activity Mn_5O_8 is due to the oxidative property of the oxide and Mn_5O_8 is the only oxide which shows oxidative decolorization at neutral pH.

5.2.1.1 Optimization of MB decolourization with Mn_5O_8 nanorods

The performance of Mn_5O_8 nanoparticles on the decolorization MB dye has been studied in the presence of sulfuric acid. Effect of MB concentration, amount of nanoparticles, influence of pH and function of time on MB degradation were also investigated to suggest an optimum condition. UV-vis absorption spectra of MB solution were measured in all cases.

i. Various concentrations of MB studied for decolourization

1×10^{-5} M, 2×10^{-5} M and 3×10^{-5} M MB solutions were prepared and used to observe the effect of MB concentration on its removal by Mn_5O_8 nanoparticles at low pH. 5 ml of each concentration MB, 5 mL of nano Mn_5O_8 suspensions (0.25 g L^{-1}) and 1 mL H_2SO_4 were mixed together and after 1 min, absorbance of each of the reaction mixture was taken. Fig. 5.15 shows the UV-vis. absorption spectra of untreated 3×10^{-5} M MB solution and spectra of every concentration after 1 min of the reaction.
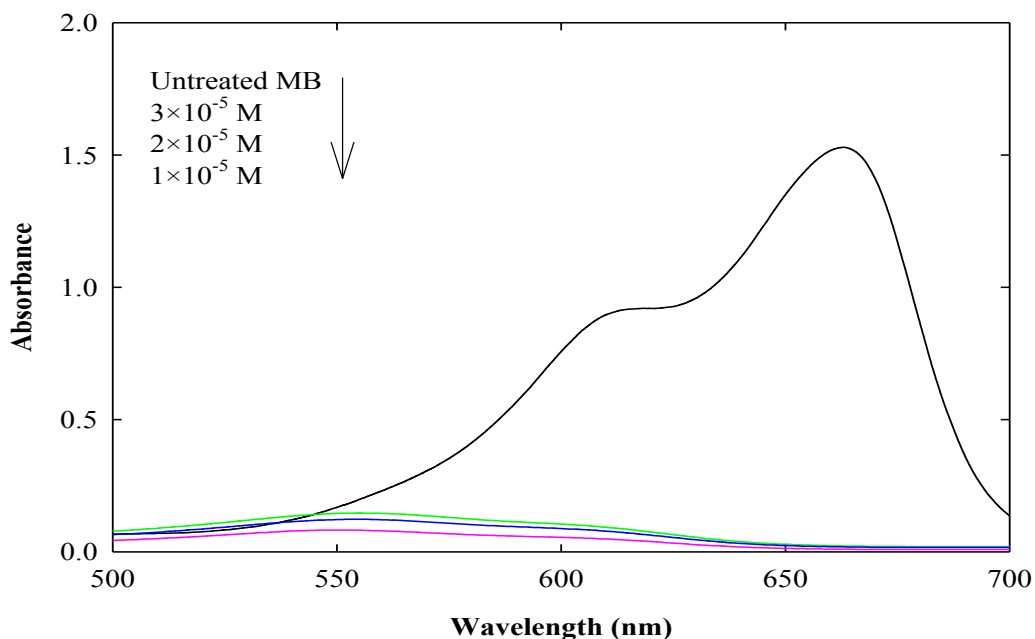
Fig. 5.15: UV-vis. spectrum of untreated 3×10^{-5} M MB and various concentration of MB after treatment with Mn_5O_8 nanoparticles

ii. Influence of amounts of Mn_5O_8 nanoparticles on MB decolorization

To investigate the effect of amount of Mn_5O_8 nanoparticles on MB decolorization, different amount of Mn_5O_8 nanoparticles suspensions (0.25 g L^{-1}), viz., 1.0 mL, 3.0 mL, 5.0 mL and 7.0 mL were added to a fixed amount (5.0 mL of 3×10^{-5} M) of MB solution and allowed to react for 1 min. It was found that 3.0 mL nanoparticles suspension was enough for complete decolorization of that amount of MB. UV-vis. absorption spectra of MB solutions were measured in every case and are shown in Fig. 5.16

F   ount of
Mn$_5$O$_8$ nanoparticles
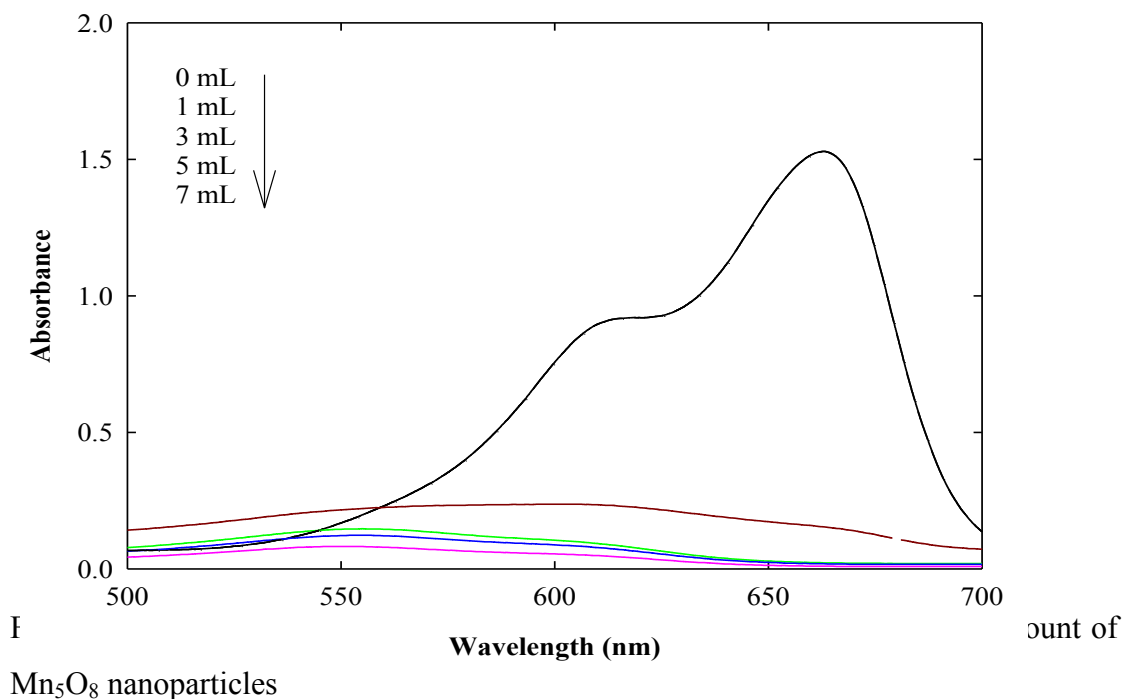
iii. Effect of pH on MB decolorization

Effect of pH of the medium on the decolorization of MB dye was investigated spectroscopically. Fig. 5.17 shows the decolorization of 3×10^{-5} M MB at (a) pH 3 and (b) pH 5 respectively using the Mn$_5$O$_8$ nanoparticles suspension. It can be seen from the results that both the degree and rate of MB decolorization are enhanced at lower pH medium. Thus it appears that the role of acid in the present decolorization process is indeed indispensable.
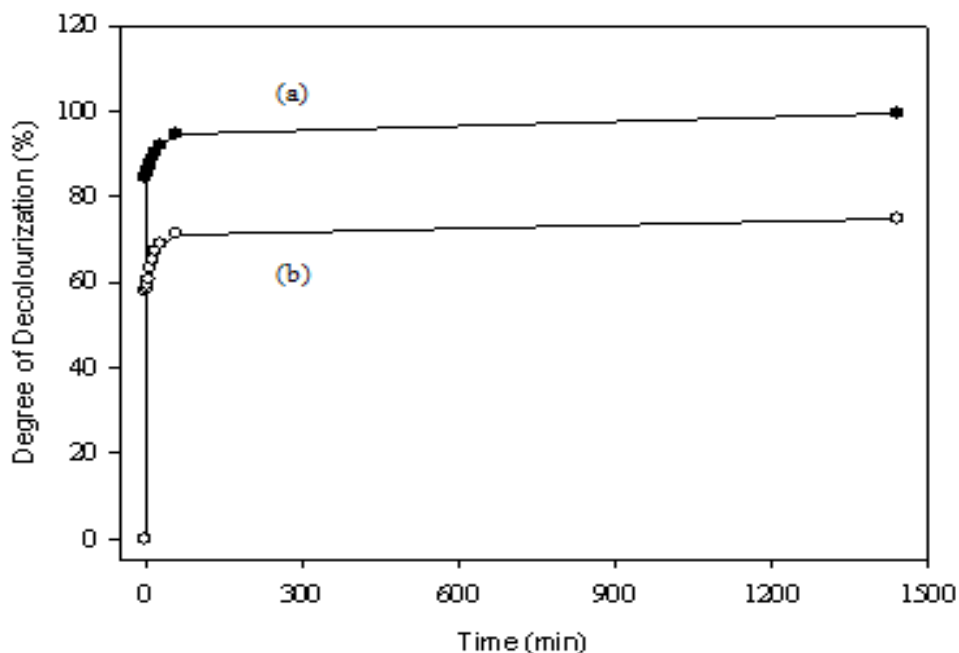
Fig. 5.17: Decolorization of 3×10^{-5} M MB at (a) pH 3 and (b) pH 5 using the Mn_5O_8 nanoparticles suspension

iv. MB decolorization as a function of time

The efficiency of Mn_5O_8 nanoparticles on the decolorization of MB was monitored as a function of time. Fig. 5.18 shows the UV-vis. spectra of the 3×10^{-5} M MB dye solution before (a) and after (b-k) charging the Mn_5O_8 nanoparticles at pH 3. The spectra taken at different time intervals, viz., 1, 3, 5, 7, 10, 15, 20, 30, 60 min and 24 h after charging the nanoparticles corresponding the spectra (b-k) respectively. Inset shows the camera pictures of 3×10^{-5} M MB dye solution before (x) and after (y) charging the Mn_5O_8 nanoparticles. As soon as Mn_5O_8 was added in the dye solution at pH 3, the blue color of the reaction mixture turned to initially light violet and finally colorless. Within 1 min after charging the nanoparticles suspension, the characteristic MB peaks plummeted sharply (spectrum b) showing 85% decolorization of the dye. With further elapse of time, the peaks seem to be disappearing gradually (spectra c-k). Within 30 min, the main absorption band became so broad that no obvious band could be traced suggesting nearly complete decolorization of MB.
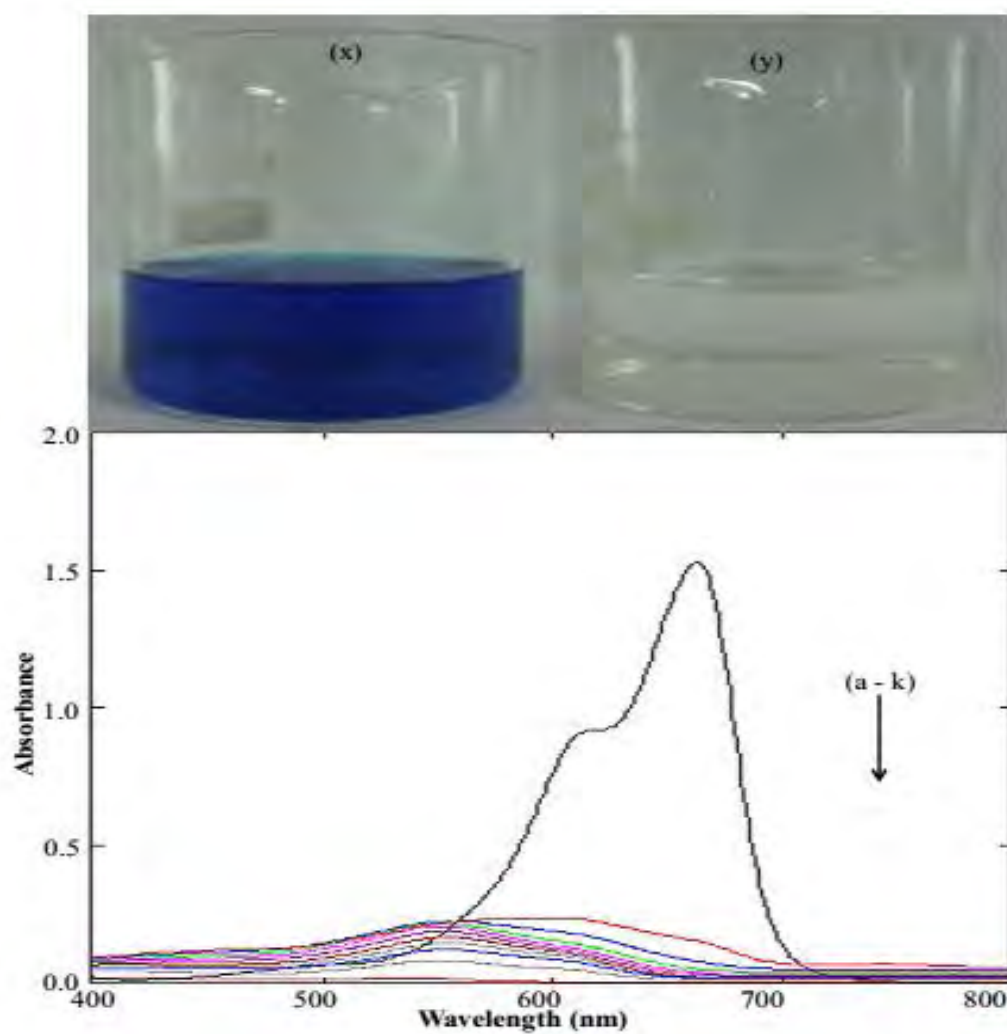
101

Fig. 5.18: UV-vis. spectra of 3×10^{-5} M MB dye solution before (a) and after (b-k) charging the Mn_5O_8 nanoparticles at pH 3. Inset shows the camera pictures of 3×10^{-5} M MB dye solution before (x) and after (y) charging the Mn_5O_8 nanoparticles

5.2.1.2 Structural change of Mn_5O_8 nanorods due to decolorization of MB

The structural change of Mn_5O_8 nanorods for their oxidative property was investigated through the decolorization of MB. 200 mL of 3×10^{-5} M MB solution and Mn_5O_8 nanoparticles suspension (250 mg L^{-1}) at pH 3 was taken for investigation. The reaction mixture was kept undisturbed for 24 hours. Then the Mn_5O_8 nanorods were separated from the mixture and washed repeatedly with deionized water. The washed samples were dried at 80 °C and then XRD analysis was carried out for structural characterization. Fig. 5.19 shows the XRD patterns of Mn_5O_8 (a) before and (b) after decolorization of MB
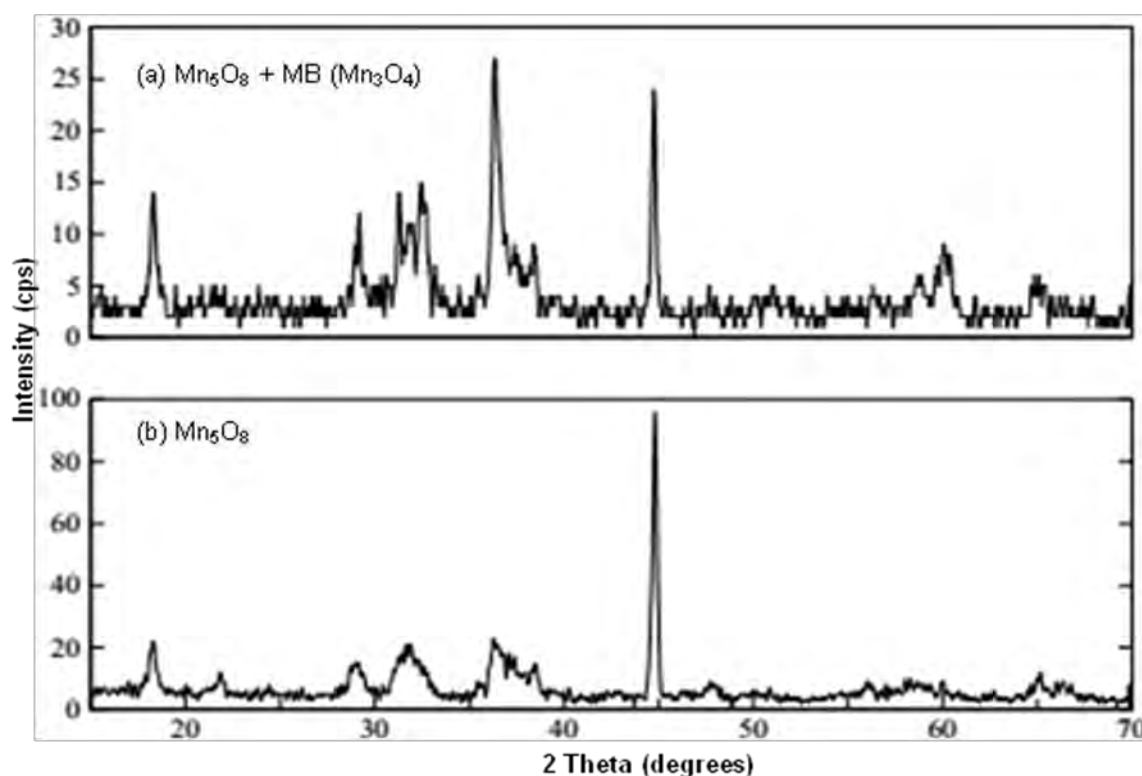

Fig. 5.19: XRD patterns of Mn_5O_8 (a) before and (b) after decolorization of MB

From the XRD patterns it is clear that Mn_5O_8 reduced to Mn_3O_4 during the decolorization process. This may be due to the fact that Mn_5O_8 is a metastable compound which through oxidizing the dye reduced to stable Mn_3O_4.

5.2.2. Oxidative property of Mn₃O₄ and Mn₂O₃ nanoparticles

From the earlier investigations it was observed that Mn_3O_4 and Mn_2O_3 nanoparticles do not show any decolorization property in neutral medium. Then attempt is taken to justify the decolorization property of these two oxides in lower pH. 5 mL Mn_3O_4 and 5 mL of Mn_2O_3 nanoparticles suspension (250 mgL^{-1}) was added to 5 mL of 1×10^{-5} M MB solution separately and after 30 min the decolorization of MB was measured through the UV-visible spectroscopy. The UV-vis spectra of 1×10^{-5}M MB dye solution before and at thirty minutes after charging the Mn_3O_4 and Mn_2O_3 nanoparticles suspensions respectively at pH 3 are shown in Fig. 5.20.
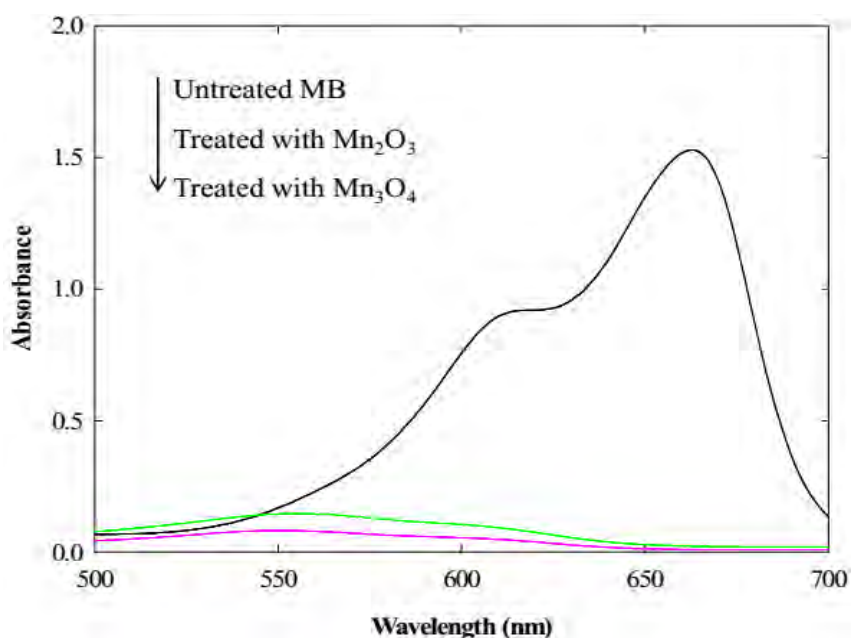

Fig. 5.20: UV-vis spectra of 1×10^{-5} M MB dye solution before and at thirty minutes after charging the Mn_3O_4 and Mn_2O_3 nanoparticles respectively at pH 3

From the UV-visible spectra it is evident that Mn_3O_4 and Mn_2O_3 also exhibit decolorization property at lower pH. In addition it is found that Mn_3O_4 shows greater decolorization activity than Mn_2O_3. To justify whether the decolorization is oxidative or adsorptive for Mn_3O_4 and Mn_2O_3, structural changes of these oxides were investigated after the dye degradation.

104

5.2.3. Structural changes of Mn₃O₄ and Mn₂O₃ due to decolorization of MB

The structural changes of Mn_3O_4 and Mn_2O_3 nanoparticles due to decolorization of MB was investigated following the procedure described in Section 5.2.2. Fig. 5.21 shows the XRD patterns of Mn_3O_4 (a) before and (b) after decolorization of MB and Fig. 5.22 indicates the XRD patterns of Mn_2O_3 (a) before and (b) after decolorization of MB
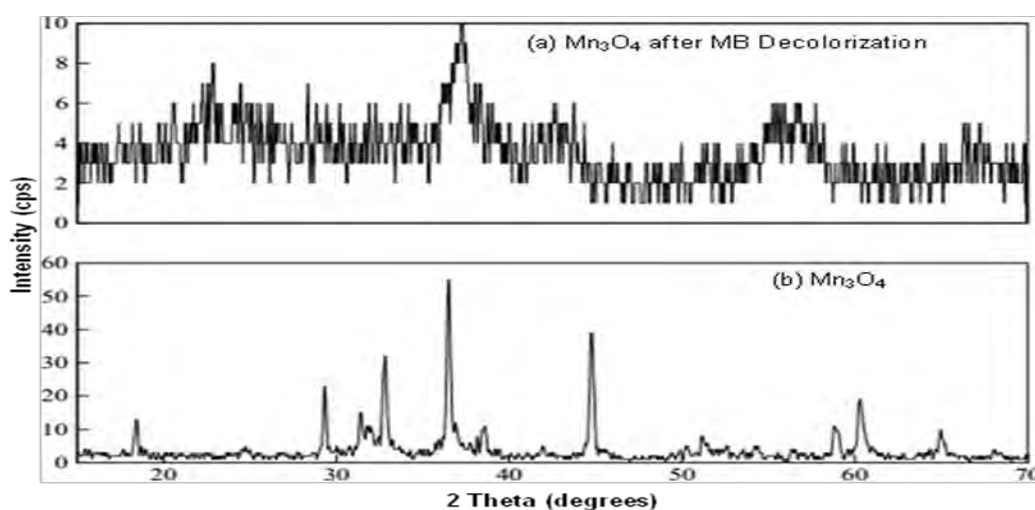

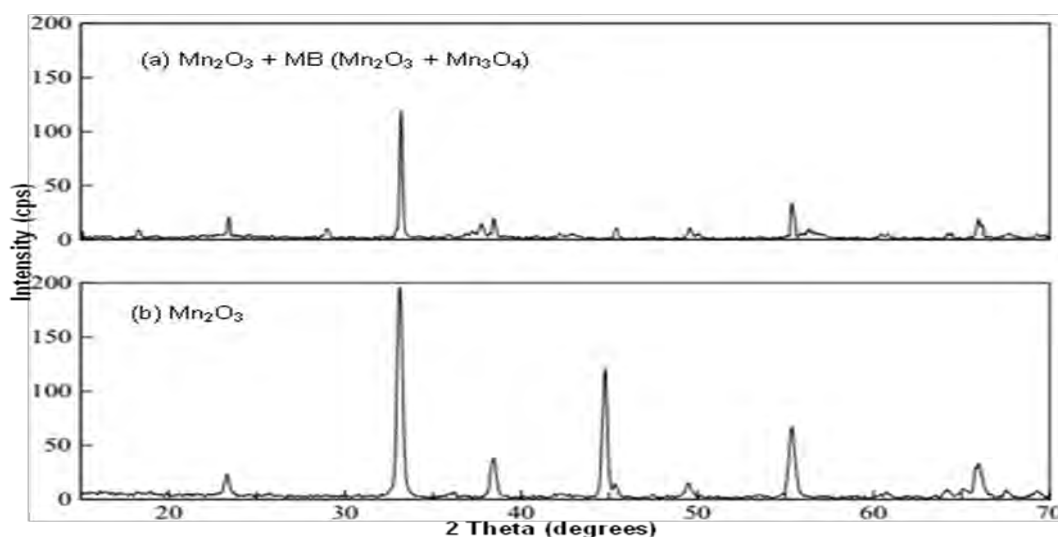Fig. 5.21: XRD patterns of Mn_3O_4 (a) before and (b) after decolorization of MB

Fig. 5.22: XRD patterns of Mn_2O_3 (a) before and (b) after decolorization of MB

From the Fig. 5.21 it is obvious that after decolorizing MB, Mn_3O_4 shifts from their tetragonal crystalline structure to amorphous nature. Furthermore, desorption of dye was observed after the decolorization experiments. From the SEM image of Mn_3O_4 nanoparticles (Fig. 5.11) it can be seen that, the nanoparticles are in nanoporous materials. Therefore, we can predict that the decolorization of MB dye occurs may be due to adsorption as well as oxidation. However, further details investigation is required to find the competitive oxidative and adsorptive properties of Mn_3O_4.

Structural change of Mn_2O_3 nanoparticles due to decolorization of MB dye was further investigated and the XRD patterns are depicted in Fig. 5.22. From the XRD patterns it is found that during the decolorization of MB dye, Mn_2O_3 reduced to Mn_3O_4. This is due to the fact that Mn_3O_4 is one of the most stable oxides of Mn and Mn_2O_3 decolorize MB through oxidative degradation.

Now from the oxidative characterization of Mn_3O_4, Mn_5O_8 and Mn_2O_3 it is evident that, in neutral media only Mn_5O_8 shows oxidative property for decolorization of MB whereas Mn_3O_4 and Mn_2O_3 do not show any oxidative property. The metastable Mn_5O_8 oxide shows a tendency to form a stable oxide of Mn through oxidation or reduction process. But in lower pH Mn_3O_4 and Mn_2O_3 also show decolorization of MB. The decolorization of MB by Mn_3O_4 might be occurred due to the simultaneous adsorption and oxidation of MB, whereas the decolorization of MB by Mn_5O_8 and Mn_2O_3 occurred through oxidative degradation.

Conclusion

Mn-oxides nanoparticles having different crystalline geometry and surface morphology have been successfully synthesized via a gel formation route by the reduction of $KMnO_4$ with glycerol. Mn_3O_4 nanoparticles were immediately formed after heat treatment of the gel at 80 °C. The heat treatment at 350°C and 700 °C results Mn_5O_8 and Mn_2O_3. The crystalline geometry of these oxides is tetragonal, monoclinic and cubic respectively for Mn_3O_4 Mn_5O_8 and Mn_2O_3. Surface morphology of the oxides is also found to be dependent on the heat treatment. Mn_3O_4 particles are flower like porous with a average diameter of 50 nm, Mn_5O_8 particles are rod shaped with a diameter of 10 nm and length of 1-2 μm and Mn_2O_3 particles are cubic in shape.

The oxidative property of the synthesized Mn-oxides nanoparticles, *viz*., Mn_3O_4, Mn_5O_8 and Mn_2O_3 was investigated from the decolorization of Methylene Blue (MB). Among the different oxides, Mn_5O_8 nanorods were found to be a promising material for decolorization of MB from water even in neutral solution. After thirty minutes the degree of decolorization of MB by Mn_5O_8 nanoparticles reached more than 60% whereas Mn_3O_4 nanoparticles and Mn_2O_3 structure do not show any decolorization of MB in absence of acid. pH of the decolorization medium exerts significant effect on the degree of dye decolorization. The degree of decolorization of MB by Mn_5O_8 nanoparticles reached more than 85% within 1 min at the pH as low as 3. At lower pH Mn_3O_4 and Mn_2O_3 also exhibit decolorization of MB.

Structural dependence of oxidative properties of the synthesized Mn-oxide nanoparticle, having different crystal geometry was further investigated from the structural changes during the decolorization of Methylene Blue (MB). It was found that after decolorizing of MB, Mn_3O_4 nanoparticles lost their crystalline nature and converted to amorphous Mn_3O_4. Investigation suggests that the decolorization activity of Mn_3O_4 might results from oxidation as well as adsorption. However, from the structural investigation of Mn_5O_8 and Mn_2O_3 before and after dye degradation

suggests that the decolorization activity of the oxides is due to their oxidative activity. The results further suggest that among the three oxides, the metastable Mn_5O_8 shows superior dye decolorization activity among the oxides under investigation in this study.

The low cost single route for the preparation of different oxides of Mn especially Mn_5O_8 nanorods will open a new window of application of these materials in different fields where oxidative and adsorptive activities are concern. This synthetic route might generate new thoughts in the preparation of Mn-oxide based nano-composites in the field of 'nanomaterials for energy and environment'.

References

[1]. M. Ishii, M. Nakahira, T. Yamanaka, *Solid State Comm.*, 11 (1972) 209

[2]. S. Rui, W. Hong-jun, F. Shou-hua, *Chem. Res. Chinese Universities*, 28 (2012) 577

[3]. P. Tailhades, B. Gillot, A. Rousset, *J. Phys. IV C1*, 2 (1997) 49

[4]. T. Gao, P. Norby, F. Krumeich, H. Okamato, R. Nesper, H. Fjellvag, *J. Phys. Chem. C.*, 114 (2010) 922

[5]. V. Berbenni, A. Marini, *Mat. Res. Bull.*, 38 (2003) 1859

[6]. S. Fritsch, J. Sarrias, A. Rousset, G. U. Kulkarmi, *Mat. Res. Bull.*, 133 (1980) 81

[7]. J. A. Lee, C. E. Newham, F. S. Stone, F. L. Tye, J. Solid State Chem., 131 (1980) 81

[8]. J. H. Rask, P. R. Buseck, Am. Mineral., 71 (1986) 805

[9]. T. Y. Zhang, T. Oyama, A. Aoshima, H. Hadika, J. C. Zhao, N. Serpone, J. Photochem. Photobiol. A, 140 (2001) 163

[10]. A. T. Stone, J. J. Morgan, Environ. Sci. Technol., 18 (1984) 450